Fabrication of Tapered Dual-core As_2Se_3-PMMA Fiber and Its Applications

by

Song Gao

Thesis submitted to the
Faculty of Graduate and Postdoctoral Studies
In partial fulfillment of the requirements for the Degree of
Doctor of Philosophy
in
Physics

Ottawa-Carleton Institute for Physics
University of Ottawa
Ottawa, Ontario, Canada

To my family

Abstract

Fiber optical temperature and strain sensors have been extensively investigated for applications in the civil structures to ensure safety and prevent disasters in advance. Most of the demonstrated fiber sensors are based on the silica fibers to form an interferometer by measuring the spectrum wavelength shift caused by the change of the refractive index and fiber length, and the sensitivities, defined as the rate of wavelength shift with respect to temperature or strain, are limited by the small values of thermal-expansion coefficient and thermo-optic effect of the silica materials. To improve the sensitivity, we designed the dual-core As_2Se_3-PMMA fiber with the PMMA cladding diameter 56.5 times larger than that of the As_2Se_3 cores, which brings out many interesting sensing applications.

Nonlinear devices have a variety of practical applications including parametric amplification, all-optical switching, super-continuum generation, and sensing applications. Tapered chalcogenide-polymer fiber structures composed of an As_2Se_3 core and a polymethyl methacrylate (PMMA) cladding are a promising platform for nonlinear applications because the As_2Se_3 core provides high nonlinearity over the near- and mid-infrared spectral ranges for compact nonlinear devices with low power consumption and the PMMA cladding provides high mechanical strength for easy handling. Advanced As_2Se_3-PMMA fiber structures such as dual-core fibers that support guided propagation of an even mode and an odd mode will open the way for a variety of novel devices in the near- and mid-IR wavelength range.

In my work I utilized two As_2Se_3 fibers and a polymethyl methacrylate (PMMA) tube for the fabrication of dual-core As_2Se_3-PMMA tapers and demonstration of the sensing applications and nonlinear optical effects.

The thesis mainly consists of three parts: the fabrication process, the sensing applications, and the nonlinear applications in the tapered dual-core As_2Se_3-PMMA fiber.

In the first part, the fabrication process of the tapered dual-core As_2Se_3-PMMA fiber is introduced. The dual-core As_2Se_3-PMMA fibers are fabricated using a rod-in-tube method. The images of the setups and fibers in process are listed.

In the second part, a theoretical model for temperature and strain measurement and four sensing applications are introduced. Firstly, we demonstrate an approach for high-sensitivity simultaneous temperature and strain measurement in a dual-core As_2Se_3-PMMA taper with As_2Se_3 core diameter of 0.55 μm. High measurement sensitivities are observed for both principal polarization axes of the tapered dual-core As_2Se_3-PMMA fiber with temperature sensitivities of -115 pm/ºC for axis-1, -35.5 pm/ºC for axis-2, and strain sensitivities of -4.21 pm/με for axis-1 and -3.16 pm/με for axis-2. Secondly, the thermal forces in a dual-core As_2Se_3-PMMA taper are investigated. A temperature-insensitive strain sensor is proposed and demonstrated based on the thermal forces. Finally, two approaches for temperature and strain sensitivity enhancement are investigated. The first approach is by reducing the value of the variation of the difference between phases of the even and odd modes with respect to wavelength ($\partial\phi_d(\lambda)/\partial\lambda$) and increasing thermal-forces in a dual-core As_2Se_3-PMMA taper with As_2Se_3 core diameter of 2.5 μm. The value of $\partial\phi_d(\lambda)/\partial\lambda$ decreases with the As_2Se_3 core diameter and thermal-forces on the As_2Se_3 cores are enhanced in the fibers with large PMMA cladding, which work together to enhance the measurement sensitivity. The second approach is based on effective group-velocity matching between the even and odd modes of a dual-core As_2Se_3-PMMA taper on which an antisymmetric long-period grating is inscribed. The variation of the difference between phases of the even and odd modes with respect to wavelength tends to 0 ($\partial\phi_d(\lambda)/\partial\lambda \to 0$) near the resonance wavelength of the grating due to the effective group-velocity matching between the two modes, and consequently, thermally-induced change of the difference between phases of the two modes $\phi_d(\lambda)$ leads to a large wavelength shift indicating enhancement of the temperature measurement sensitivity.

In the third part, I study the nonlinear optical effects in the hybrid fibers. Firstly, I demonstrate modulation instability within the normal-dispersion regime in a dual-core As_2Se_3-PMMA fiber. Then I review the work about the forward stimulated Brillouin scattering and its sensing applications. The radial and torsional-radial guided acoustic modes of silica fibers and tapered dual-core As_2Se_3-PMMA fibers are investigated experimentally and the preliminary results are presented.

Acknowledgments

Being a member of the Fiber Optics Group in the University of Ottawa is a happy and fascinating experience for me. Four years is a long journey even in one’s life but this one seems too short for me. I wish time could go slow to let me enjoy staying here. During this journey pursuing my Ph.D. degree, I grew up to a real researcher. There were moments of frustration and moments of happiness interwoven in this period, but most impressively, moments of self-recognition and enjoying the scientific research. This thesis cannot be finished without the help of many people. It is my great honor to have this opportunity to thank all the people who have helped me during my Ph.D. study. I will cherish this unforgettable experience forever.

First of all, I would like to sincerely thank my supervisor, Professor Xiaoyi Bao, for her careful guidance and support in my Ph.D. study. It is my great honor to work with Prof. Bao. Her critical thinking, strong passion, broad knowledge and thoughtful insight in research, impress me a lot. Her perseverance and dedication towards the real physics is astounding, and will always be regarded as a source of inspiration to me. This thesis would be impossible without her constant support and guidance. Her encouragement and constant support greatly increase my confidence in research and also inspired me to pursue the real physics behind all these complicated phenomena during my Ph.D. studies. I would also express my great gratitude to Professor Liang Chen for his precious advice and instructive discussions. His profound knowledge in physics and mathematics cannot be matched and has always inspired me to challenge all obstacles that come in the way of my research.

I am grateful to Dr. Chams Baker for his novel ideas, instructive suggestions and strict requirements for my research. He always has a strong passion on the research, which deeply impresses me. His profound knowledge and kindness guided me, and I have learned so much from him. He is more than an instructor and Postdoc to me but a big brother and close friend. He was always with me whenever I got confused, lost and disappointed. This thesis would be impossible without his continuous guidance.

Many thanks are given to Dr. Ping Lu for his thoughtful discussions and valuable suggestions on my research. His guidance benefits me a lot in terms of how to analyze and solve the problems when I started my research. We worked together on my first project about nonuniform fiber based random laser and random number generation. I also thank Dr. Liang Zhang and Dr. Lijuan Gu for their helpful discussions and assistance when I'm depressed and confused. Both of them have rigorousness attitude towards science and research, which really impress me.

I would like to express my gratitude to Dr. Yanping Xu and Mr. Bhavaye Saxena. They provided tremendous assistance and guidance with my researches and experiments. It is a great pleasure to collaborate with them to work on several exciting research projects.

I am thankful to all the other colleagues in Fiber Optics group — Prof. Zhengying Li, Prof. Ping Han, Dr. Chen Wang, Prof. Mingjiang Zhang, Prof. Chunhua Wang, Dr. Yang Lu, Dr. Qian He, Dr. Dapeng Zhou, Mr. Dao Xiang and Ms. Meiqi Ren, Mr. Benoit Vanus, Mr. Zhichao Zhou, Mr. Robert Chutu Li, Mr. Tian Wang and Mr. Wei Cai. My life in the laboratory was enriched by their company.

I also express my gratitude to the financial support of China Scholarship Council (CSC).

Finally, I am deeply indebted to my family and my love in China. It is their encouragement, enduring love and understanding that encourage me to pursue my graduate study.

It is impossible to thank all, and I apologize to those I have inadvertently left out.

Thank you all again.

Statement of originality

This work contains no material which has been accepted for the award of any other degree or diploma in any university or other tertiary institution and, to the best of my knowledge and belief, contains no material previously published or written by another person, except where due reference has been made in the text.

I give consent to this copy of my thesis, when deposited in the University Library, being available for loan and photocopying.

SIGNED: ………………………………..

DATE: …………………………………...

Supervisor: Prof. Xiaoyi Bao

Contents

List of Figures

List of Tables

List of Acronyms

AFG	Arbitrary function generator
BPF	Bandpass filter
CW	Continous wave
EAS	Electrical spectrum analyzer
EDFA	Erbium-doped fiber amplifier
EOM	Electro-optic modulator
FBG	Fiber Bragg gratings
FSBS	Forward stimulated Brillouin scattering
FUT	Fiber under test
FWM	Four-wave mixing
GAWBS	Guided acoustic-wave Brillouin scattering
IBBS	Incoherent broad-band source
IR	Infrared
LP	Linear polarizer
LPG	Long-period grating
MI	Modulation instability
Mid-IR	Mid-infrared
MMF	Multi-mode fiber
MZI	Mach-Zehnder interferometer
OSA	Optical spectrum analyzer

PBS	Polarization beam-splitter
PC	Polarization controller
PCF	Photonic-crystal fiber
PD	Photodetector
PMMA	Poly (methyl methacrylate)
RI	Refractive index
SMF	Single mode fiber
SPM	Self-phase modulation
UV	Ultraviolet
VA	Variable attenuator

Chapter 1 Introduction

This chapter generally introduces the background, motivation, and contribution of my research work. In Section 1.1, a brief introduction to the As_2Se_3 glass, PMMA polymer, dual-core fiber structure and tapered structure is presented. Motivations on the fabrication of the tapered dual-core As_2Se_3-PMMA fiber and its temperature and strain sensing applications and nonlinear applications such as Modulation Instability are also clarified. Section 1.2 summarizes the contributions of my work to the above areas. Section 1.3 gives the outline of the thesis.

1.1 Background and motivation

1.1.1 As_2Se_3 glass

Detection based on the mid-infrared (Mid-IR) sources has attracted extensive attention since a vast majority of gaseous chemical substances exhibit fundamental vibrational absorption bands in the mid-infrared spectral region (2-25 μm). However, as the most common optical fiber material, silica exhibits high attenuation of above 60 dB/m at wavelengths longer than 3 μm [1-3].

Chalcogenide glasses based on the elements (Sulfide (S), Selenide (Se), Telluride (Te)) have a wide transparency in infrared spectrum (IR) with the transmission window from 0.5 to 25 μm [4-6], which implies potential applications in biochemical sensors and optical communication systems [6]. Furthermore, chalcogenide glass is an excellent nonlinear medium with the intrinsic material nonlinearity (n_2) of 1.1×10^{-13} cm^2/W at 1550 nm that is 1000 times larger than that of the widespread silica glass [7-9]. Table 1-1 lists some optical parameters of silica and several chalcogenide glasses.

Device and material	Refractive index	n_2 / n_2(Silica)	Transmission Range (µm)	Minimum Loss (dB m^{-1})
Silica fiber [10]	1.44	1	0.2-3.5	0.0002 @1.55 µm
As_2S_3 fiber [11]	2.5	200	0.6-12	0.1-0.2 @ 3 µm
As_2Se_3 fiber [12]	2.9	600	1.0-16	0.55 @ 4.5 µm
Te-based fiber [13, 14]	~3.2	~1000	1.5-25	3 @10 µm

Table.1- 1. Typical optical parameters of silica fiber and several chalcogenide fibers.

Because of the transparency in Mid-IR and high material nonlinearity of chalcogenide fibers, applications based on chalcogenide fibers have been extensively developed, such as supercontinuum generation [15], ultrafast all-optical switches [16], chalcogenide glass-fiber-based mid-IR sources [17], strong stimulated Brillouin scattering [18], and slow and fast light in high nonlinear chalcogenide fibers [19].

In particular, As_2Se_3 has the potential for a wide range of applications because it has the highest n_2 among all chalcogenide glass at 1550 nm. The softening temperature of the As_2Se_3 glass is 188 ˚C that allows us to coat the As_2Se_3 glass with other material such as PMMA in the lab environment. As_2Se_3 glass with thermal expansion coefficient of $\left(dL/dT\right)/L$ $=22.4\times10^{-6}$ / ˚C and thermo-optic coefficient of dn/dT $=5\times10^{-5}$/ ˚C [20] is an excellent candidate to be utilized in temperature measurement sensors, while the thermal-expansion coefficient $\sim0.5\times10^{-6}$/˚C [21].

1.1.2 PMMA polymer

Poly (methyl methacrylate) (PMMA) is a strong and tough material, which can provide mechanical robustness and flexibility as a coating material in fibers. Its environmental stability is superior to most other plastics such as polystyrene and polyethylene, and PMMA is therefore often the material of choice for outdoor applications [22]. Furthermore, for the optical properties, PMMA transmits light from visible region to infrared region of up to 2,800 nm and the dispersion formula in [23] gives the value of refractive index is 1.478 at 1550 nm. What's more, PMMA has a maximum water absorption ratio of 0.3–0.4 % by weight [24], which can be used for developing humidity sensors. Finally, the coefficient of thermal expansion is relatively high at $\left(dL/dT\right)/L$ =22.4×10^{-4}/°C [25] and the thermo-optic coefficient of the PMMA is dn/dT =-1.20×10^{-4}/°C [25], which are potential materials for designing sensors with high sensitivity for temperature measurement.

1.1.3 Dual-core fiber structure

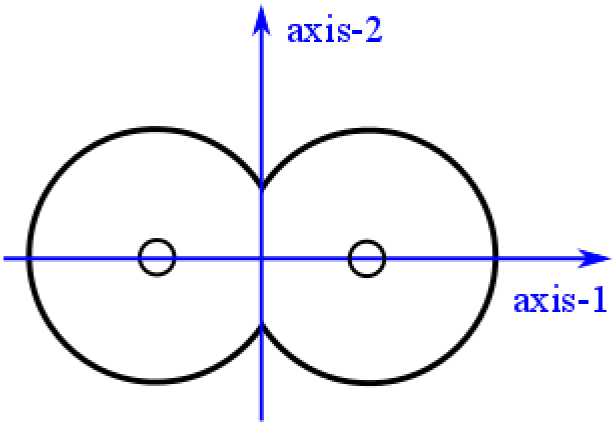

Figure 1- 1. Schematic of a dual-core structure.

Figure 1-1 shows a schematic of a dual-core structure. There are many different kinds of dual-core structure, like PCF based dual-core structure [26] and normal directional couplers [27]. Dual-core fibers are considered to be candidates of many applications such as space division multiplexing [28] and sensing applications [29-31].

Crosstalk between cores in multicore optical fibers can be analyzed using supermode theory. The supermode theory relies on the study of the composite waveguide as a whole [32]. Any light field can be represented as a sum of orthogonal states whose superposition represents an actual field distribution in a fiber. The solutions of Maxwell's equations in the dual-core fibers results in two sets of symmetric (the even mode) and antisymmetric (the odd mode) modes, so-called fundamental supermodes, for x and y polarization orientations, respectively. In one of the polarization axis, any guided electric field in the dual-core fiber can be decomposed as a superposition of the two orthogonal supermodes.

The propagation constants of these supermodes are different leading to the phase mismatch of the phase velocities, which induces along the fiber an evolution of the global field distribution. The intensity is proportional to $\cos^2[\pi z/\Lambda]$ in core 1 and $\sin^2[\pi z/\Lambda]$ in core 2, where Λ is the spatial period of intensity oscillations given by $\Lambda=2\pi/(\beta_e- \beta_o)$, β_e and β_o are the propagation constant of the even and odd modes, respectively. This can be interpreted as power coupling between the two cores as well as the spatial beating of the two corresponding supermodes. The interference effect of these supermodes is presented in Fig. 1-2(a) and Fig. 1-2(b) [32]. By definition, two orthogonal supermodes possess different phase velocities, which results in periodic switching of power between cores along the fiber. Strong power transfer between cores arises from a large spatial overlap of excited supermodes.

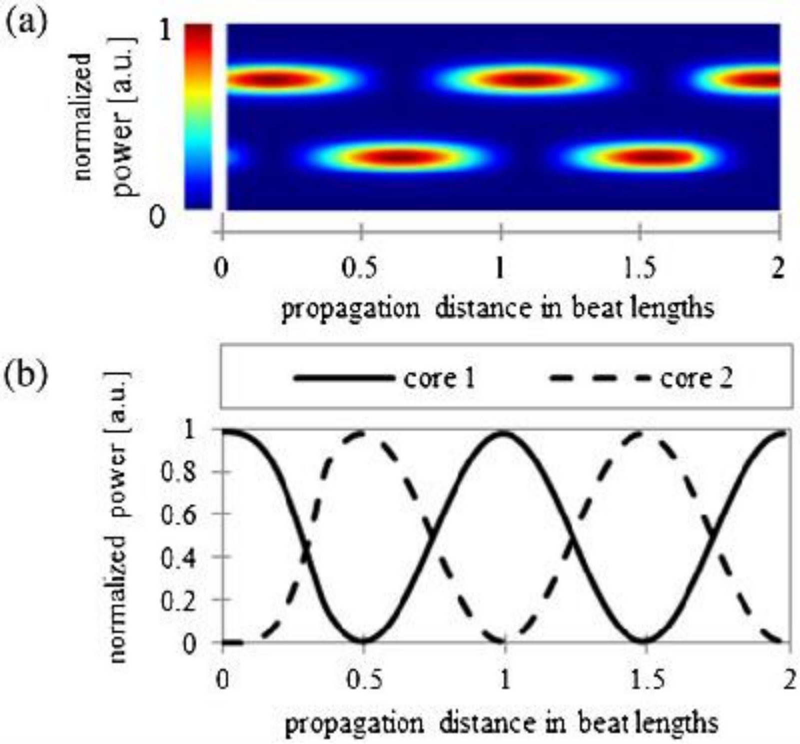

Figure 1- 2. (a) Calculated power distribution in particular cores over fiber length. (b) Normalized power in particular cores over fiber length expressed in beat lengths [31].

1.1.4 Tapered structure

The waveguide nonlinearity γ is defined as $\gamma = k_0 n_2 / A_{eff}$, where n_2 is the material nonlinearity, $k_0 = 2\pi/\lambda$ is the wave-number and A_{eff} is effective mode area. One approach to enhance the waveguide nonlinearity γ is to fabricate fiber cores using materials with high intrinsic material nonlinearity (n_2), such as the chalcogenide fibers. The other approach is to fabricate micro-wires with a large contrast for the core to cladding refractive index to reduce the effective mode area A_{eff} [33]. For example, a single-mode transmission and an ultrahigh waveguide nonlinearity with $\gamma = 176\ W^{-1}m^{-1}$ is achieved in micro-wires with As_2Se_3 core diameter of 0.45 μm by the tapering a hybrid As_2Se_3-PMMA using the heat-brush method [34]. The high intrinsic material nonlinearity of the As_2Se_3 glass, the large difference between refractive index of the As_2Se_3 core and the PMMA cladding and also the micro-wire structure contribute collectively to the ultrahigh values of γ.

1.1.5 Chalcogenide-PMMA tapers

Baker et al. successfully fabricated the first hybrid chalcogenide-PMMA taper consisting of a chalcogenide fiber core (As_2Se_3) and a Poly(methyl methacrylate) (PMMA) cladding, which enhances the mechanical strength of the chalcogenide tapers and protects it from environmental contamination and degradation [35]. The As_2Se_3 core of the taper provides an ultrahigh nonlinearity up to $\gamma = 133\ W^{-1}m^{-1}$ and the PMMA cladding provides mechanical strength of the device and reduces sensitivity to the surrounding environment. Then Ahmad et al. demonstrated the first parametric oscillator [36], the first Fabry-Perot Raman laser [37] and broadband four-wave mixing [38] based on the As_2Se_3-PMMA taper. The inscription of fiber Bragg gratings in tapered single-core As_2Se_3-PMMA fibers has also been reported utilizing photosensitivity of As_2Se_3 glass to optical signals at 1550 nm [39]. Al-Kadry et al. demonstrated a supercontinuum generation span from 960 nm to 2500 nm in a As_2S_3-PMMA with a As_2S_3 diameter of 0.58 μm and a wire section length of 3 mm [40]. Beugnot et al. have demonstrated the PMMA cladding surrounding microwire significantly reduces and controls stimulated Brillouin scattering by broadening the Brillouin linewidth and increases the threshold [41]. Godin et al. demonstrated normal dispersion modulation instability (MI) in the mid-infrared (mid-IR) spectral region by pumping a hybrid polymer-chalcogenide optical micro-wire with a diameter of 3.6 μm and a wire section length of 14 cm [42]. Finally, Al-Kadry et al. demonstrated mode-locked laser based on an As_2S_3-PMMA taper with a As_2S_3 diameter of 1.7 μm and a taper length of 10 cm [40].

1.1.6 Motivation of fabrication of tapered dual-core As_2Se_3-PMMA fiber

Our motivation for fabrication of tapered dual-core As_2Se_3-PMMA fiber is to investigate the applications and the nonlinear effect in near-IR and Mid-IR in the As_2Se_3-PMMA micro-wires due to the combination of high intrinsic material nonlinearity, the micro-wire structure and thermal/strain induced properties.

1.2 Thesis contribution

This thesis introduces the fabrication procedure of the tapered As_2Se_3-PMMA fibers and extends the applications of the As_2Se_3-PMMA taper to the high sensitivity temperature and strain sensing and the nonlinear applications such as modulation instability and guided acoustic wave Brillouin scattering. Major contributions of this thesis include:

(1) The fabrication procedure of the hybrid As_2Se_3-PMMA tapers is described.

(2) An approach for high-sensitivity simultaneous temperature and strain measurement in a dual-core As_2Se_3-PMMA taper with As_2Se_3 core diameter of 0.55 μm utilizing the intrinsic material properties of As_2Se_3 and PMMA is proposed and demonstrated. High measurement sensitivity is achieved by combining the large thermal-expansion coefficient of the PMMA cladding, the low stiffness of the micron diameter As_2Se_3 core, and the large difference between the refractive-indices of As_2Se_3 and PMMA. High measurement sensitivities of -115 pm/ºC, -4.21 pm/με are measured from the transmission spectrum of one principal polarization axis of the dual-core fiber, -35.5 pm/ºC and -3.16 pm/με are obtained from the transmission spectrum of the second polarization axis of the dual-core fiber. Decorrelation between the temperature and strain measurement sensitivities of the principal polarization axes is achieved through thermally induced squeezing of the As_2Se_3 cores by the PMMA cladding due to an order of magnitude difference between the thermal-expansion coefficients

of As_2Se_3 and PMMA, enabling simultaneous measurement of temperature and strain variations with temperature and strain uncertainty of 0.15 ºC and 1.87 με.

(3) A temperature-insensitive strain sensor is proposed and demonstrated based on a dual-core As_2Se_3-PMMA taper with As_2Se_3 core diameter of 0.61 μm utilizing the thermal forces on the As_2Se_3 cores by the PMMA cladding. Longitudinal and transverse forces on the As_2Se_3 cores are induced by thermal expansion/contraction of the PMMA cladding due to an order of magnitude difference between the thermal expansion coefficients of As_2Se_3 and PMMA. At an optimal PMMA layer thickness, the wavelength shift caused by the thermally-induced forces on the refractive-index of the dual-core fiber cores counterbalances that caused by the thermally-induced fiber length variation leading to temperature insensitive transmission. Temperature-insensitive strain measurement over a temperature range from 30°C to 40°C is demonstrated in a dual-core As_2Se_3-PMMA fiber with an As_2Se_3 core diameter of 0.61 μm and a PMMA cladding diameter of 34.4 μm. Thermally-induced forces in hybrid fibers open the path towards the realization of novel sensors and devices that are immune to temperature fluctuations.

(4) We demonstrate an approach for high-sensitivity temperature and strain measurement in a dual-core As_2Se_3-PMMA taper with a large As_2Se_3 core diameter of 2.5 μm that provides a small value of $\partial\phi_d(\lambda)/\partial\lambda$ and large thermal forces. The variation of the difference between phases of the two modes with respect to wavelength ($\partial\phi_d(\lambda)/\partial\lambda$) becomes small as the As_2Se_3 core diameter increases, and consequently, thermally-induced and strain-induced change of the difference between phases of the two modes $\phi_d(\lambda)$ leads to a large wavelength shift indicating enhancement of the temperature and strain measurement sensitivity. Furthermore, thermally-induced longitudinal and transverse forces on the As_2Se_3 cores further enhance the temperature measurement sensitivity. High sensitivities of 436 pm/°C, -6.23 pm/μ**ε** and 572

pm/°C and -3.63 pm/μ**ε** from the transmission spectra of axis-1 and axis-2 in the dual-core As_2Se_3-PMMA taper are obtained.

(5) We report for the first time that transmission of optical pulses centered at a wavelength of 1550 nm through a tapered dual-core As_2Se_3-PMMA fiber inscribes an antisymmetric long-period grating. The pulse power is equally divided between even and odd modes that superpose along the dual-core fiber to form an antisymmetric intensity distribution. A permanent refractive-index change that matches the antisymmetric intensity distribution is inscribed due to photosensitivity at the pulse central wavelength. The evolution of the transmission spectrum of the dual-core fiber is experimentally measured as the accumulated time that the fiber is exposed to the pulse is increased. A theoretical model of an antisymmetric long-period grating in a dual-core fiber computationally reproduces the experimentally observed evolution of the transmission spectrum. Experimental results indicate that antisymmetric long-period gratings induce effective group-velocity matching between the even and odd modes of the dual-core fiber, and reveal for the first time that long-period gratings can lead to slow light propagation velocities.

(6) Based on effective group-velocity matching between the even and odd modes of a dual-core As_2Se_3-PMMA taper on which an antisymmetric long-period grating is inscribed, we propose and demonstrate an approach for temperature-sensitivity enhancement by a factor of 4.0. The transmission of optical pulses in the dual-core As_2Se_3-PMMA taper inscribes the antisymmetric long-period grating that causes the electric fields to couple back and forth between the even and odd modes leading to effective group-velocity matching between the two modes. The variation of the difference between phases of the two modes with respect to wavelength tends to 0 ($\partial\phi_d(\lambda)/\partial\lambda \rightarrow 0$) near the resonance wavelength of the grating due to the effective group-velocity matching between the two modes, and consequently, thermally-

induced change of the difference between phases of the two modes $\phi_d(\lambda)$ leads to a large wavelength shift indicating enhancement of the temperature measurement sensitivity. The sensitivity of temperature measurement in the wavelength range with effective group velocity matching is enhanced by a factor of 4.0 in comparison with that in the wavelength range that does not have effective group velocity matching. The effective group-velocity matching between modes in fibers opens the path towards the realization of novel high-sensitivity sensors for temperature and strain measurement.

(7) We report the first observation of modulation-instability in the normal-dispersion regime of a dual-core As_2Se_3-PMMA fiber. The modulation instability spectrum shows multiple peaks arising from the strong wavelength dependence of the coupling coefficient. Modulation instability in dual-core fibers can be used for enhanced parametric amplification, broadly tunable lasers, and efficient entangled photon generations.

(8) We review the recent work about the forward stimulated Brillouin scattering and its sensing applications. The forward stimulated Brillouin scattering by the radial guided acoustic modes of silica fibers and tapered dual-core As_2Se_3-PMMA fibers is investigated experimentally and the preliminary results are presented. Sensing applications such as the acoustic impedance of the surrounding medium and taper dimension characterization can be achieved based on cavity lifetime measurements of multiple modes due to the acoustic reflectivity at the outer cladding boundary.

1.3 Thesis outline

This thesis contains eleven chapters and is organized as follows:

Chapter 1 reviews the background of the As_2Se_3 glass, PMMA polymer, dual-core structure and tapered structure.

Chapter 2 gives a theoretical model for temperature and strain measurement in a dual-core As_2Se_3-PMMA taper.

Chapter 3 presents the fabrication procedure of hybrid As_2Se_3-PMMA tapers.

Chapter 4 includes three parts: (1) high-sensitivity simultaneous temperature and strain measurement in a dual-core As_2Se_3-PMMA taper with As_2Se_3 core diameter of 0.55 μm utilizing the intrinsic material property of As_2Se_3 and PMMA. (2) investigation of the thermal forces in a dual-core As_2Se_3-PMMA taper. A temperature-insensitive strain sensor is demonstrated based on a dual-core As_2Se_3-PMMA taper with As_2Se_3 core diameter of 0.61 μm utilizing the thermal forces on As_2Se_3 cores by the PMMA cladding. (3) high-sensitivity temperature and strain measurement in a dual-core As_2Se_3-PMMA taper with a large As_2Se_3 core diameter of 2.5 μm, which provides a small value of $\partial\phi_d(\lambda)/\partial\lambda$ and large thermal forces.

Chapter 5 includes two parts: (1) the inscription of an antisymmetric long-period grating by the transmission of optical pulses is investigated in a tapered dual-core As_2Se_3-PMMA fiber. Experimental results indicate that antisymmetric long-period gratings induce effective group-velocity matching between the even and odd modes of the dual-core fiber, and reveal for the first time that long-period gratings can lead to slow light propagation velocities. (2) an approach for temperature-sensitivity enhancement by a factor of 4.0 is demonstrated based on effective group-velocity matching between the even and odd modes of a dual-core As_2Se_3-PMMA taper on which an antisymmetric long-period grating is inscribed.

Chapter 6 demonstrates modulation instability within the normal-dispersion regime in dual-core As_2Se_3-PMMA fiber.

Chapter 7 reviews the recent work about the forward stimulated Brillouin scattering and its sensing applications. The radial and torsional-radial guided acoustic modes of silica fibers and tapered dual-core As_2Se_3-PMMA fibers are investigated experimentally and the preliminary results are presented.

Chapter 8 concludes all the work in this thesis and proposes possible directions for future research.

Chapter 2 Theoretical model for temperature and strain measurement in a dual-core As_2Se_3 -PMMA taper

In this chapter, a theoretical model for temperature and strain measurement in a dual-core As_2Se_3-PMMA taper is given. Theoretical analysis shows that wavelength shift of the transmission spectrum is linearly proportional to temperature and strain variations in the dual-core tapered fiber enabling measurement of these physical parameters. The wavelength shift induced by temperature and strain variation is related to $\partial\phi_d(\lambda)/\partial\lambda$ (the variation of the difference between phases of the even and odd modes with respect to wavelength), L_w (length of the fiber) and Δn_{eff} (the refractive indices difference between the even and odd modes). For temperature measurement, α_T (thermal expansion coefficient) and γ_{TIF} (the variation of $\Delta n_{eff,T}$ by thermally-induced forces) are another factors changing the wavelength shift in the transmission spectrum. For strain measurement, the low stiffness (α_ε) of the fiber materials enhances the sensitivity. The parameters, $\partial\phi_d(\lambda)/\partial\lambda$, L_w, Δn_{eff}, γ_{TIF} can be manipulated by designing the fibers to achieve different applications, of which the applications are reported in the following chapters.

2.1 Background

Optical fiber sensors have shown significant advantages and drawn an intensive attention worldwide due to its low loss feature, the geometric versatility, small size and light weight, which guarantees a high quality of the optical signals. With the immunity to external electromagnetic fields, optical fiber sensors have high sensitivities to external physical perturbations such as temperature and strain variations.

Point sensors as one of optical fiber sensors measure the changes of the physical parameters at a localized area. With the advantages of low cost, high sensitivity, easy fabrication, and compactness, various point fiber sensors have been proposed based on different kinds of techniques and algorithms, such as fiber Bragg grating, Fabry-Perot interferometer and Mach-Zehnder interferometer. Temperature and strain sensing based on the dual-core As_2Se_3-PMMA tapers can be categorized into the technique based on a Mach-Zehnder interferometer. Table 2.1 lists several kinds of fiber Mach-Zehnder interferometers and their applications.

Sensor Type	Fiber Type	Measurands	Sensing Performance
Tapered MZI	SMF	Simultaneous Strain and RI [43]	1590 nm/RIU, -0.060 nm/με
		Simultaneous temperature and RI[44]	26.087nm/RIU , 0.077 nm/°C
Core-mismatch MZI	SMF-MMF-SMF	Temperature [45]	0.0142nm/°C
		Strain[45]	0.007 nm/ με
	SMF-SMF-SMF	RI [46]	28.6nm/ RIU
LPG MZI	LPG-SMF-LPG	Temperature [47]	----
	PCF	Strain [48]	----

Table.2- 2. Fiber Mach-Zehnder interferometers and their applications.

2.2 Analytical model

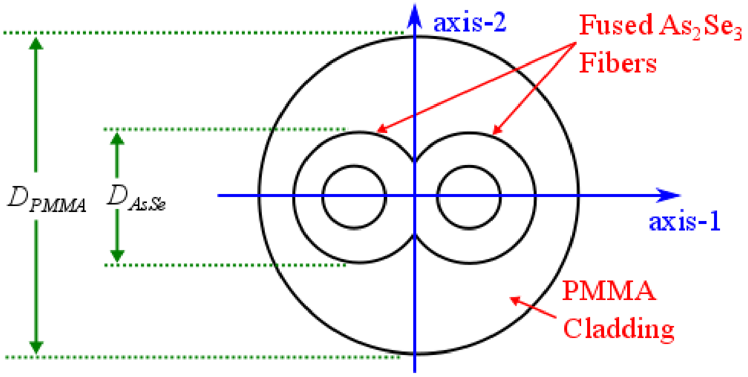

Figure 2- 1. A schematic of the dual-core As_2Se_3-PMMA fiber.

Figure 2-1 presents the schematic of the cross-section of a dual-core As_2Se_3-PMMA fiber illustrating two fused As_2Se_3 fibers surrounded by a PMMA layer. The asymmetric geometrical structure of a dual-core fiber with respect to axis-1 (x-axis) and axis-2 (y-axis) leads to strong birefringence with two distinct principal polarization axes [49, 50].

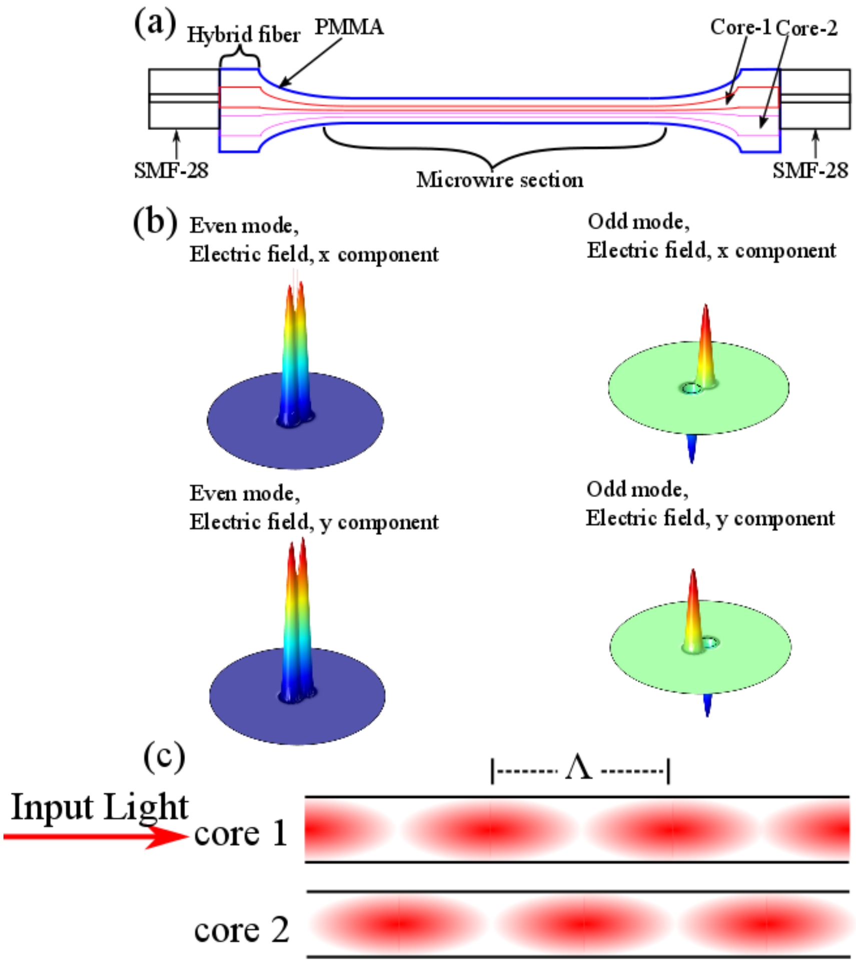

Figure 2- 2. (a) Schematic of a dual-core As_2Se_3-PMMA taper coupled to SMF-28 fibers. (b) The calculated distribution of electric fields of even and odd modes in x-axis and y-axis. (c) Illustration of spatial power distribution in a dual-core fiber when light is launched into core-1.

Figure 2-2(a) shows the different sections of a dual-core As_2Se_3-PMMA taper whose ends are permanently butt-coupled to SMF-28 fibers using UV-cured epoxy. As presented in Fig. 2-2(b), strong birefringence with two distinct principal polarization axes is induced by the geometrical structure with two distinct axes of symmetry and a dual-core fiber sustains two supermodes, an even mode for which the transverse electric field vectors in both cores have the same direction, and an odd mode where the transverse electric field vectors in the fiber cores have opposite directions [49]. The distribution of electric fields of the even and odd modes in two axes of a typical dual-core fiber are calculated using the Comsol Multiphysics software. When the light is launched into core-1 of a dual-core fiber, for each principal polarization axis, the power is split equally between the even and odd modes that superpose along the fiber to form an antisymmetric period spatial power distribution as presented in Fig. 2-2(c).

As presented above, a dual-core fiber sustains distinct principal polarization axes and for each axis there are two main modes, an even mode and an odd mode [50]. When light is launched at the input of core-1 of the dual-core fiber, the even mode and the odd mode are excited equally. For each principal axis, the output radiation pattern is a superposition of the fields of the even and odd modes and is given by

$$E = \sqrt{0.5}a_e \exp\left(j2\pi n_{eff}^{e} L_w / \lambda\right) + \sqrt{0.5}a_o \exp\left(j2\pi n_{eff}^{o} L_w / \lambda\right).$$

The intensity at the output of core-1 is given by

$$I = 0.5\left|a_e\right|^2 + 0.5\left|a_o\right|^2 + \left|a_e\right|\left|a_o\right|\cos\left(\phi_d\left(\lambda, T\right)\right),$$

where $\phi_d\left(\lambda, T\right) = 2\pi\Delta n_{eff} L_w / \lambda + \theta_e - \theta_o$, $\Delta n_{eff} = n_{eff}^{e} - n_{eff}^{o}$, a_i is the complex amplitude with i being e for the even-mode or o for the odd-mode, θ_i is the phase of a_i, and L_w is the length of the dual-core taper waist.

Troughs are observed in the transmission spectrum of a tapered dual-core fiber when the difference between the phases of the even and odd modes satisfies the condition $\phi_d(\lambda, T) = (2m+1)\pi$, where m is an integer. Changes in the temperature of the fiber taper lead to change in the phase-difference ϕ_d given by

$$\Delta\phi_d\left(\lambda, T\right) = \left(\partial\phi_d / \partial\lambda\right)\Delta\lambda + \left(\partial\phi_d / \partial T\right)\Delta T .$$

The phase-difference at the m^{th} trough in the transmission spectrum is always $\phi_d(\lambda,T)$ = $(2m+1)\pi$; hence, as temperature changes from T to $T+\Delta T$, the m^{th} trough shifts from wavelength $\lambda_{m,T}$ to wavelength $\lambda_{m,T+\Delta T} = \lambda_{m,T} + \Delta\lambda_{m,T}$ such that

$$\phi_d\left(\lambda_{m,T}, T\right) = \phi_d\left(\lambda_{m,T} + \Delta\lambda, T + \Delta T\right) = (2m+1)\pi$$

leading to

$$\Delta\lambda_{m,T} = -\left(\partial\phi_d / \partial\lambda\right)^{-1}\left(\partial\phi_d / \partial T\right)\Delta T .$$

Using

$$\partial\phi_d / \partial T = \left(2\pi / \lambda\right)\left(L_w \partial\Delta n_{eff} / \partial T + \Delta n_{eff} \partial L_w / \partial T\right),$$

the wavelength-shift of troughs becomes

$$\Delta\lambda_{m,T} = -\left(\partial\phi_d / \partial\lambda\right)^{-1} k_0 L_{w,T} \Delta n_{eff,T}\left(\alpha_T + \gamma_T\right)\Delta T \qquad (2.1)$$

where $\Delta n_{eff,T}$ is the refractive indices difference between the even and odd modes, $L_{w,T}$ is the taper length, $\alpha_T = (1/L_{w,T})(\partial L_{w,T}/\partial T)$, and $\gamma_T = (1/\Delta n_{eff,T})(\partial\Delta n_{eff,T}/\partial T)$.

The large difference of thermal expansion coefficients between PMMA cladding with $\alpha_{PMMA} = 2.02\times 10^{-4}$ /°C [25] and the As_2Se_3 cores with $\alpha_{AsSe} \sim 0.2\times10^{-4}$ /°C [51] leads to thermally-induced transverse and longitudinal forces on the As_2Se_3 cores. When temperature increases, the PMMA cladding transversely and longitudinally expands the As_2Se_3 core, and when temperature decreases, the PMMA layer transversely and longitudinally squeezes the As_2Se_3 cores. Taking into account the thermally-induced forces, the variation of $\Delta n_{eff,T}$ with temperature is expressed as

$$\gamma_T = \gamma_{TO} + \gamma_{TIF}$$

where γ_{TO} and γ_{TIF} arise from the variation of $\Delta n_{eff,T}$ by the thermo-optic effect, and thermally-induced forces, respectively. Quantifying γ_{TIF} is difficult since it must be performed numerically and thermally-induced longitudinal and transverse forces are not uniform in the fiber cross section. The value of thermal expansion coefficient of the fiber α is positive, lies between values of the thermal expansion coefficients of As_2Se_3 and PMMA, and depends on the diameter of the As_2Se_3 cores and the thickness of the PMMA cladding. For small As_2Se_3 cores as is the case in tapered dual-core fibers, the value of α is mainly determined by the thickness of the PMMA layer. For a thick PMMA layer, the value of α is the same as the thermal expansion coefficient of PMMA because the stiffness of the thick PMMA layer is higher than that of the As_2Se_3 cores, but for a thin PMMA layer the value of α is the same as the thermal expansion coefficient that of As_2Se_3 because the stiffness of the PMMA layer is lower than that of the As_2Se_3 cores. Furthermore, the value of γ can become negative due to the presence of thermally-induced forces, and at an optimal PMMA layer thickness, the magnitude of γ becomes large enough such that $\alpha + \gamma = 0$ leading to $\Delta\lambda_{m,T} = 0$, which indicates temperature insensitive transmission for the dual-core As_2Se_3-PMMA fiber. Finally, the negative value of γ can become further small when the diameter of the PMMA cladding is further increased such that ($\alpha+\gamma < 0$) leading to $\Delta\lambda_{m,T} > 0$ which makes the transmission spectrum of the troughs shift towards longer wavelength when temperature increases ($\Delta T>0$).

Similarly, the wavelength shift $\Delta\lambda_{m,\mathcal{E}}$ due to the imposed strain is given by

$$\Delta\lambda_{m,\varepsilon} = -\left(\partial\phi_d / \partial\lambda\right)^{-1} k_0 L_{w,\varepsilon} \Delta n_{eff,\varepsilon} \left(\alpha_\varepsilon + \gamma_\varepsilon\right)\Delta\varepsilon \qquad (2.2)$$

where $\alpha_{\mathcal{E}} = (1/L_{w,\mathcal{E}})(\partial L_{w,\mathcal{E}}/\partial\mathcal{E})$, $\gamma_{\mathcal{E}} = (1/\Delta n_{eff,\mathcal{E}})(\partial\Delta n_{eff,\mathcal{E}}/\partial\mathcal{E})$. Variation of the taper temperature or strain changes L_w and Δn_{eff}, shifting the trough wavelengths in the transmission spectrum. Transmission spectrum of the troughs shift towards longer or shorter wavelength based on the sign of $(\alpha_T + \gamma_T)$ or $(\alpha_{\mathcal{E}} + \gamma_{\mathcal{E}})$ since the values of $\partial\phi_d/\partial\lambda$, L_w, and Δn_{eff} are all positive.

2.3 Numerical simulations

2.3.1 $\partial\phi_d/\partial\lambda$ changes with As_2Se_3 core diameter

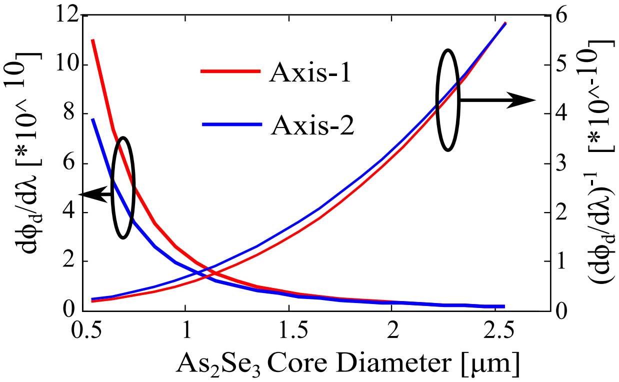

Figure 2- 3. Calculated values of $\partial\phi_d/\partial\lambda$ and $(\partial\phi_d/\partial\lambda)^{-1}$ as a function of As_2Se_3 core diameter. Red line: Axis-1; blue line: Axis-2.

Figure 2-3 shows the calculated values of $\partial\phi_d/\partial\lambda$ as a function of diameter of As_2Se_3 core using Comsol Multiphysics software. The value of $\partial\phi_d/\partial\lambda$ decreases with the diameter of the As_2Se_3 cores. According to Eq. (2.1) and (2.2), a small value of $\partial\phi_d/\partial\lambda$ induces a large wavelength shift of the transmission spectrum of the dual-core fiber when temperature and strain change.

2.3.2 Δn_{eff} changes with As_2Se_3 core diameter of the taper

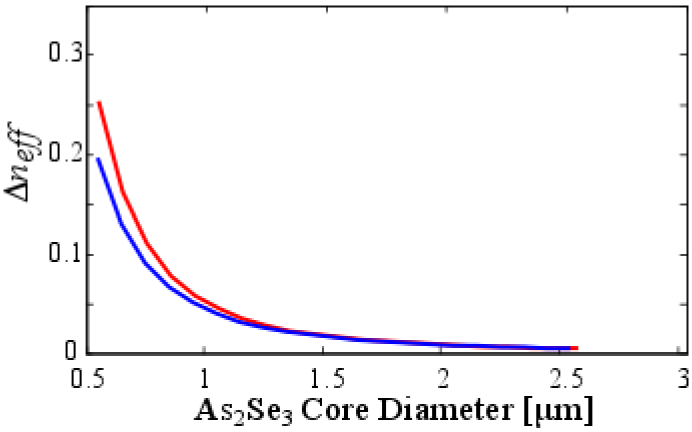

Figure 2- 4. Calculated values of Δn_{eff} as a function of As_2Se_3 core diameter. Red line: Axis-1; blue line: Axis-2.

Figure 2-4 shows the calculated values of Δn_{eff} as a function of diameter of As_2Se_3 core using Comsol Multiphysics software. The value of Δn_{eff} decreases with the diameter of the As_2Se_3 cores.

Chapter 3 Fabrication of hybrid dual-core As_2Se_3-PMMA tapers

This chapter presents the fabrication procedure of hybrid chalcogenide-polymer tapers, which includes preparation of the As_2Se_3 fibers and PMMA tubes, preform fabrication, fiber drawing, polishing and coupling process and micro-wire fabrication. The setups and fibers in every step are given.

3.1 As_2Se_3 fiber and PMMA micro-tube preparation

The commercial As_2Se_3 fibers with the As_2Se_3 core diameter of 96 μm, the cladding diameter of 170 μm and a numerical aperture of 0.18 are provided by Coractive High-Tech company. Two 7-cm long fibers are cut, put in the oven for 2 hours with the oven temperature of 150 ˚C and immersed in the acetone to remove the coating of the fibers.

A 20 cm-long PMMA tube with an inner diameter of 5 mm and an outer diameter of 9.5 mm is annealed in the oven to remove the internal stresses frozen in the solid PMMA tubes. The annealing process requires one hour in the oven with the oven temperature of 150 ˚C.

3.2 Fabrication of the Preform

The dual-core As_2Se_3-PMMA fibers are fabricated using a rod-in-tube method. Two As_2Se_3 fibers are inserted into a PMMA tube, as illustrated in Fig. 3-1(a). The assembly is mounted horizontally on a lathe that is rotating at a rate of 3 rotations/min, as illustrated in Fig. 3-1(b). The PMMA tube is heat-softened using an electrical resistive heater at a temperature of 220 ˚C moving back and forth along the PMMA tube at a velocity of 1 μm/s.

Surface tension causes the PMMA tube to collapse on the As_2Se_3 fibers to obtain an As_2Se_3-PMMA fiber preform. Figure 3-1(c) presents an image of a hybrid fiber preform.

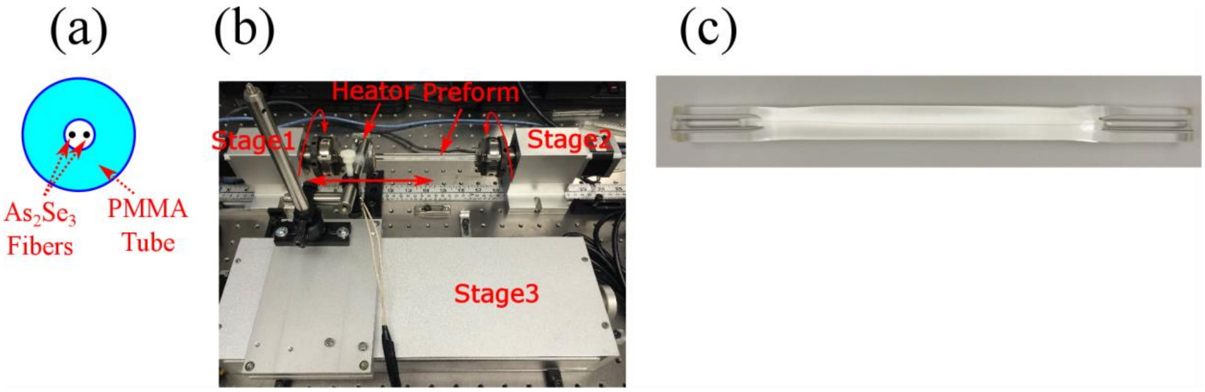

Figure 3- 1. Preform fabrication setup.

3.3 Preform drawing

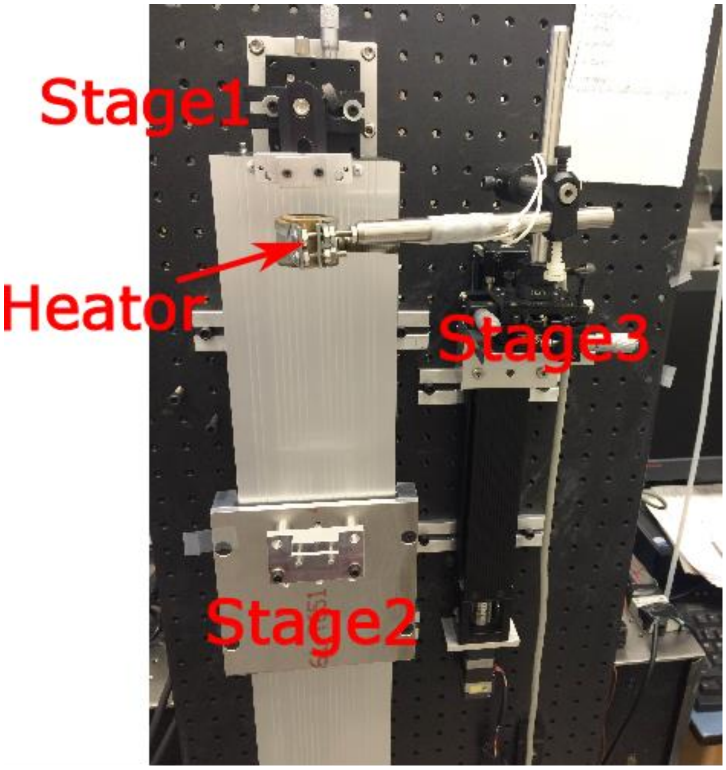

Figure 3- 2. Drawing setup.

The As_2Se_3-PMMA preform is drawn using the drawing setup shown in Fig. 3-2 to get hybrid fibers. In this process, the preform is slowly inserted at a constant velocity into a furnace that heats the preform to a softening point, and the micro-tube is drawn at a higher velocity from the other side of the furnace with a ratio of 0.125. This causes the soft part to elongate and a micro-tube with a scaled down cross-section pattern results from the preform with PMMA diameter of 1.2 mm, As_2Se_3 core diameter of 12 µm and As_2Se_3 cladding diameter of 21.25 µm. The As_2Se_3 core diameter of 12 µm (the ratio of 0.125) is selected to maximize coupling efficiency between the fundamental mode of a step-index As_2Se_3 fiber and fundamental mode of a standard single-mode step-index silica fiber (SMF-28e). The PMMA cladding diameter is sufficiently large to allow handling, polishing of the hybrid micro-taper and coupling with the SMFs without damage. Figure 3-3 shows an image of a dual-core As_2Se_3-PMMA fiber with the fiber length of 7 cm.

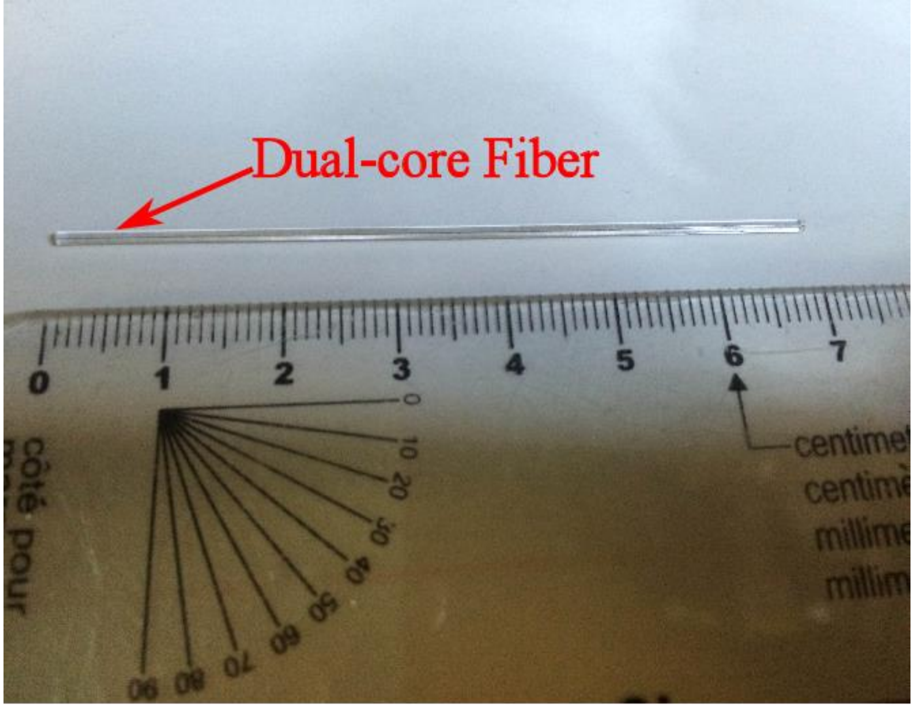

Figure 3- 3. An image of a dual-core As_2Se_3-PMMA fiber.

3.4 Polishing Hybrid Fibers

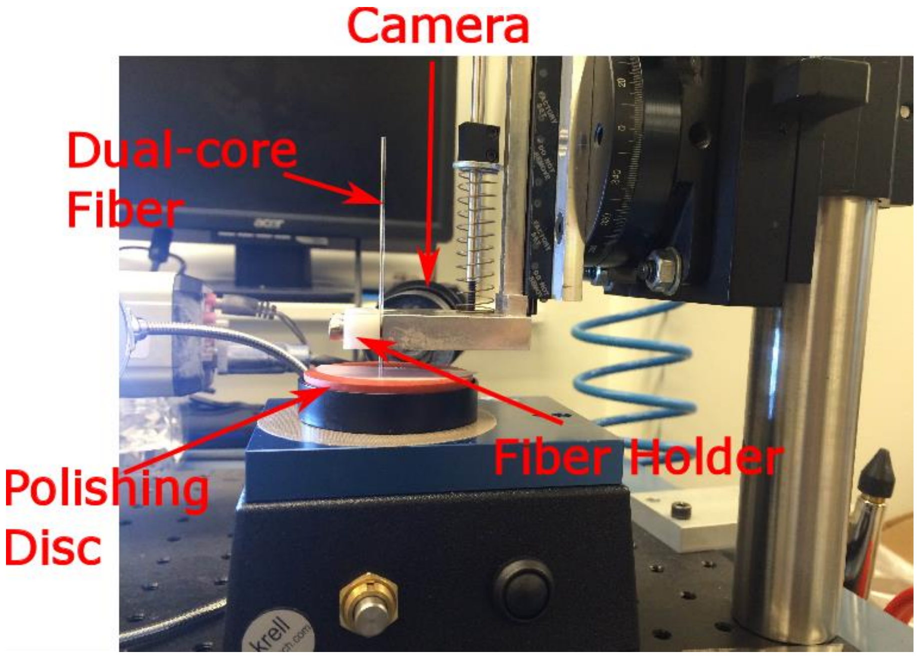

Figure 3- 4. Fiber polishing setup.

Figure 3-4 shows the setup used to polish the end facets of hybrid fibers. The polishing setup consists of a rotating polishing disc on which polishing paper is placed, a fiber holder to hold the fiber perpendicular or at a certain angle to the polishing disc surface, and a camera to monitor the fiber tip as it is being polished. A translation stage is used to approach the fiber tip to the rotating polishing disc. The polishing process is performed for six stages in which polishing paper with particles sizes of 20 μm, 9.0 μm, 3.0 μm, 1.0 μm, 0.5 μm, and 0.3 μm are used. Figure 3-5 presents an image of the polished end of the dual-core fiber showing the fused As_2Se_3 fibers and the surrounding PMMA cladding.

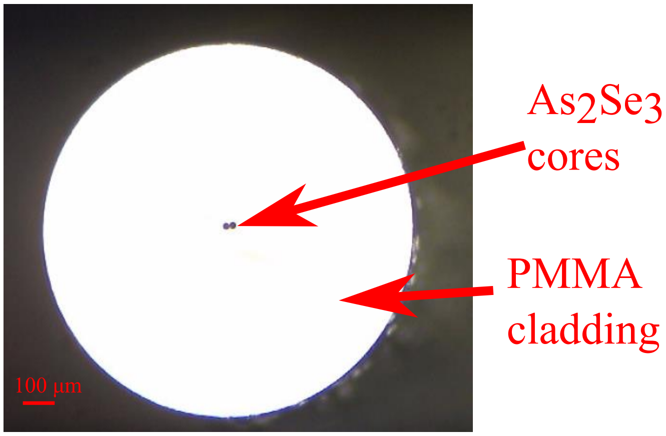

Figure 3- 5. An image of the polished end of the dual-core fiber showing the fused As_2Se_3 fibers and the surrounding PMMA cladding.

3.5 Coupling process

The coupling setup consists mainly of two alignment stages, a camera connected to a screen, a microscope, and a UV lamp, as shown in Fig. 3-6. The first alignment stage is used to launch a broadband light from a single mode fiber into the core of the hybrid fiber. The output end of the fiber is observed using a camera connected to a screen to monitor the alignment process and ensure that light is coupled into the core. The output end of the hybrid fiber is then transferred to a second alignment stage to be coupled to a receiving SMF fiber, which in turn is connected to a power meter. The core of the receiving fiber is aligned to maximize the power measured at the power meter. Further fine-tuning of alignment stages is performed to maximize the power measured at the power meter, which indicates optimal coupling into and out of the hybrid fiber. UV cured epoxy is then used to permanently fix the input and output end of the hybrid fiber to the launching and receiving SMFs.

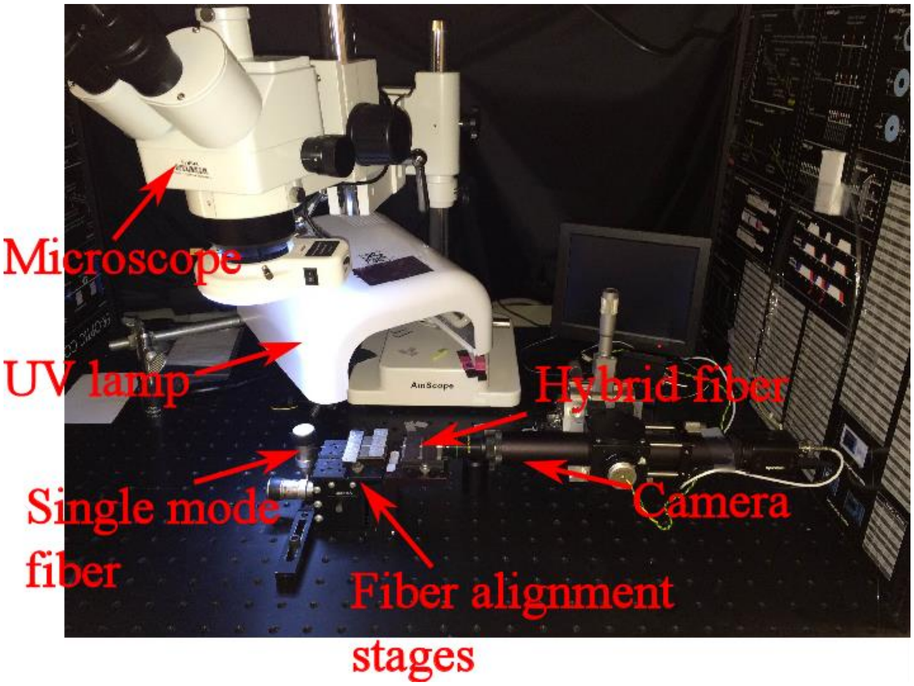

Figure 3- 6. Coupling setup.

3.6 Micro-wire Fabrication

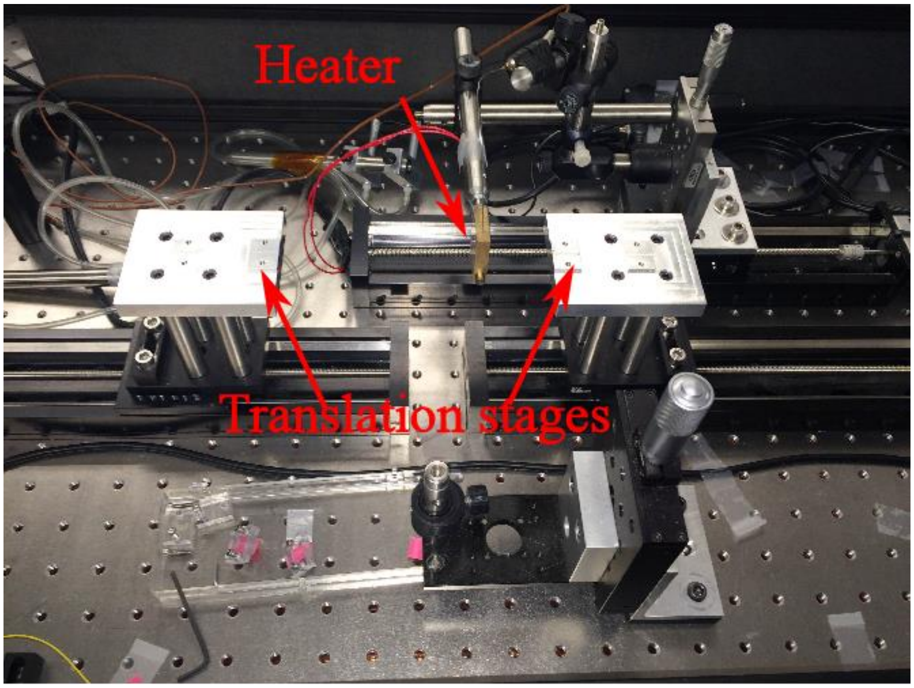

Figure 3- 7. Fiber tapering setup.

Figure 3-7 presents an image of the setup used for tapering hybrid fibers to obtain micro-wires. The tapering setup consists of three motorized translation stages and a resistive heater with a temperature controller. The resistive heater with the temperature controller is used to heat the hybrid fiber to the softening point, two of the motorized translation stages are used to stretch the fiber, and the third one is used to sweep the heater along the fiber length back and forth. This setup allows for precise control of the micro-taper profile including the transition regions and the diameter of the micro-wire section by tapering the fiber over multiple sweeps. Given a specific micro-taper profile, a Matlab program is used to generate a set of files containing information describing each tapering sweep. Then, a Lab-View program reads the files generated by the Matlab program and uses the information stored in them to control the motorized translation stages and fabricate a micro-taper with the prescribed profile.

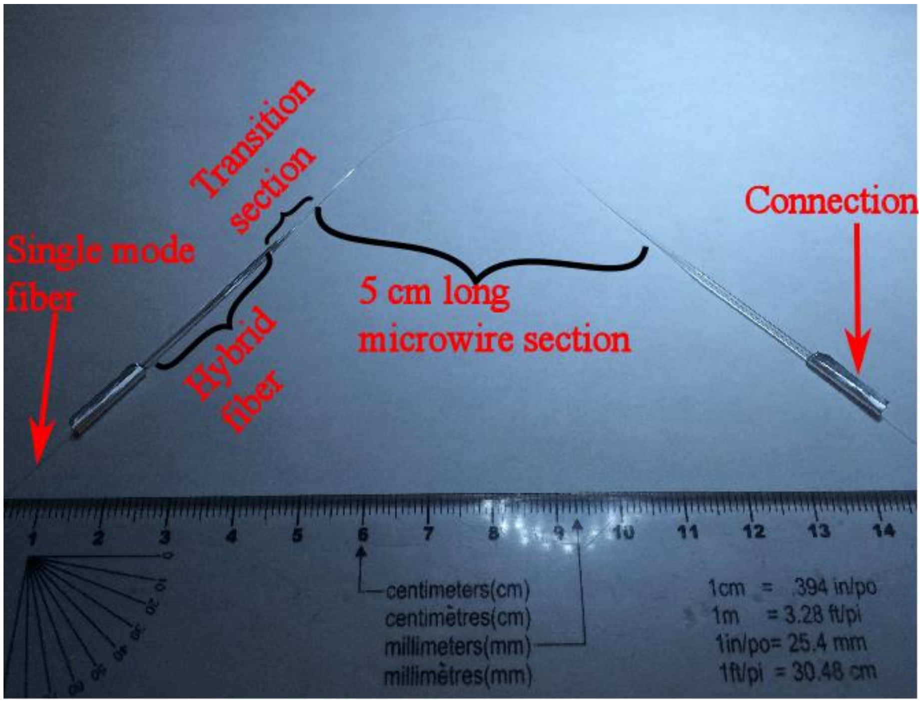

Figure 3- 8. An image of a micro-taper.

The hybrid fiber is tapered adiabatically at a temperature of 190 ℃ until the As_2Se_3 core diameter in the micro-wire section of the hybrid micro-taper reaches the target diameter. A hybrid micro-taper is fabricated with micro-wire section length of 7.0 cm, an As_2Se_3 core diameter of 21.25 μm, and a PMMA cladding diameter of 1.2 mm. Figure 3-8 shows an image of a micro-taper whose ends are permanently butt-coupled to SMF-28 fibers using UV-cured epoxy. Various sections of a dual-core As_2Se_3-PMMA taper are labeled including single mode fiber (SMF), the connection between SMFs and hybrid fibers, hybrid fibers, transition sections and 5 cm-long micro-wire section.

Chapter 4 Experimental investigation for temperature and strain measurement in dual-core As_2Se_3-PMMA tapers

In this chapter, the performance of temperature and strain measurement in dual-core As_2Se_3-PMMA tapers is investigated experimentally. This chapter includes three parts: (1) high-sensitivity simultaneous temperature and strain measurement in a dual-core taper with As_2Se_3 core diameter of 0.55 μm utilizing the intrinsic material property of As_2Se_3 and PMMA; (2) a temperature-insensitive strain sensor based on a dual-core taper with As_2Se_3 core diameter of 0.61 μm utilizing the thermal forces on As_2Se_3 cores by the PMMA cladding; (3) sensitivity enhancement for temperature and strain measurement in a dual-core taper with a large As_2Se_3 core diameter of 2.5 μm.

4.1 High-sensitivity simultaneous temperature and strain measurement

We propose and demonstrate high-sensitivity temperature and strain measurement in a dual-core As_2Se_3-PMMA taper with As_2Se_3 core diameter of 0.55 μm utilizing the intrinsic material property of As_2Se_3 and PMMA. Theoretical analysis shows that wavelength shift in the transmission spectrum is linearly proportional to temperature and strain variations in the dual-core tapered fiber enabling measurement of these physical parameters. High measurement sensitivities are observed for both principal polarization axes of the tapered dual-core As_2Se_3-PMMA fiber with temperature sensitivities of -115 pm/ºC for axis-1, -35.5 pm/ºC for axis-2, and strain sensitivities of -4.21 pm/με for axis-1 and -3.16 pm/με for axis-2. A character matrix $M_{T,\varepsilon}$ is defined to simultaneously determine variations in temperature and strain from the wavelength shifts of the transmission spectra of the principal polarization axes.

4.1.1 Background

Optical fiber sensors have attracted a lot of interest for a variety of applications including temperature monitoring [52, 53], strain measurement [54], refractive-index measurement [55, 56], structural-health monitoring [57], and detection of molecular or biomolecular binding [58, 59]. Discrimination between temperature and axial strain has been reported using long-period gratings (LPG) [60], modified fiber Bragg gratings (FBG) [61], and hybrid LPG-FBG structures [62, 63]. However, a typical full width at half maximum of a resonance peak of an LPG and an FBG is on the order of a nanometer, which limits the measurement accuracy. Using multimode fibers for temperature and strain sensing has also been reported [64, 65], but the low contrast of the beat spectrum of two modes makes the measurement of the spectral shift difficult. Fiber Mach-Zehnder interferometers [66, 67] have also been proposed for temperature and strain measurement, but silica fibers and tapers are fragile making their usage difficult in practical applications.

4.1.2 Principle

As discussed in Chapter 2, the temperature and strain sensors are implemented by the measurement of the wavelength shift of the spectrum caused by the thermally/strain-induced refractive-index change and thermally/strain-induced fiber length variation. A dual-core fiber sustains two distinct principal polarization axes and for each axis the wavelength shift of the transmission spectrum is given by Eqs. (2.1) and (2.2) in Chapter 2.

Variation of the taper temperature or strain changes L_w and Δn_{eff}, shifting the trough wavelengths in the transmission spectrum. Due to the large thermal-expansion coefficient of the PMMA cladding and a low stiffness of the As_2Se_3 micron-diameter cores, the dual-core fiber exhibits high-sensitivity for temperature and strain measurement.

4.1.3 Temperature and strain measurement setup and results

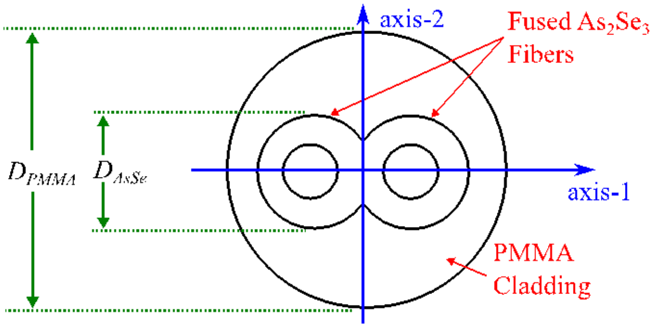

Figure 4- 1. A schematic of the dual-core As_2Se_3 -PMMA fiber.

As presented in Chapter 3, a dual-core fiber preform is obtained by coating two multimode step-index As_2Se_3 fibers (from Coractive Inc.) with a core diameter of 96 µm, a cladding diameter of 170 µm, and a numerical aperture of NA_{AsSe} = 0.18 [68] using a PMMA layer with an outer diameter of ~ 9.5 mm. The preform is then drawn into a fiber which has an As_2Se_3 core diameter of 12 µm, an As_2Se_3 cladding diameter of 21.25 µm and an outer PMMA cladding diameter of ~ 1.2 mm. Figure 4-1 presents a schematic of the cross-section of a dual-core As_2Se_3-PMMA fiber illustrating two fused As_2Se_3 fibers surrounded by a PMMA layer. The asymmetric geometrical structure of a dual-core fiber with respect to axis-1 and axis-2 leads to strong birefringence with two distinct principal polarization axes [49, 50]. A core diameter of 12 µm is selected to maximize coupling efficiency between the fundamental mode of a step-index As_2Se_3 fiber and fundamental mode of a standard single-mode step-index silica fiber (SMF-28e). A 7 cm long dual-core fiber sample is cut and both ends of are finely polished for low-loss coupling into the fiber. The input and output of core-1 are butt-coupled to standard single-mode silica fibers, and the butt-coupling interfaces are permanently fixed using UV-cured epoxy. The heat-brush method [69-71] is then used to taper the dual-core fiber leading to a diameter of D_{AsSe} = 0.55 μm for each As_2Se_3 micro-wire, a diameter of D_{PMMA} = 31.06 μm for the PMMA cladding, and a 5 cm long waist.

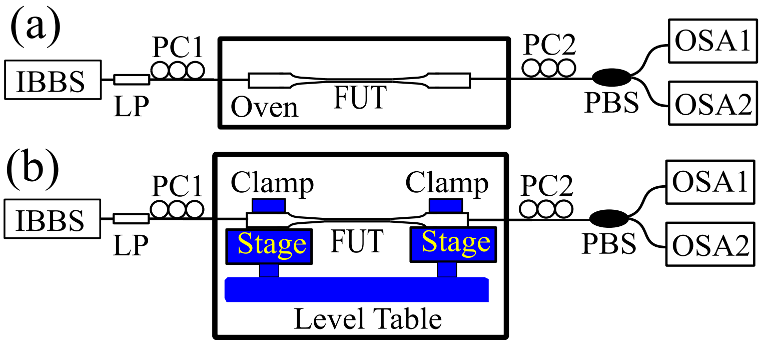

Figure 4- 2. Schematics of the (a) temperature and (b) strain measurement setups. IBBS: incoherent broad-band source; LP: linear polarizer; PC: polarization controller; FUT: fiber under test; PBS: polarization beam-splitter; OSA: optical spectrum analyzer.

Figure 4-2 (a) presents a schematic utilized for the demonstration of temperature measurement in the tapered dual-core As_2Se_3-PMMA fiber. Light from a broadband source (Agilent 83437A) is passed through a linear polarizer (LP) and then launched into core-1 of the dual-core fiber. A polarization controller (PC1) that is utilized to excite both fiber polarizations by aligning the polarization of the broadband light at 45 degrees from the principal polarization axes of the dual-core fiber. A second polarization controller (PC2) at the output of the dual-core fiber is utilized to align the principal polarization axes of the fiber with the principal polarization axes of the polarization beam splitter (PBS) to obtain the transmission spectra of both principal polarization axes of the dual-core fiber. The tapered dual-core fiber is placed in an oven with a resolution of 0.1 ºC. Both the temperature and the transmission spectra of the dual-core fiber are recorded as temperature increases to obtain the evolution of the transmission spectra as a function of temperature.

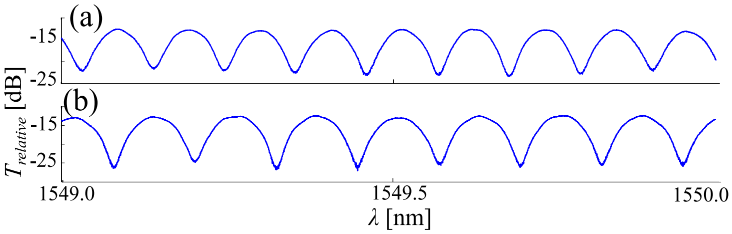

Figure 4- 3. Measured typical interference pattern for a) axis-1 and b) axis-2 of dual-core tapers at room temperature.

Figure 4-3 presents typical measured transmission spectra for both polarization axes of the dual-core fiber. When light is launched into core-1 of the dual-core fiber, half the signal power propagates in the even mode and the other half propagates in the odd mode. The intensity at the output of core-1 is given by $I= 0.5|a_e|^2+0.5|a_o|^2+|a_e||a_o|\cos[\phi_d(\lambda)]$, where $\phi_d(\lambda) = \Delta\beta L_w+\theta_e-\theta_o$. The interference patterns in the transmission spectra arise from the wavelength dependence of $\Delta\beta$, which is defined as the difference between the propagation constants of the two modes.

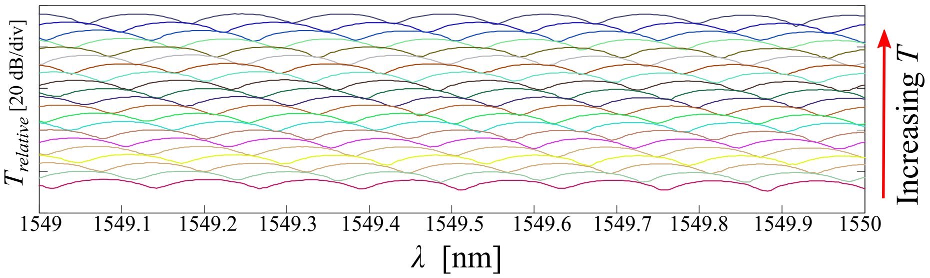

Figure 4- 4. Measured evolution of the transmission spectrum in axis-2 of the tapered dual-core As_2Se_3-PMMA fibers as the temperature increases from 35 ºC to 55 ºC.

Two troughs at the wavelength of 1549.89 nm and 1549.78 nm when temperature is 35 ºC are selected from the transmission spectra of axis-1 and axis-2, respectively. The wavelengths of the two troughs are measured as the temperature of the oven increases from 35 ºC to 55 ºC. Figure 4-4 presents evolution of the transmission spectrum in axis-2 of the tapered dual-core As_2Se_3-PMMA fibers as the temperature increases from 35 ºC to 55 ºC.

The dispersion effect is negligible within the 2 nm span such that all the recorded troughs have the same wavelength shift when temperature changes. One of the troughs at the wavelength of 1549.89 nm from the transmission spectrum is selected to measure the wavelength shifts as the temperature changes. Figure 4-5 (a) presents the wavelength shift of the trough of each principal polarization axis as a function of temperature showing that the troughs shift towards shorter wavelengths as the temperature increases. When temperature increases, $\Delta T > 0$, and since the values of $\partial\phi_d/\partial\lambda$, $L_{w,T}$, $\Delta n_{eff,T}$ and $\alpha_T+\gamma_T$ are all positive, Eq.(2.1) leads to $\Delta\lambda < 0$ in agreement with experimental results. The temperature measurement sensitivity, defined as the rate of wavelength shift with respect to temperature, is -115 pm/ºC for axis-1 and -35.5 pm/ ºC for axis-2.

Figure 4-2 (b) presents a schematic of the strain measurement setup. The tapered dual-core fiber is fixed by two clamps to linear translation stages. Axial strain is induced using the linear translation stages by extending the 5 cm long waist of the tapered dual-core fiber in steps of 10 μm, which corresponds to increasing the axial strain in steps 200 με. The transmission spectrum of the dual-core fiber is measured as the strain is varied from 0 με to 1000 με to obtain the evolution of the transmission spectra as a function of applied strain.

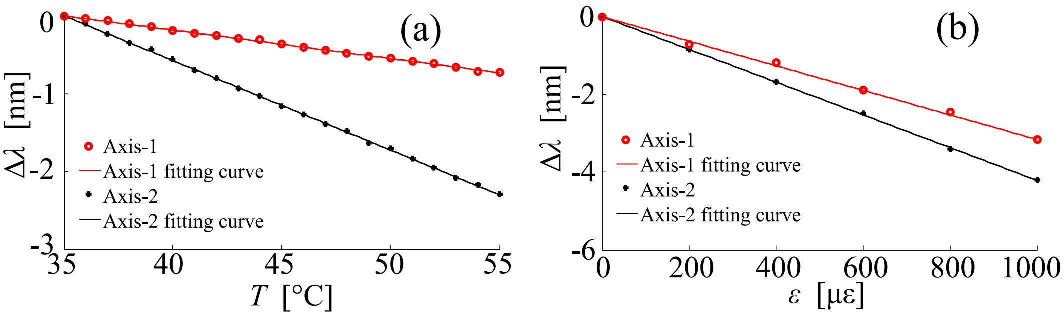

Figure 4- 5. Measured shifts of trough wavelength for axis-1 and axis-2 as a function of (a) temperature and (b) strain.

Similar to the temperature measurement procedure, two troughs are selected from the transmission spectra of axis-1 and axis-2. The wavelengths of the two troughs are measured as the applied strain value is varied from 0 με to 1000 με. Figure 4-5 (b) presents the wavelength shift of the trough of each principal polarization axis as a function of strain showing that the troughs shift towards shorter wavelengths as the strain increases. When strain increases, $\Delta\boldsymbol{\varepsilon} > 0$, and since the values of $\partial\phi_d/\partial\lambda$, $L_{w,\varepsilon}$, $\Delta n_{eff,\varepsilon}$ and $\alpha_{\varepsilon}+\gamma_{\varepsilon}$ are positive, Eq.(2.2) leads to $\Delta\lambda<0$ in agreement with experimental results. The strain measurement sensitivities for axis-1 and axis-2 are -4.21 pm/με and -3.16 pm/με, respectively.

4.1.4 Discussion

The PMMA cladding has a large thermal-expansion coefficient and the As_2Se_3 micron-diameter cores have a low stiffness, leading to a large value of $\alpha_{T,\varepsilon}$. The value of Δn_{eff} is also large due to the large refractive-index difference between the core and cladding materials. According to the expression of $\Delta\lambda_m$ in Eq.(2.1) and Eq.(2.2), the large values of $\alpha_{T,\varepsilon}$ and Δn_{eff} enhance the temperature and strain measurement sensitivities.

There are three physical phenomena affecting the wavelength shift when the temperature of the As_2Se_3-PMMA fiber changes: thermally induced change of the material refractive-indices, core-squeezing induced change of the material refractive-indices, and change of the fiber length. The core-squeezing effect is negligible in fibers that are made from the same material such as silica dual-core fiber, but becomes significant in hybrid As_2Se_3-PMMA fibers that are made from organic and inorganic materials due to one-order-of-magnitude difference between the thermal-expansion coefficients of the organic PMMA cladding (2.02×10^{-4}/°C [25]) and the inorganic As_2Se_3 cores ($\sim0.2\times10^{-4}$/°C [51]). The core-squeezing effect that arises from strain is negligible, and hence, only two physical phenomena induce wavelength shift when the strain that is applied to the As_2Se_3-PMMA fiber changes: strain-induced change of the material refractive-indices, and change of the fiber length. Because the core-squeezing effect in As_2Se_3-PMMA dual-core fibers is significant under temperature variation but negligible under strain variation, it is possible to discriminate between thermal and strain induced wavelength shifts of the transmission spectrum of the dual-core fiber.

The principal polarization axes of the dual-core fiber have different values of Δn_{eff} and $\partial\phi_d/\partial\lambda$, which according to Eqs.(2.1) and (2.2) leads to decorrelated temperature and strain measurement sensitivities for these axes. The thermal-induced core-squeezing further enhances the decorrelation between temperature measurement sensitivities of the principal polarization axes due to the asymmetric structure of the dual-core fiber as the cores are parallel with respect to one axis, but are in series along the other axis. Because of the decorrelated measurement sensitivities of temperature and strain on the principal polarization axes, the tapered dual-core As_2Se_3-PMMA fiber can be used as a dual-parameter sensor to measure both temperature and strain at the same time. The measurement sensitivities on axis-1 and axis-2 are, respectively, -115 pm/ºC and -35.5 pm/ºC for temperature measurement, -4.21 pm/με and -3.16 pm/με for strain measurement. A character matrix $M_{T,\varepsilon}$ is defined to relate the trough wavelength-shift on both principal polarization axes to the changes in temperature and strain leading to

$$\begin{bmatrix} \Delta\lambda_1 \\ \Delta\lambda_2 \end{bmatrix} = M_{T,\varepsilon} \begin{bmatrix} \Delta T \\ \Delta\varepsilon \end{bmatrix} = \begin{bmatrix} -115 & -4.21 \\ -35.5 & -3.16 \end{bmatrix} \begin{bmatrix} \Delta T \\ \Delta\varepsilon \end{bmatrix}.$$

Where $\Delta\lambda_1$, $\Delta\lambda_2$ are the trough wavelength-shift on axis-1 and axis-2, respectively. The character matrix $M_{T,\varepsilon}$ is invertible because temperature and strain measurement sensitivities of the principal polarization axes are decorrelated, and hence, wavelength shifts from both principal polarization axes can be used for simultaneous measurement of temperature and strain variations.

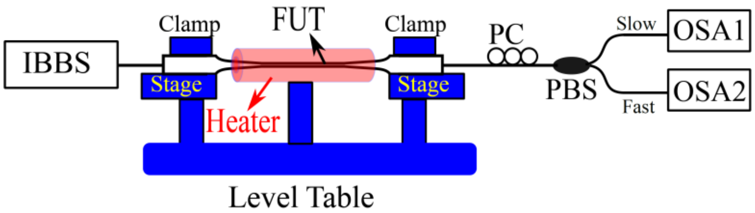

Figure 4- 6. Schematics of the temperature and strain simultaneous measurement setup. IBBS: incoherent broad-band source; LP: linear polarizer; PC: polarization controller; FUT: fiber under test; PBS: polarization beam-splitter; OSA: optical spectrum analyzer.

To test the ability of the proposed sensor, the setup in Fig. 4-6 is utilized to induce temperature and strain simultaneously. The tapered dual-core fiber is fixed by two clamps to linear translation stages inducing the axial strain. An 8 cm long cylindrical shape electrical resistive heater with an inner diameter of 12 mm is utilized to change the temperature around the fiber. The temperature increases from 35 ºC to 55 ºC and the strain randomly changes from 0 to 1000 με. Figure 4-7 shows the comparison between the measured and applied temperature and strain values. The root mean square derivations of the measured temperature and strain errors are 0.15 ºC and 1.87 με, respectively.

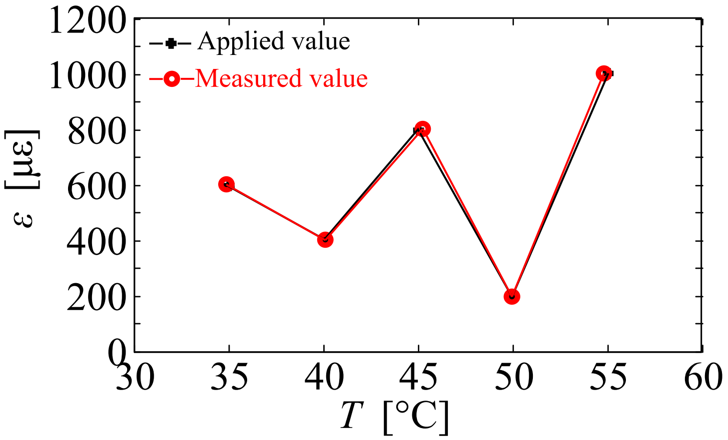

Figure 4- 7. Comparison between simultaneously applied temperature–strain and measured data.

4.1.5 Conclusion

In conclusion, an approach for high-sensitivity measurements of temperature and strain in a dual-core As_2Se_3-PMMA taper is proposed and demonstrated. The large thermal-expansion coefficient of the PMMA cladding, the low stiffness of the micron-diameter As_2Se_3 cores, and the large refractive-index difference between As_2Se_3 and PMMA in a dual-core As_2Se_3-PMMA tapered fibers enable high temperature and strain measurement sensitivities. High temperature and strain measurement sensitivities are observed for the principal polarization axes with values of -115 pm/ºC, -4.21 pm/με for axis-1, -35.5 pm/ºC and -3.16 pm/με axis-2. The thermally-induced core-squeezing effect enables discrimination between temperature and strain. Decorrelation of temperature and strain measurement sensitivities of the principal polarization axes enables simultaneous measurement of temperature and strain variations.

4.2 Novel approach for temperature-insensitive strain measurement

A temperature-insensitive strain sensor is proposed and demonstrated based on a dual-core As_2Se_3-PMMA taper with As_2Se_3 core diameter of 0.61 μm utilizing the thermal forces on As_2Se_3 cores by the PMMA cladding. Longitudinal and transverse forces on the As_2Se_3 cores are induced by thermal expansion/contraction of the PMMA cladding due to an order of magnitude difference between the thermal expansion coefficients of As_2Se_3 and PMMA. At an optimal PMMA layer thickness, the wavelength shift caused by the thermally-induced forces on the refractive-index of the dual-core fiber cores counterbalances that caused by the thermally-induced fiber length variation leading to temperature insensitive transmission. Temperature-insensitive strain measurement over a temperature range from 30 °C to 40 °C is demonstrated in a dual-core As_2Se_3-PMMA fiber with an As_2Se_3 core diameter of 0.61μm and a PMMA cladding diameter of 34.4μm. Thermally-induced forces in hybrid fibers open the path towards the realization of novel sensors and devices that are immune to temperature fluctuations.

4.2.1 Background

Railways, bridges, tunnels, dams, pipelines, and power generators deteriorate due to extreme weather conditions and material aging leading in some instances to catastrophic structural failures such as a bridge collapse. To ensure structural safety and prevent disasters in advance, strain at every point of a civil structure must be constantly monitored. Strain measurement using optical fibers has attracted a lot of attention because optical fibers can be easily embedded in bridges, buildings and other structures. Axial strain measurement has been reported using LPGs [72], FBGs [54, 73], multimode fibers [74], and tapered fiber Mach-Zehnder interferometers [75]. However, most strain fiber sensors are affected by temperature variations leading to unreliable strain measurements. Two main solutions have been utilized for overcoming the problem of temperature dependence: utilization of fibers with dual-parameter sensing capability [60, 61, 64, 65], and utilization of fibers that are insensitive to temperature variation [76-81].

The first solution for overcoming the problem of temperature dependence relies on simultaneous dual-parameter sensing where both temperature and strain are measured simultaneously allowing for reliable strain measurement. For example, simultaneous temperature and strain sensing can be achieved by monitoring shift in the transmission spectra of both polarization axes of a dual-core fiber [82]. In this case, the amplitude of thermally-induced forces is small due to the thin PMMA cladding layer and the thermally-induced length variation plays a significant role in the temperature measurement inducing the negative values of the temperature sensitivities.

The second solution for overcoming the problem of temperature dependence relies on the development of optical fiber devices that are insensitive to temperature. In one approach, engineering the fiber optical properties such as chromatic dispersion can be utilized to achieve temperature insensitivity. For example, temperature insensitivity has been demonstrated in long-period gratings (LPGs) inscribed on a photonic crystal fiber [76, 78]. For this long-period grating, temperature-induced wavelength-shift in the transmission spectrum depends on the fiber dispersion and can be eliminated by engineering the chromatic-dispersion of the photonic crystal fiber. In a second approach, combining two different materials for the core and the cladding has been proposed to achieve temperature insensitive fibers [83]. In this approach, the cladding material and diameter are specially selected such that the overall thermal expansion coefficient of the fiber counterbalances the thermally induced refractive-index change. The hybrid As_2Se_3-PMMA micro-tapers [35], hybrid polymer photonic crystal fiber with integrated chalcogenide glass nanofilms [84] and Zeonex-PMMA microstructured polymer optical fiber sensors [85] have been proposed and demonstrated, to our knowledge, however, this approach has never been experimentally demonstrated because there has not been any material combination that would make the effect of thermally-induced refractive-index variation counterbalance the effect of thermal expansion as proposed in [83], and also because the effect of thermally-induced forces by the fiber cladding on the core has not been considered.

4.2.2 Principle

The dual-core micro-tapers were fabricated using a rod-in-tube method [71, 86]. Figure 4-8 presents an image of the cross-section of a dual-core As_2Se_3-PMMA fiber showing two fused As_2Se_3 fibers and a surrounding PMMA cladding.

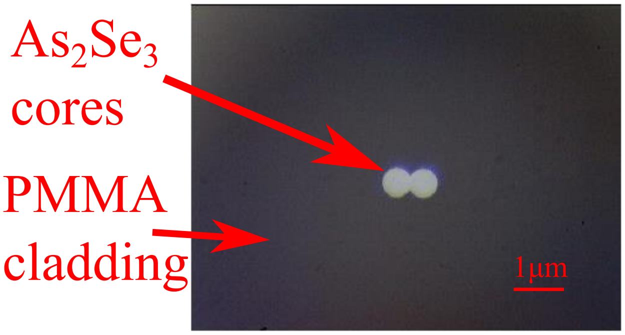

Figure 4- 8. An image of the polished end of the dual-core fiber showing the fused As_2Se_3 fibers and the surrounding PMMA cladding.

As discussed in Chapter 2, the temperature sensors are implemented by the measurement of the wavelength shift of the spectrum caused by the thermally-induced refractive-index change and thermally-induced fiber length variation. The wavelength shift of the transmission spectrum is given by Eq. (2.1)

$$\Delta\lambda_{m,T} = -\left(\partial\phi_d / \partial\lambda\right)^{-1} k_0 L_{w,T} \Delta n_{eff,T} \left(\alpha_T + \gamma_T\right)\Delta T \qquad (2.1)$$

where $\Delta n_{eff,T}$ is the refractive indices difference between the even and odd modes, $L_{w,T}$ is the taper length, $\alpha_T = (1/L_{w,T})(\partial L_{w,T}/\partial T)$, and $\gamma_T = (1/\Delta n_{eff,T})(\partial\Delta n_{eff,T}/\partial T)$. The large difference of thermal expansion coefficients between PMMA cladding with $\alpha_{PMMA} = 2.02\times 10^{-4}$ /°C [25]and the As_2Se_3 cores with $\alpha_{AsSe} \sim 0.2\times10^{-4}$ /°C [51] leads to thermally-induced transverse and longitudinal forces on the As_2Se_3 cores. When temperature increases, the PMMA cladding transversely and longitudinally expands the As_2Se_3 core, and when temperature decreases, the PMMA layer transversely and longitudinally squeezes the As_2Se_3 cores. Taking into account the thermally-induced forces, the variation of $\Delta n_{eff,T}$ with temperature is expressed as

$$\gamma_T = \gamma_{TO} + \gamma_{TIF}$$

where γ_{TO} and γ_{TIF} arise from the variation of $\Delta n_{eff,T}$ by the thermo-optic effect, and thermally-induced forces, respectively. Quantifying γ_{TIF} is difficult since it must be performed numerically and thermally-induced longitudinal and transverse forces are not uniform in the fiber cross section. The value of thermal expansion coefficient of the fiber α is positive, lies between values of the thermal expansion coefficients of As_2Se_3 and PMMA, and depends on the diameter of the As_2Se_3 cores and the thickness of the PMMA cladding. For small As_2Se_3 cores as is the case in tapered dual-core fibers, the value of α is mainly determined by the thickness of the PMMA layer. For a thick PMMA layer, the value of α is the same as the thermal expansion coefficient of PMMA because the stiffness of the thick PMMA layer is higher than that of the As_2Se_3 cores, but for a thin PMMA layer the value of α is the same as the thermal expansion coefficient that of As_2Se_3 because the stiffness of the PMMA layer is lower than that of the As_2Se_3 cores. Furthermore, the value of γ can become negative due to the presence of thermally-induced forces, and at an optimal PMMA layer thickness, the magnitude of γ becomes large enough such that $\alpha + \gamma = 0$ leading to $\Delta\lambda_{m,T} = 0$, which indicates temperature insensitive transmission for the dual-core As_2Se_3-PMMA fiber.

4.2.3 Experimental setup and results

Figure 4-9 presents a schematic of water-bath setup that is utilized for temperature measurement in tapered dual-core As_2Se_3-PMMA fibers. The cooling process of the water bath makes the water temperature decrease steadily avoiding the temperature gradient and fluid currents in the temperature increasing process. Light radiated from an Erbium-doped fiber amplifier (EDFA) is launched into the dual-core fiber through core-1 exciting the even and the odd modes. A polarization controller (PC) is used to adjust the polarization of light coming out from core-1 of the tapered dual-core As_2Se_3-PMMA fiber and align it with the principal polarization axis of the polarization beam splitter (PBS) to obtain the transmission spectrum. The transmission spectrum is observed using an optical spectrum analyzer (OSA). A thermocouple heat sensor (from OMEGA Engineering) with a resolution of 0.1 °C is used for the temperature measurement in the water-bath whose temperature is raised to 50 °C and then is left to cool down. After the setup is stable, the data collection process is started. Both the water temperature and the transmission spectrum are measured and recorded every 10 s as the water cools down from 40 °C to 30 °C to obtain the evolution of the transmission spectrum as a function of temperature.

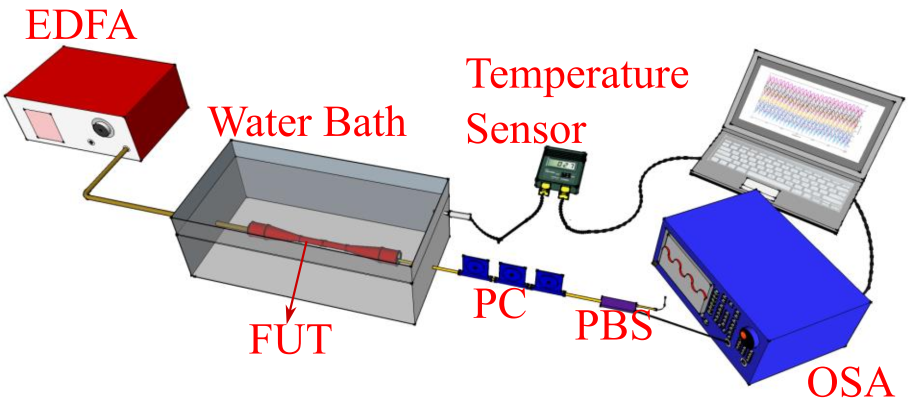

Figure 4- 9. Schematic of the temperature measurement setup. EDFA: Erbium-doped fiber amplifier; FUT: fiber under test; PC: polarization controller; PBS: polarization beam-splitter; OSA: optical spectrum analyzer.

Six tapered dual-core As_2Se_3-PMMA fibers with 5 cm long waists are tested separately in the temperature measurement experiment. The As_2Se_3 core diameters of the six fibers are 1.50 μm, 1.00 μm, 0.65 μm, 0.61 μm, 0.60 μm and 0.55 μm with the PMMA cladding diameters of 84.7 μm, 56.5 μm, 36.7 μm, 34.4 μm, 33.9 μm and 31.1 μm, respectively. One of the troughs from the transmission spectrum is selected to measure the wavelength shifts as the temperature of the water bath drops from 40 °C to 30 °C. Figure 4-10 presents evolution of the transmission spectra of the six tapered dual-core As_2Se_3-PMMA fibers as the temperature drops from 40 °C to 30 °C. The sensitivity, defined as the rate of wavelength shift as a function of temperature, decreases from positive values to negative values as the As_2Se_3 core diameter reduces. As shown in Fig. 4-11(a), the temperature sensitivities are 69.2 pm/°C, 36.9 pm/°C, 9.09 pm/°C , -0.136 pm/°C, -2.38 pm/°C and -36.2 pm/°C, respectively. Figure 4-11(b) presents the measured temperature sensitivity as a function of As_2Se_3 core diameter and PMMA cladding diameter. For the diameter of the As_2Se_3 core such that $D_{AsSe\_core} < D_0$, the thermally-induced length variation dominates the wavelength shift as $\Delta\lambda<0$ and the temperature sensitivity is negative. By contrast, the opposite occurs when $D_{AsSe\_core} > D_0$ where the thermally-induced forces dominate the wavelength shift such that $\Delta\lambda >0$ and the temperature sensitivity is positive.

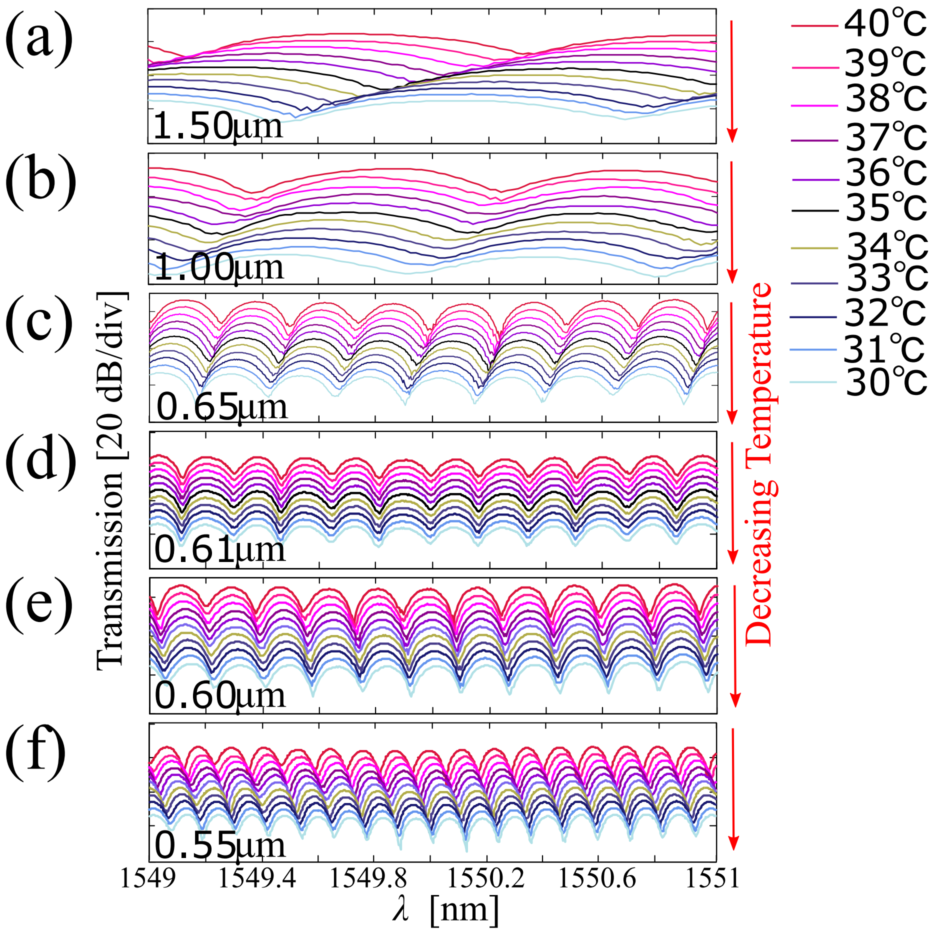

Figure 4- 10. Evolution of the transmission spectra of the six tapered dual-core As_2Se_3-PMMA fibers with As_2Se_3 diameters of (a) 1.50 μm, (b) 1.00 μm, (c) 0.65 μm, (d) 0.61 μm, (e) 0.60 μm and (f)0.55 μm as the temperature decreases ($\Delta T<0$).

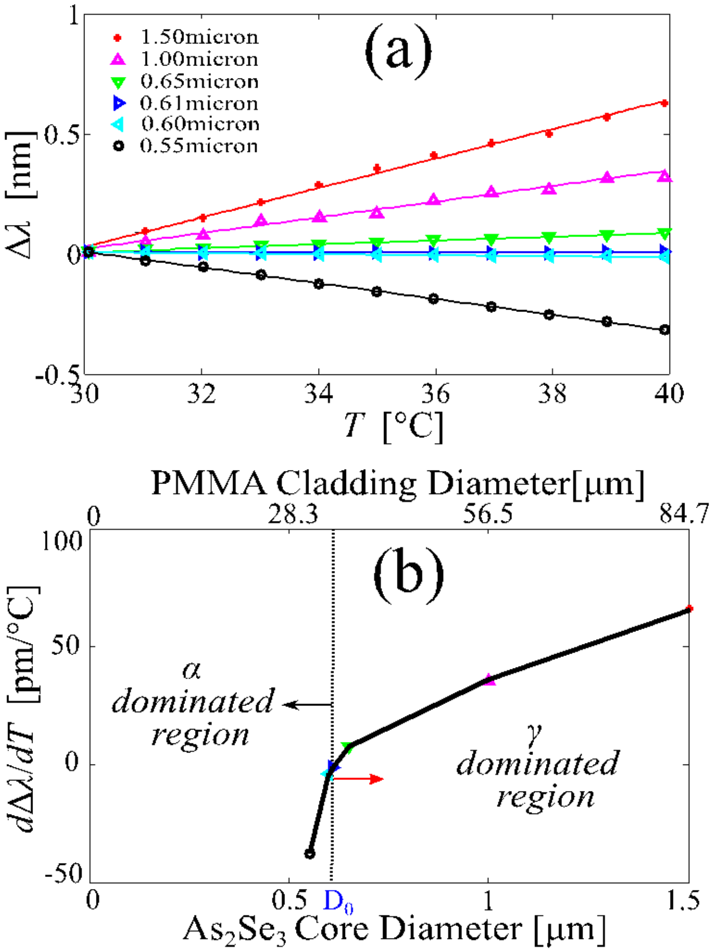

Figure 4- 11. (a) Measured shifts of trough wavelength as a function of temperature for six fibers with As_2Se_3 core diameters of 1.50 μm, 1.00 μm, 0.65 μm, 0.61 μm, 0.60 μm and 0.55 μm. (b) Temperature measurement sensitivity as a function of As_2Se_3 core and PMMA cladding diameter. D_0 stands for the diameter of the As_2Se_3 core at which it has temperature insensitive transmission.

The large difference of thermal expansion coefficient between PMMA cladding and As_2Se_3 cores leads to thermally-induced forces on the As_2Se_3 cores that are determined by the thickness of the PMMA cladding. For a thick PMMA cladding as is the case for tapers with As_2Se_3 core diameters of 1.50 μm, 1.00 μm and 0.65 μm, the thermally-induced forces are large leading to $\alpha + \gamma < 0$, and the trough shifts towards shorter wavelengths when temperature decreases ($\Delta T<0$) as observed in Fig. 4-10(a), (b) and (c). For a thin PMMA cladding as is the case for tapers with an As_2Se_3 core diameter of 0.60 μm and 0.55 μm, the thermally-induced forces are weak leading to $\alpha + \gamma > 0$, and the trough shifts towards longer wavelengths when temperature decreases ($\Delta T<0$) as observed in Fig. 4-10(e) and (f). At an optimal PMMA cladding thickness as is the case for a taper with an As_2Se_3 core diameter of 0.61 μm, the thermally-induced relative variation of the refractive-indice difference between the even and odd modes $\delta\Delta n_{eff,T}/\Delta n_{eff,T}$ counterbalances the thermally-induced relative variation of the fiber length $\delta L_{w,T}/L_{w,T}$ such that $\alpha + \gamma = 0$; consequently, the trough does not shift as the temperature changes leading to a temperature insensitive transmission for the dual-core As_2Se_3-PMMA fiber as observed in Fig. 4-10(d). At the optimal As_2Se_3 core diameter of 0.61 μm, two other fibers with waist lengths of 2 cm and 8 cm are tested also showing low temperature sensitivities of -0.517 pm/°C and -0.262 pm/°C, respectively.

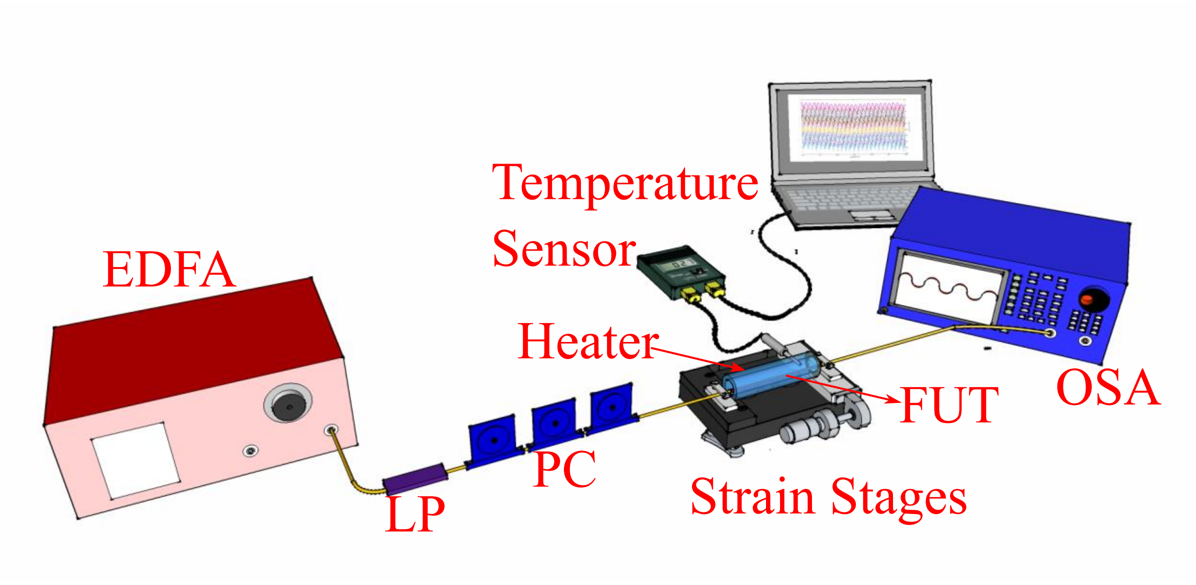

Figure 4- 12. Schematic of the strain measurement setup. EDFA: Erbium-doped fiber amplifier; LP: linear polarizer; PC: polarization controller; FUT: fiber under test; OSA: optical spectrum analyzer.

Figure 4-12 presents a schematic of the strain measurement setup. The light emitted from EDFA is passed through a linear polarizer followed by a polarization controller (PC) that is used for aligning the polarization of the EDFA light with the principal polarization of the dual-core fiber to get the transmission spectrum in the temperature insensitive axis. The tapered dual-core fiber with the As_2Se_3 core diameter of 0.61 μm and PMMA cladding diameter of 34.4 μm is fixed by two clamps to linear translation stages inducing the axial strain by extending the 5 cm long waist in steps of 10 μm, which corresponds increasing the axial strain in steps of 200 με. An 8 cm long cylindrical shape electrical resistive heater with an inner diameter of 12 mm is utilized to change the temperature around the fiber. The transmission spectrum of the dual-core fiber is measured for each applied strain value as the strain is varied from 0 με to 3000 με at 32 °C, 35 °C and 38 °C for both increasing and decreasing strain values to obtain the shift of the transmission spectra as a function of applied strain. Figure 4-13 presents the strain measurement results at 32 °C, 35 °C and 38 °C. The sensitivity is -3.01 pm/με with no hysteresis and does not change at different temperatures.

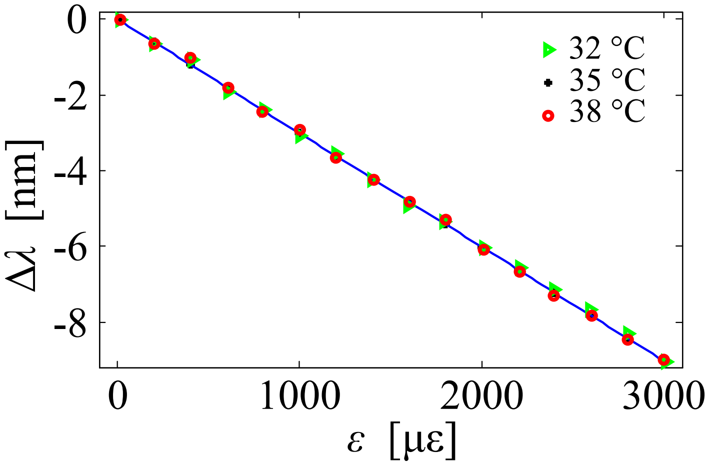

Figure 4- 13. Measured transmission spectrum as a function of strain in a dual-core As_2Se_3-PMMA fiber with a core diameter D_{AsSe_core} =0.61 μm at temperatures of 32 °C, 35 °C and 38 °C.

4.2.4 Discussion

Other fiber parameters such as fiber birefringence, modal-propagation constant, Stimulated Brillouin Scattering gain spectrum, and group-delay can also be made insensitive to temperature by exploiting thermally-induced forces for a variety of applications. Fibers with temperature insensitive fiber birefringence can be utilized for the implementation of filters and polarization rotators with temperature immunity. Temperature-insensitive modal-propagation constant can be utilized in the implementation of lasers with reduced phase noise. A temperature insensitive Stimulated Brillouin Scattering gain spectrum can be utilized for the implementation of lasers with low-frequency drift and reduced frequency hopping. Finally, temperature insensitive group-delay allows for the implementation of pulsating lasers with stable repetition rates. The same approach can be achieved by choosing other materials with a large difference between the expansion coefficients of the core and the cladding.

4.2.5 Conclusion

An approach for a temperature-insensitive strain sensor is proposed and demonstrated by using a dual-core As_2Se_3-PMMA taper. Thermally-induced forces on the As_2Se_3 cores by the PMMA cladding are adjusted by tapering the As_2Se_3-PMMA fiber such that the effect of variations of the difference between effective refractive-indices of the even and odd modes on the fiber transmission spectrum counterbalances the effect of fiber elongation when the temperature changes. The transmission spectrum of the dual-core As_2Se_3-PMMA exhibits a low temperature-sensitivity of -0.136 pm/°C allowing for temperature insensitive strain measurement within 10 °C temperature measurement range. The temperature-insensitivity of optical fiber parameters opens the path for the implementation of reliable sensors and devices with immunity to temperature fluctuations.

4.3 Sensitivity enhancement for temperature and strain measurement

We demonstrate an approach for high-sensitivity temperature and strain measurement in a dual-core As_2Se_3-PMMA taper with As_2Se_3 core diameter of 2.5 μm. To improve the sensitivity of temperature and strain measurement, we designed the dual-core As_2Se_3-PMMA fiber with inorganic As_2Se_3 cores and organic PMMA cladding and also the even and odd modes to build an interferometer. The variation of the difference between phases of the two modes with respect to wavelength ($\partial\phi_d(\lambda)/\partial\lambda$) decreases with increasing As_2Se_3 core diameter, and consequently, thermally-induced and strain-induced change of the difference between phases of the two modes $\phi_d(\lambda)$ leads to a large wavelength shift indicating enhancement of the temperature and strain measurement sensitivity. Furthermore, thermally-induced longitudinal and transverse forces on the As_2Se_3 cores further enhance the temperature measurement sensitivity. High sensitivities of 436 pm/°C, -6.23 pm/μ**ε** and 572 pm/°C and -3.63 pm/μ**ε** from the transmission spectra of axis-1 and axis-2 in the dual-core As_2Se_3-PMMA taper are obtained.

4.3.1 Background

Fiber optical temperature and strain sensors have been extensively investigated for applications in the civil structures to ensure safety and prevent disasters in advance [57, 87]. Various techniques have been proposed to simultaneously monitor temperature and strain variations [29, 87]. Most of the demonstrated fiber sensors are based on the silica fibers by measuring the spectrum wavelength shift caused by the change of the refractive index and fiber length. Silica fibers have the thermal-expansion coefficient of $\sim 0.5\times10^{-6}/^{\circ}C$ [21], while the values of thermal-expansion coefficients of As_2Se_3 and PMMA are $\sim 0.2\times10^{-4}/^{\circ}C$ [51]

and 2.02×10^{-4}/˚C [25, 88], respectively. To improve the sensitivity we designed the dual-core As_2Se_3-PMMA fiber with the PMMA cladding diameter 56.5 times larger than that of the As_2Se_3 cores.

Simultaneous temperature and strain measurement with temperature sensitivities of -115 pm/˚C for axis-1, -35.5 pm/˚C for axis-2 and strain sensitivities of -4.21 pm/μ**ε** for axis-1 and -3.16 pm/μ**ε** for axis-2 has been reported in a dual-core As_2Se_3-PMMA fiber with As_2Se_3 core diameter of 0.55 μm [82]. In this case, thermally-induced forces are small due to the thin PMMA cladding layer. A temperature-insensitive strain sensor based on thermally-induced forces in dual-core As_2Se_3-PMMA taper has been demonstrated [89]. At an optimal PMMA layer thickness of 34.4 μm with As_2Se_3 core diameter of 0.61 μm, the wavelength shift caused by the thermal forces counterbalances that caused by the thermally-induced fiber length variation leading to temperature insensitive transmission.

We propose and demonstrate high-sensitivity temperature and strain measurement in a dual-core As_2Se_3-PMMA taper with a large As_2Se_3 core diameter. The variation of the difference between phases of the two modes with respect to wavelength ($\partial\phi_d(\lambda)/\partial\lambda$) becomes small as the As_2Se_3 core diameter increases, and consequently, the difference between phases of the two modes ϕ_d (λ) induced by variations of temperature and strain leads to a large wavelength shift indicating enhancement of the temperature and strain measurement sensitivity in dual-core fibers with large As_2Se_3 core diameter. Moreover, the increased thermal forces in the fibers with large PMMA cladding will further increase the temperature measurement. High measurement sensitivities are observed in both principal polarization axes of the dual-core As_2Se_3-PMMA taper with the As_2Se_3 core diameter of 2.5 μm and PMMA cladding diameter of 113 μm. The measured temperature and strain sensitivities are 436 pm/˚C for axis-1, 572 pm/˚C for axis-2 and -6.23 pm/μ**ε** for axis-1 and -3.63 pm/μ**ε** for axis-2, respectively.

4.3.2 Principle

As discussed in Chapter 2, the fiber length and the effective refractive index of the even and odd modes are changed thermally leading to the wavelength-shift of the troughs that is given by Eq. (2.1)

$$\Delta\lambda_{m,T} = -\left(\frac{\partial\phi_d}{\partial\lambda}\right)^{-1}\frac{2\pi}{\lambda}L_{w,T}\Delta n_{eff,T}\left(\alpha_T+\gamma_{TO}+\gamma_{TIF}\right)\Delta T \quad (2.1)$$

where $\Delta n_{eff,T}$ is the refractive index difference between the even and odd modes, $L_{w,T}$ is the taper length, $\alpha_T = (1/L_{w,T})\partial L_{w,T}/\partial T$, $\gamma_T = (1/\Delta n_{eff,T})\,\partial\Delta n_{eff,T}/\partial T$ and $\gamma_T = \gamma_{TO} + \gamma_{TIF}$ with γ_{TO} and γ_{TIF} being the variation of $\Delta n_{eff,T}$ by the thermo-optic effect, and thermally-induced forces, respectively.

When strain varies, the fiber length and the effective index of the even and odd modes are changed leading to the wavelength-shift of the troughs that is given by Eq. (2.2)

$$\Delta\lambda_{m,\varepsilon} = -\left(\frac{\partial\phi_d}{\partial\lambda}\right)^{-1}\frac{2\pi}{\lambda}L_{w,\varepsilon}\Delta n_{eff,\varepsilon}\left(\alpha_\varepsilon+\gamma_\varepsilon\right)\Delta\varepsilon \qquad (2.2)$$

where $\Delta n_{eff,\boldsymbol{\varepsilon}}$ is the refractive indices difference between the even and odd modes, $L_{w,\boldsymbol{\varepsilon}}$ is the taper length, $\alpha_{\boldsymbol{\varepsilon}} = (1/L_{w,\boldsymbol{\varepsilon}})\,\partial L_{w,\boldsymbol{\varepsilon}}/\partial\boldsymbol{\varepsilon}$, $\gamma_{\boldsymbol{\varepsilon}} = (1/\Delta n_{eff,\boldsymbol{\varepsilon}})\,\partial\Delta n_{eff,\boldsymbol{\varepsilon}}/\partial\boldsymbol{\varepsilon}$ with $\gamma_{\boldsymbol{\varepsilon}}$ being the variation of $\Delta n_{eff,\boldsymbol{\varepsilon}}$ induced by the strain. The low stiffness of the micron diameter of As_2Se_3-PMMA fiber and the large refractive-indice difference between the even and odd modes enable the high-sensitivity strain measurement in the dual-core As_2Se_3-PMMA taper.

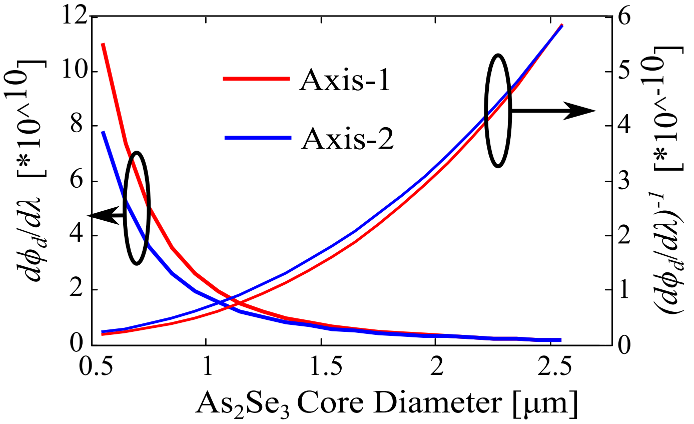

Figure 4- 14. Calculated values of $\partial \phi_d / \partial \lambda$ and $(\partial \phi_d / \partial \lambda)^{-1}$ as a function of As_2Se_3 core diameter.

Figure 4-14 shows calculated values of $\partial\phi_d/\partial\lambda$ and $(\partial\phi_d/\partial\lambda)^{-1}$ as a function of diameter of As_2Se_3 core using Comsol Multiphysics software. The value of $\partial\phi_d/\partial\lambda$ decreases as the diameter of the As_2Se_3 cores. According to Eq. (1) and (2), a small value of $\partial\phi_d/\partial\lambda$ induces a large wavelength shift of the transmission spectrum of the dual-core fiber when temperature and strain changes. Although the value of the $\Delta n_{eff,T}$ slightly decreases, the overall product of $(\partial\phi_d/\partial\lambda)^{-1}$ and $\Delta n_{eff,T}$ increases as the As_2Se_3 core diameter increases, which enhances the temperature and strain measurement sensitivity.

For temperature measurement, the positive value of the thermal-expansion coefficient α_T depends on the diameter of the As_2Se_3 cores and the thickness of the PMMA cladding. For dual-core fibers with small As_2Se_3 cores and a thick PMMA layer, the value of α_T is the same as the thermal-expansion coefficient of PMMA due to the higher value of the stiffness of the thick PMMA layer. The positive value of γ_{TO} is determined by the thermal-optic coefficients of the As_2Se_3 cores and the PMMA layer which are ~ 2.0×10^{-4}/°C [51, 90] and -1.20×10^{-4}/°C [25, 88, 91], respectively. The negative value of γ_{TIF} is determined by the negative value of the stress-optic coefficient [92] of chalcogenide glass due to the strain by the thermal-forces of the PMMA cladding on the As_2Se_3 cores. When temperature varies, the

PMMA cladding transversely and longitudinally expands or squeezes the As_2Se_3 cores leading to the variation of the refractive index of As_2Se_3 cores and the negative value of γ_{TIF}. However, quantifying γ_{TIF} is difficult since it must be performed numerically and thermally-induced longitudinal and transverse forces are not uniform in the fiber cross-section. Thermally-induced longitudinal and transverse forces are further induced as the diameter of the thickness of the PMMA layer increases. The negative value of γ_{TIF} becomes smaller inducing $\alpha_T+\gamma_T=\alpha_T+\gamma_{TO}+\gamma_{TIF} << 0$, which will further enhance the temperature measurement sensitivity.

4.3.3 Experimental results

The dual-core fiber is tapered using the heat-brush method [34, 69-71] to obtain micro-wires. In the heat-brush method, the dual-core fiber is heated to a softening temperature and then pulled symmetrically from both ends to elongate the fiber as the heater sweeps back and forth within a designated hot-zone [70]. A continuous-wave laser with power P_{in} at λ= 1550 nm is launched into core-1 of the dual-core fiber and a power-meter measures the power P_{out} at the output of core-1 as the dual-core fiber is being extended from both ends. Figure 4-15 presents the measured transmission $T = P_{out}/P_{in}$ of core-1 in the dual-core fiber with the targeted As_2Se_3 core diameter $D_{AsSe} = 2$ μm and targeted fiber length L = 10 cm as a function of extension.

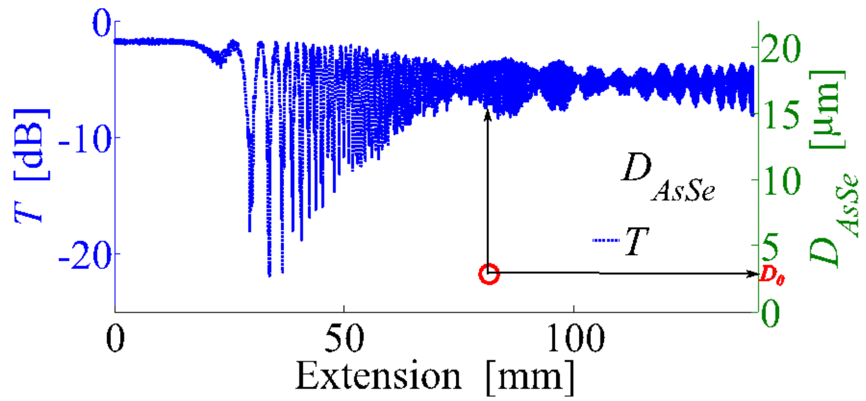

Figure 4- 15. Measured transmission of core-1 in the dual-core fiber as a function of extension during the tapering process.

In Fig. 4-15, the transmission as a function of extension exhibits an amplitude modulation due to the polarization dependence of the tapered dual-core As_2Se_3-PMMA fiber. When the extension length is about 80 mm corresponding to the As_2Se_3 core diameter $D_{AsSe} = D_0 = 3.0$ μm, the polarization property starts to appear showing two principal axes that enables the dual-parameter sensing. Figure 4-16 presents measured transmission spectra for axis-1 and axis-2 of the dual-core fiber with $D_{AsSe} = 2.5$ μm. The interference patterns in the transmission spectra of the two axes show different periodic oscillations.

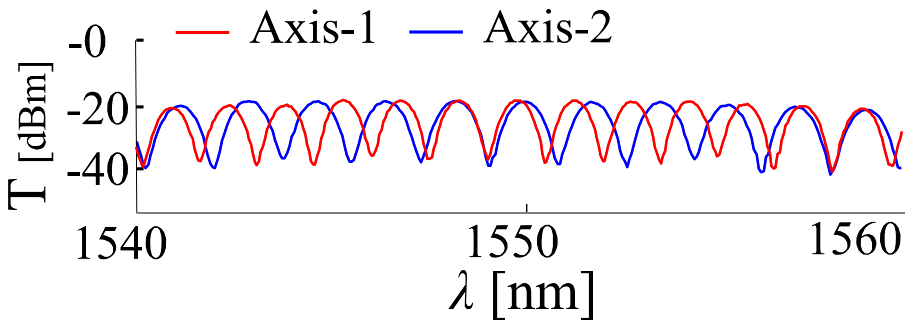

Figure 4- 16. Measured typical interference pattern for axis-1 and axis-2 of dual-core taper with D_{AsSe} = 2.5 μm and L = 10 cm waist. T stands for the transmission power of the fiber.

A water-bath setup is utilized for the demonstration of temperature measurement in the tapered dual-core As_2Se_3-PMMA fiber shown in [82]. The tapered dual-core fibers are completely immersed in the water-bath whose temperature is raised to 60 ˚C and then is left to cool down. A thermocouple (OMEGA Engineering) is used to measure the water temperature at a resolution of 0.1 ˚C. Both the water temperature and the transmission spectra of the dual-core fiber are measured every 30 s as the water cools down from 55 ˚C to 30 ˚C to obtain the evolution of the transmission spectra in axis-1 and axis-2 as a function of temperature. Four tapered dual-core As_2Se_3-PMMA fibers with 10 cm long waists are tested separately in the temperature measurement experiment. The As_2Se_3 core diameters of the four fibers are 2.5 µm, 2.0 µm, 1.5 µm and 1.0 µm with the PMMA cladding diameters of 141.3 µm, 113.0 µm, 84.8 µm and 56.5 µm, respectively. The transmission spectra in both axes of each fiber are measured as the temperature of the water bath drops from 55 ˚C to 30 ˚C. As shown in Fig. 4-17(a), in axis-1 the temperature sensitivities, defined as the rate of wavelength shift of troughs as a function of temperature, are 410 pm/˚C, 253 pm/˚C, 94.8 pm/˚C and 45.2 pm/˚C, respectively. Figure 4-17(b) presents the temperature sensitivities in axis-2 that are 560 pm/˚C, 363 pm/˚C, 238 pm/˚C and 115 pm/˚C, respectively. For comparison, the measured shifts of trough wavelength for the fiber with As_2Se_3 core diameter of 0.55 µm [82] are also added in the Fig. 4-17 with temperature sensitivities of -115 pm/˚C for axis-1, -35.5 pm/˚C for axis-2. The large difference of thermal expansion coefficient between PMMA cladding and As_2Se_3 cores leads to thermally-induced forces on the As_2Se_3 cores that are determined by the thickness of the PMMA cladding. For a thick PMMA cladding as is the case for tapers with As_2Se_3 core diameters of 2.5 µm, 2.0 µm, 1.5 µm and 1.0 µm, the thermally-induced forces are large leading to $\alpha_T + \gamma_{TO} + \gamma_{TIF} < 0$, and the trough shifts towards longer wavelengths when temperature increases. For a thin PMMA cladding as is the case for the taper with an As_2Se_3 core diameter of 0.55 µm, the thermally-induced forces are weak leading to $\alpha_T + \gamma_{TO} + \gamma_{TIF} > 0$, and the trough shifts towards shorter wavelength when the temperature increases. The fiber with largest As_2Se_3 core diameter has strongest thermally-induced forces and also the smallest value of $\partial\phi_d/\partial\lambda$ inducing largest wavelength shift in the transmission spectrum and highest temperature measurement sensitivity, as is the case for the fiber with As_2Se_3 core diameter of 2.5 µm. Figure 4-17(c) presents the measured temperature sensitivity as a function of As_2Se_3 core diameter for axis-1 and axis-2, which shows enhanced sensitivity as the As_2Se_3 core diameter increases. Although the trend of the sensitivity with respect to the core diameter is modulated by Δn_{eff} and γ_T based on Eq. (1), it is consistence with that of $(\partial\phi_d/\partial\lambda)^{-1}$ as shown in Fig. 4-14.

In order to obtain the evolution of the transmission spectra as a function of applied strain, the tapered dual-core fiber with D_{AsSe} = 2.5 µm is fixed by two clamps to linear translation stages inducing the axial strain by extending the 10 cm long waist in steps of 10 µm, which corresponds increasing the axial strain in steps of 100 $\mu\boldsymbol{\varepsilon}$. The transmission spectra of the two axes are recorded as the strain is varied from 0 to 1000 $\mu\boldsymbol{\varepsilon}$. Figure 4-18 presents the measured wavelength shifts of axis-1 and axis-2 as a function of strain showing that strain measurement sensitivities are -6.23 pm/$\mu\boldsymbol{\varepsilon}$ and -3.63 pm/$\mu\boldsymbol{\varepsilon}$, respectively. Since all the values of $\partial\phi_d/\partial\lambda$, $L_{w,}$, $\Delta n_{eff,\boldsymbol{\varepsilon}}$ and $(\alpha_{\boldsymbol{\varepsilon}} + \gamma_{\boldsymbol{\varepsilon}})$ are positive when the strain increases, Eq. (2.2) leads to $\Delta\lambda < 0$ in agreement with experimental results.

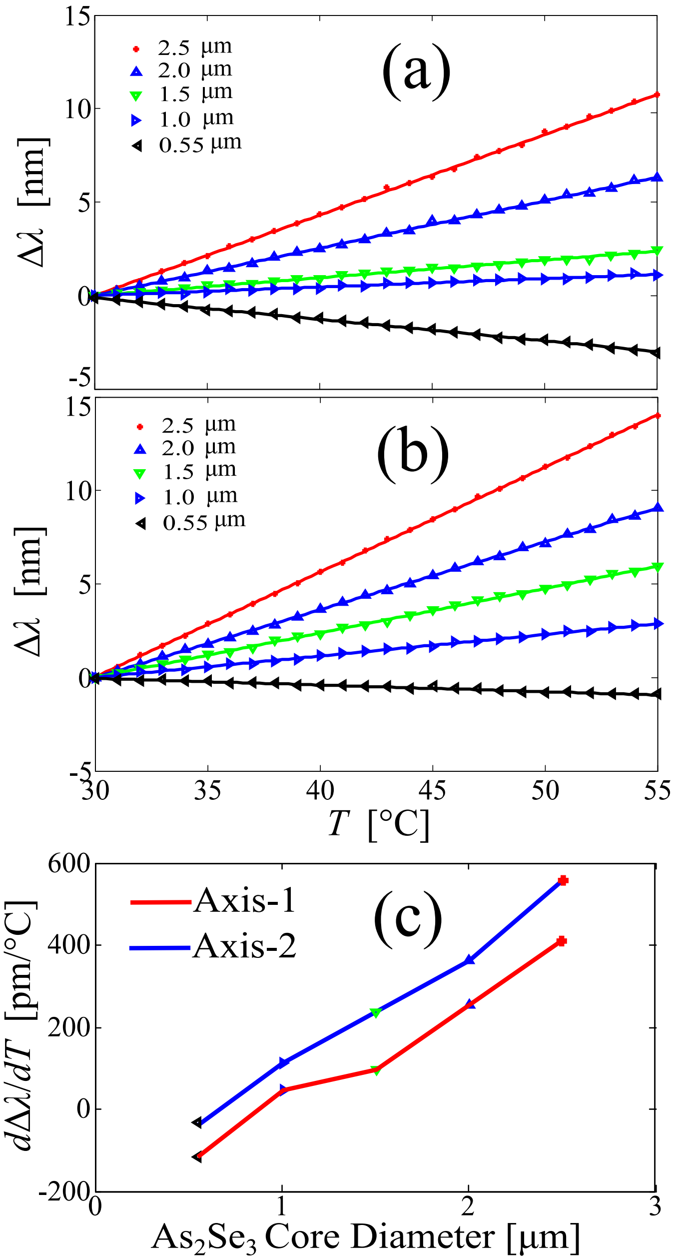

Figure 4- 17. Measured shifts of trough wavelength for 4 fibers with As_2Se_3 core diameters of 2.5 μm, 2.0 μm, 1.5 μm, 1.0 μm and 0.55 μm [8] as a function of temperature for (a) axis-1 (b) axis-2. The straight lines present the linear fitting of the measured data. (c)Temperature measurement sensitivity as a function of As_2Se_3 core diameter for axis-1 and axis-2.

A character matrix $M_{T,}$ is defined to relate the wavelength-shift of transmission spectra in axis-1 and axis-2 to the variations in temperature and strain:

$$\begin{bmatrix}\Delta\lambda_1\\ \Delta\lambda_2\end{bmatrix} = M_{T,\varepsilon}\begin{bmatrix}\Delta T\\ \Delta\varepsilon\end{bmatrix} = \begin{bmatrix}436 & -6.23\\ 572 & -3.63\end{bmatrix}\begin{bmatrix}\Delta T\\ \Delta\varepsilon\end{bmatrix}$$

where $\Delta\lambda_1$, $\Delta\lambda_2$ are the wavelength-shifts of the transmission spectrum in axis-1 and axis-2, respectively. The character matrix M_T can be used to simultaneously determine the temperature and strain variations from the wavelength shifts of transmission spectra in axis-1 and axis-2.

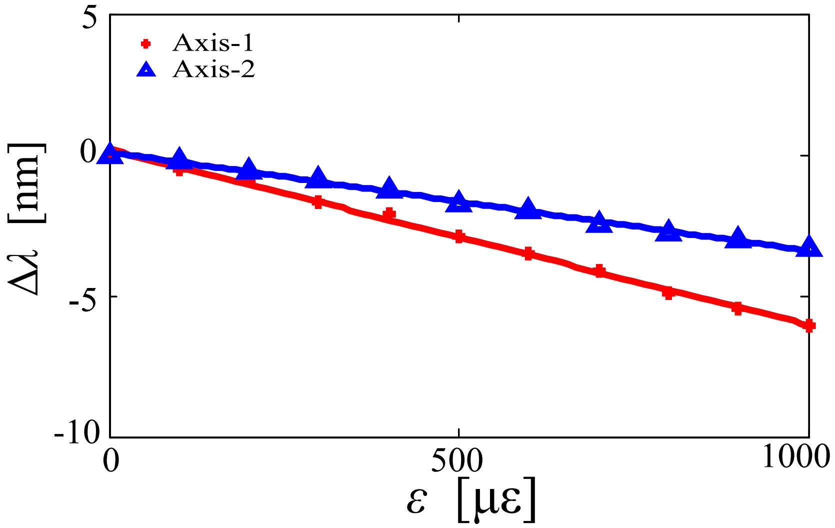

Figure 4- 18. Measured shifts of trough wavelength for the fiber with As_2Se_3 core diameters of 2.5 μm as a function of strain for axis-1 and axis-2. The straight lines present the linear fitting of the measured data.

4.3.4 Conclusion

An approach for high-sensitivity temperature and strain sensor is proposed and demonstrated by using a dual-core As_2Se_3-PMMA taper with the As_2Se_3 core diameter of 2.5 μm. Theoretical model and experimental results show that the sensitivities of temperature and strain measurement are enhanced when the value of $\partial\phi_d(\lambda)/\partial\lambda$ becomes small. Thermally-induced forces on the As_2Se_3 cores by the PMMA cladding further enhance the temperature measurement sensitivity. The transmission spectrum of the dual-core As_2Se_3-

PMMA exhibits high measurement sensitivities on axis-1 and axis-2 of 436 pm/˚C and 572 pm/˚C for temperature measurement, -6.23 pm/μ**ε** and -3.63 pm/μ**ε** for strain measurement.

Chapter 5 Self-inscribed antisymmetric long-period grating in a dual-core As_2Se_3-PMMA fiber and its sensing application

In this chapter, we report for the first time that transmission of optical pulses centered at a wavelength of 1550 nm through a tapered dual-core As_2Se_3-PMMA fiber inscribes an antisymmetric long-period grating. Then we propose and demonstrate an approach for temperature-sensitivity enhancement by a factor of 4.0 based on effective group-velocity matching between the even and odd modes of a dual-core As_2Se_3-PMMA taper on which an antisymmetric long-period grating is inscribed.

5.1 Self-inscribed antisymmetric long-period grating

We report for the first time that transmission of optical pulses centered at a wavelength of 1550 nm through a tapered dual-core As_2Se_3-PMMA fiber inscribes an antisymmetric long-period grating. The pulse power is equally divided between even and odd modes that superpose along the dual-core fiber to form an antisymmetric intensity distribution. A permanent refractive-index change that matches the antisymmetric intensity distribution is inscribed due to photosensitivity at the pulse central wavelength. The evolution of the transmission spectrum of the dual-core fiber is experimentally measured as the accumulated time that the fiber is exposed to the pulse is increased. A theoretical model of an antisymmetric long-period grating in a dual-core fiber computationally reproduces the experimentally observed evolution of the transmission spectrum. Experimental results indicate that antisymmetric long-period gratings induce effective group-velocity matching between the even and odd modes of the dual-core fiber, and reveal for the first time that long-period gratings can lead to slow light propagation velocities.

5.1. 1 Background

Tapered chalcogenide-polymer fiber structures composed of an As_2Se_3 core and a polymethyl methacrylate (PMMA) cladding are a promising platform for nonlinear applications because the As_2Se_3 core provides high nonlinearity over the near- and mid-infrared spectral ranges for compact nonlinear devices with low power consumption and the PMMA cladding provides high mechanical robustness for easy handling. Indeed, tapered As_2Se_3-PMMA fibers have been used in a variety of practical applications including super-continuum generation [35], broadband parametric amplification [38], polarization switching [93], and laser pulse generation [40]. Advanced As_2Se_3-PMMA fiber structures such as dual-core and birefringent elliptical-core fibers enable novel all-optical signal processing devices for a broader set of applications. Dual-core As_2Se_3-PMMA fiber tapers composed of two As_2Se_3 cores and a PMMA cladding are especially promising because they support guided propagation of two main modes, an even mode and an odd mode, allowing for advanced nonlinear applications such as modulation instability in both the normal and anomalous dispersion regimes [94], pulse self-switching [95], and phase-matched four-wave mixing [96].

Photosensitivity of As_2Se_3 glass to optical signals at a wavelength of 1550 nm has been demonstrated and utilized for the inscription of fiber Bragg gratings in tapered single-core As_2Se_3-PMMA fibers [39]. Two identical optical pulses propagating in opposite directions in the tapered As_2Se_3-PMMA fiber form a standing wave which inscribes a longitudinal periodic refractive-index variation leading to the formation of a fiber Bragg grating. The resonance wavelength of the resulting fiber Bragg-grating coincides with the central wavelength of the pulse that is used for grating inscription, which allows for changing the resonance wavelength by tuning the pulse central wavelength. Furthermore, these gratings are inscribed over the entire As_2Se_3-PMMA taper waist allowing for the inscription of long fiber Bragg gratings.

In this section, we report for the first time that the propagation of optical pulses in a dual-core As_2Se_3-PMMA fiber inscribes an antisymmetric long-period grating with resonance at the central wavelength of the propagating pulses. Experimentally measured transmission spectra of the dual-core As_2Se_3-PMMA fiber show that propagation of optical pulses centered at a wavelength of 1550 nm causes the formation of an antisymmetric long-period grating due to photosensitivity of As_2Se_3. A theoretical model is then developed to computationally reproduce experimental measurements confirming the formation of an antisymmetric long-period grating in the dual-core fiber. The experimentally measured transmission spectra are analyzed to deduce the effect of the antisymmetric long-period grating on the difference between the phases of the even and odd modes of the dual-core fiber. The deduced phase-difference graph indicates that the antisymmetric long-period grating induces effective group-velocity matching between the even and odd modes, and can potentially lead to slow light propagation velocities.

5.1.2 Experiment and results

Two multimode step-index As_2Se_3 fibers (from Coractive Inc.) with a core diameter of D_{core_AsSe} = 96 μm, a cladding diameter of $D_{cladding\_AsSe}$ = 170 μm, and a numerical aperture of NA_{AsSe} = 0.18 are coated by a PMMA layer with an outer diameter of ~ 9.5 mm to obtain a dual-core fiber preform. The preform is then drawn into a fiber with an As_2Se_3 core diameter of 12 μm, an As_2Se_3 cladding diameter of 21.25 μm and an outer PMMA cladding diameter of ~1.2 mm. A fiber section with a length of 7 cm is cut, both ends are polished, the input and the output of core 1 are butt-coupled to standard single-mode silica fibers, and UV-cured epoxy permanently fixes the butt-coupling interfaces between the dual-core fiber and the silica fibers. The dual-core fiber is then tapered using the heat-brush method [69-71] to obtain a micro-wire with a 1.5 μm diameter for each As_2Se_3 core, an 84.7 μm diameter PMMA cladding, and a 10 cm long waist.

Figure 5-1(a) presents the setup used for the inscription and characterization of an antisymmetric long-period grating in the tapered dual-core As_2Se_3-PMMA fiber. Optical pulses with a width of 12 ps centered at a wavelength of λ_c = 1550.3 nm are generated using a laser source (Pritel FFL-1550-20). An electro-optic intensity modulator (Photline MXER-LN-10) that is driven with an electrical square pulse with a duration of 100 μs and repetition rate of 1 MHz reduces the average power of the optical pulses by 10 dB to avoid melting the tapered dual-core fiber. The optical pulses pass through a linear polarizer into core-1 of the tapered dual-core fiber to inscribe a permanent refractive-index change by photosensitivity at λ_c. Broadband amplified spontaneous emission noise from an Erbium-doped fiber amplifier (EDFA) is also passed through the linear polarizer to obtain polarized broadband light. The polarized broadband light is launched into core-1 of the dual-core fiber and the output light from core-1 is passed to an optical spectrum analyzer to obtain the transmission spectrum of the tapered fiber. A polarization controller aligns the polarized broadband light and the optical pulses with one principal polarization axis of the tapered dual-core fiber.

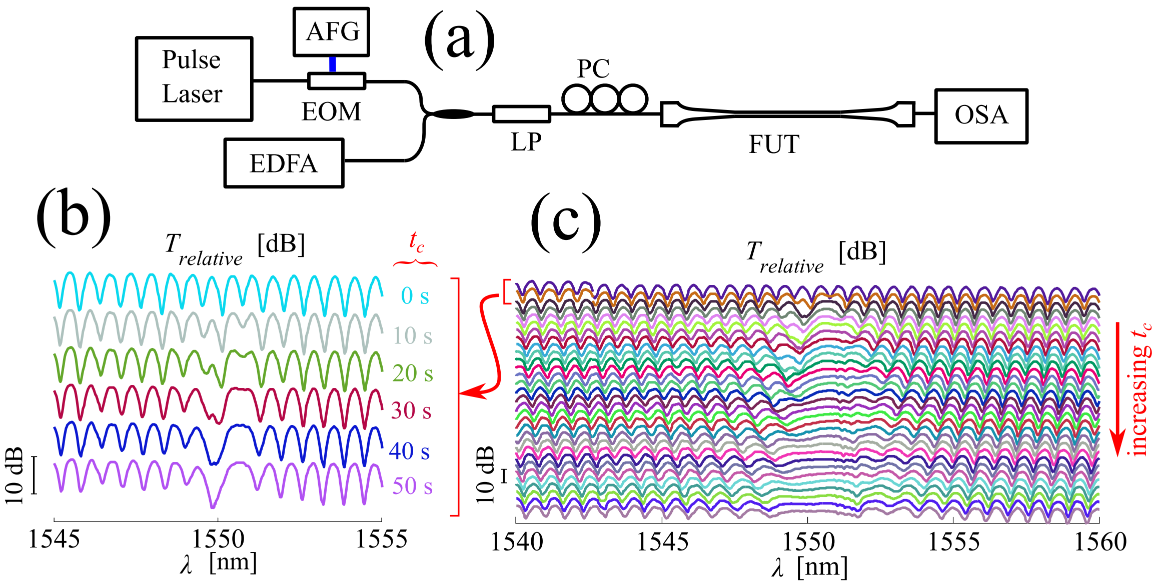

Figure 5- 1. a) Schematic of the setup for inscription and characterization of an antisymmetric grating in a tapered dual-core As_2Se_3-PMMA fiber. b) Initial growth of the transmission spectrum as the cumulative exposure time is increased from 0 s to 50 s in steps of 10 s. c) Evolution of the transmission spectrum as the cumulative exposure time is increased from 10 s to 610 s in steps of 20 s. EDFA: Erbium-doped fiber amplifier, LP: linear polarizer, PC: polarization controller, OSA: optical spectrum analyzer, FUT: fiber under test, AFG: arbitrary function generator, EOM: electro-optic modulator.

The EDFA is switched OFF and the pulsed laser is switched ON to induce refractive-index change by photosensitivity in the tapered dual-core fiber. After 10 seconds, the pulsed laser is switched OFF, the EDFA is switched ON, and the transmission spectrum of the tapered dual-core fiber is measured using the optical spectrum analyzer. The procedure of pulse exposure and transmission measurement is repeated for exposure durations of 10 s to obtain the transmission spectra of the tapered dual-core fiber as the cumulative exposure duration increases. Figure 5-1(b) presents the measured transmission spectra as the cumulative exposure duration is increased from 0 s to 50 s in steps of 10 s. To get further insight into the changes induced on the tapered dual-core fiber, Fig. 5-1(c) presents the measured transmission spectra as the cumulative exposure duration is increased from 10 s to 610 s in steps of 20 s.

5.1.3 Discussion

The changes in the transmission spectrum observed in Figs. 5-1(b) and 5-1(c) occur due to the formation of an antisymmetric long-period grating in the tapered dual-core fiber. When an optical pulse is launched into core 1 of the dual-core fiber, the pulse power is split equally between the even and odd modes. These two modes superpose along the tapered dual-core fiber to form an antisymmetric periodic spatial power distribution as illustrated in Fig. 5-2. The intensity is proportional to $\cos^2[\pi z/\Lambda]$ in core 1 and $\sin^2[\pi z/\Lambda]$ in core 2 where Λ is the spatial period of intensity oscillations given by $\Lambda=2\pi/(\beta_e-\beta_o)$, β_e, β_o are the propagation constants of the even, odd modes, respectively, and z is the propagation distance. A refractive-index change is inscribed by the optical pulse in the fiber cores due to photosensitivity of As_2Se_3 at the pulse central wavelength, λ_c [39]. The inscribed refractive-index change is proportional to the pulse power, and hence, the antisymmetric spatial power distribution leads to an antisymmetric grating with a period Λ in the tapered dual-core fiber.

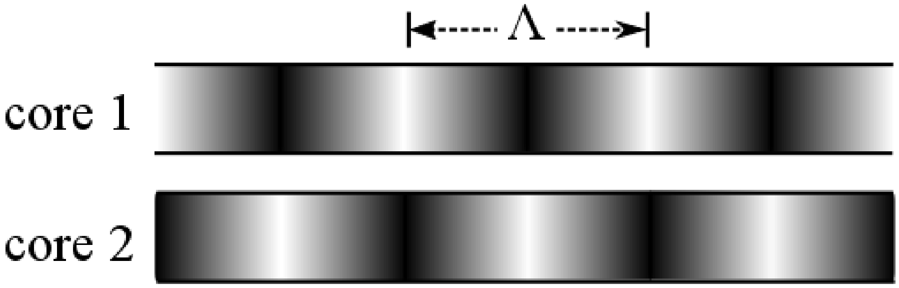

Figure 5- 2. Illustration of spatial power distribution in a dual-core fiber when light is launched into core 1.

Calculation of the transmission spectrum confirms that an antisymmetric long-period grating is formed in the tapered dual-core fiber. The propagation equations for the field amplitudes of the even and odd modes in a dual-core fiber with an antisymmetric long-period grating are derived using a perturbation analysis by reciprocity theorem [97] leading to

$$\frac{\partial \tilde{A}_e}{\partial z} = i\left(\beta_e - \beta_{e,0}\right)\tilde{A}_e + i\exp\left[i\left(q\frac{2\pi}{\Lambda} - \left(\beta_{e,0} - \beta_{o,0}\right)\right)z\right]\kappa_{e,o}\tilde{A}_o \tag{5-1}$$

$$\frac{\partial \tilde{A}_o}{\partial z} = i\left(\beta_o - \beta_{o,0}\right)\tilde{A}_o + i\exp\left[i\left(-q\frac{2\pi}{\Lambda} + \left(\beta_{e,0} - \beta_{o,0}\right)\right)z\right]\kappa_{o,e}\tilde{A}_e \tag{5-2}$$

where $\tilde{A}_m$, β_m are respectively the electric field amplitude and the propagation constant of mode *m*, $\beta_{m,0} = \beta_m|_{\lambda=\lambda_0}$ with λ_0 being the carrier wavelength of an optical signal, *q* is an integer, Λ is the grating period, $\kappa_{o,e}$ and $\kappa_{e,o}$ are the coupling coefficients with $\kappa_{o,e} = \kappa^*_{e,o}$. The coupling coefficients are calculated using

$$\kappa_{e,o} = \kappa^*_{o,e} = a_q \frac{\omega_0 \varepsilon_0}{2N_o N_e}\iint n\left[u_1 - u_2\right]\vec{F}^*_e \cdot \vec{F}_o dxdy$$

where $\boldsymbol{\varepsilon}_0$ is the permittivity of free space, $\omega_0 = 2\pi c/\lambda_0$ is the optical angular frequency, *c* is the speed of light in free space, $N_m = 0.5\iint\left(\vec{F}_m \times \vec{F}^*_m\right)\cdot\hat{z}\partial x \partial y$ is the field normalization factor, *n* is the refractive-index, $\vec{F}_m$, $\vec{G}_m$ are respectively the electric and magnetic field distributions of mode *m*, a_q is the amplitude of the refractive-index change, $u_j(x,y)$ equals 1 in core *j* and 0 elsewhere.

Optimal coupling between the even and odd modes occurs at a grating resonance-wavelength λ_r defined as the wavelength λ_0 at which the phase-matching condition $q2\pi/\Lambda = \beta_{e,0} - \beta_{o,0}$ is satisfied. When the pulse utilized for inscribing the long-period grating has a relatively narrow spectral-width such that $\beta_m = \beta_{m,c}$ where $\beta_{m,c} = \beta_m|_{\lambda=\lambda_c}$, then $\Lambda = 2\pi/(\beta_{e,c} - \beta_{o,c})$

and $\lambda_r = \lambda_c$. Using $q = 1$ and $\Lambda = 2\pi/(\beta_{e,r} - \beta_{o,r})$ with $\beta_{m,r} = \beta_m|_{\lambda=\lambda r}$, Eqs. 1 and 2 reduce to a system of ordinary differential equations

$$\frac{\partial \tilde{A}_e}{\partial z} = i\left(\beta_e - \beta_{e,r}\right)\tilde{A}_e + i\kappa_{e,o}\tilde{A}_o \tag{5.3}$$

$$\frac{\partial \tilde{A}_o}{\partial z} = i\left(\beta_o - \beta_{o,r}\right)\tilde{A}_o + i\kappa_{o,e}\tilde{A}_e \tag{5.4}$$

which have a solution

$$\begin{pmatrix} \tilde{A}_e \\ \tilde{A}_o \end{pmatrix} = \exp\begin{pmatrix} i\left(\beta_e - \beta_{e,r}\right)z & i\kappa_{e,o}z \\ i\kappa_{o,e}z & i\left(\beta_o - \beta_{o,r}\right)z \end{pmatrix}\begin{pmatrix} \tilde{A}_{e,0} \\ \tilde{A}_{o,0} \end{pmatrix} \tag{5.5}$$

The output of core 1 is given by $E_1(L) = [E_e(L)+E_o(L)]/2$, the output of core 2 is given by $E_2(L) = [E_e(L)-E_o(L)]/2$, and the transmission of the dual-core fiber is given by $T = |E_1(L)|^2/|E_1(0)|^2$, where $E_m(z) = \tilde{A}_m(z)\exp\left(i\beta_{m,0}z\right)$ for mode m and L is the length of the dual-core fiber.

A scalar field-correction method [49, 98] is utilized to calculate F_e, F_o, β_e, and β_o for a dual-core As_2Se_3-PMMA fiber with 1.5 μm As_2Se_3 cores, and a core separation of 1.25 μm. A core separation of 1.25 μm is used in the numerical calculations because the As_2Se_3 cores of the tapered dual-core fiber slightly fuse during the fabrication process [49]. The value of $\kappa_{e,o}(\lambda)$ is calculated using a_q, F_e, F_o, and then $\kappa_{e,o}(\lambda)$, $\beta_e(\lambda)$ and $\beta_o(\lambda)$ are utilized to calculate the transmission of the dual-core fiber that is inscribed with an antisymmetric long-period grating.

The numerically calculated values of $\beta_e(\lambda)$, $\beta_o(\lambda)$, $\kappa_{e,o}(\lambda)/a_q$ are closely fitted by $\beta_e(\lambda)= -7.4439\times10^{12}\lambda+2.2609\times10^{7}$, $\beta_o(\lambda)=-7.5341\times10^{12}\lambda+2.2623\times10^{7}$, and $\kappa_{e,o}(\lambda)/a_q= -2.4489\times10^{12}\lambda+7.6594\times10^{6}$. The grating period Λ of the grating is determined by λ_c and is given by $\Lambda = 2\pi/[\beta_e(\lambda_c)-\beta_o(\lambda_c)] = 50$ μm. Figure 5-3 presents the calculated transmission spectra of the dual-core fiber with an antisymmetric long-period grating as a_q is increased from 0 to 4.0×10^{-5} in steps of 1.33×10^{-6}. The calculated transmission spectra in Fig. 5-3 show similar progression behavior to that of the experimentally observed spectra in Fig 5-1(c) which confirms the formation of an antisymmetric long-period grating and indicates that the magnitude of the refractive-index change a_q increases as the exposure time t_c increases.

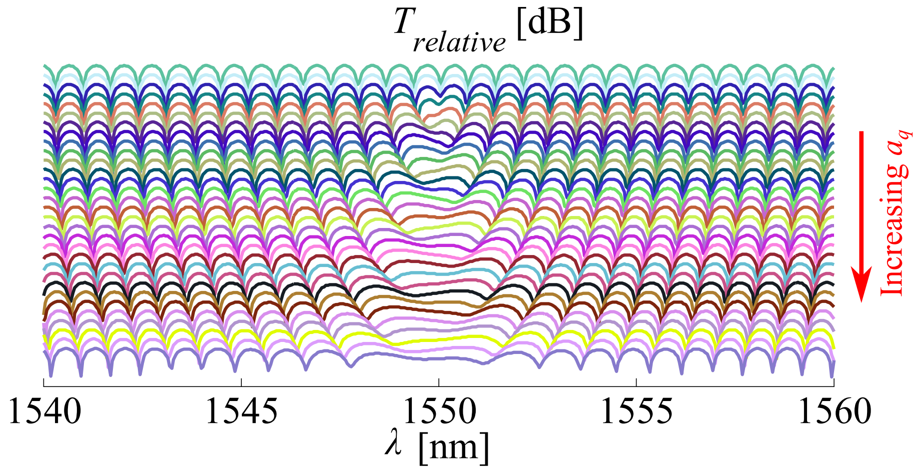

Figure 5- 3. Evolution of the theoretically calculated transmission spectrum of core 1 of a dual-core fiber with an antisymmetric long-period grating as the amplitude of the refractive-index change a_q is increased from 0 to 4.0×10^{-5} in steps of 1.33×10^{-6}.

The difference between the phases of the even and odd modes $\Delta\phi=\phi_e-\phi_o$, where ϕ_m is the phase of the electric field in mode m, is deduced from the transmission spectra in Fig 5-1(c). The phase-difference $\Delta\phi$ is a function of both the wavelength λ and the cumulative exposure time t_c, and is given by $\Delta\phi(\lambda, t_c) = (2p+1)\pi$ at the minima where p is an integer. As the exposure time is increased by Δt_c, the values of $\Delta\phi$ corresponding to the minima on the transmission spectrum do not change leading to $(\partial\Delta\phi/\partial\lambda)\Delta\lambda+(\partial\Delta\phi/\partial t_c)\Delta t_c=0$. The minima at $\lambda<\lambda_r$ shift towards longer wavelengths as t_c increases corresponding to $\Delta\lambda> 0$, hence, $\partial\Delta\phi/\partial\lambda$ and $\partial\Delta\phi/\partial t_c$ have opposite signs. Simulations of the dual-core fiber show that $\partial\Delta\phi/\partial\lambda > 0$ leading to $\partial\Delta\phi/\partial t_c < 0$, which indicates that $\Delta\phi$ decreases as t_c increases for $\lambda<\lambda_r$. Similarly, the minima at $\lambda>\lambda_r$ shift towards shorter wavelengths corresponding to $\Delta\lambda < 0$ as t_c increases, which indicates that $\Delta\phi$ increases as t_c increases for $\lambda>\lambda_r$. Finally, the transmission spectra have slower oscillations near λ_r which indicates that $\Delta\phi$ has a slower variation with λ. Figure 5-4 presents $\Delta\phi$ as a function of λ which is deduced from the information that $\Delta\phi$ decreases for $\lambda<\lambda_r$, increases for $\lambda>\lambda_r$, and has slow variation near λ_r.

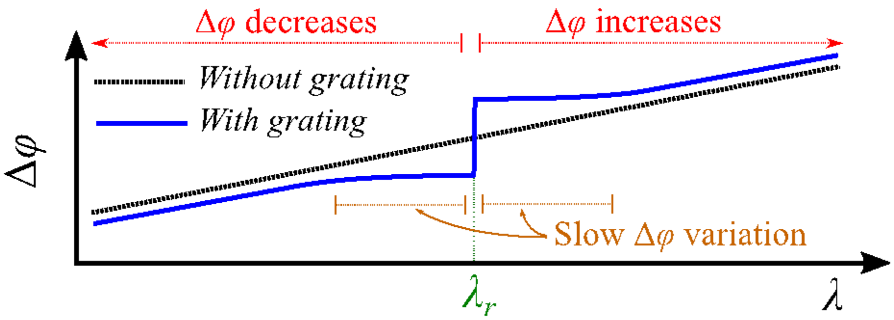

Figure 5- 4. Illustration of the difference between the phases of even and odd modes before and after inscription of the antisymmetric long-period grating.

The illustration in Fig. 5-4 shows that $\Delta\phi(\lambda)$ has slow variation near λ_r indicating effective group-velocity matching. The dual-core fiber is multimode as it supports an even mode and an odd mode. The antisymmetric long-period grating causes the electric fields to couple back and forth between the even and odd modes, and hence, the fields travel half the propagation distance in the even mode and the other half in the odd mode leading to effective group-velocity matching. To illustrate this, we did the following derivations:

The group velocity is given by

$$V_g = \frac{d\omega}{d\beta}$$

And the difference between the group velocities of the even and odd modes is given by

$$V_{g,e} - V_{g,o} = \left(\frac{d\beta_e}{d\omega}\right)^{-1} - \left(\frac{d\beta_o}{d\omega}\right)^{-1}$$

$$= \left(\frac{d\beta_e}{d\lambda}\frac{d\lambda}{d\omega}\right)^{-1} - \left(\frac{d\beta_o}{d\lambda}\frac{d\lambda}{d\omega}\right)^{-1}$$

Considering that $\frac{d\omega}{d\lambda} = -\frac{2\pi c}{\lambda^2}$,

$$V_{g,e} - V_{g,o} = -\frac{\lambda^2}{2\pi c}\left(\left(\frac{d\beta_e}{d\lambda}\right)^{-1} - \left(\frac{d\beta_o}{d\lambda}\right)^{-1}\right)$$

$$= \frac{\lambda^2}{2\pi c}\frac{\frac{d\Delta\beta}{d\lambda}}{\left(\frac{d\beta_e}{d\lambda}\right)\bullet\left(\frac{d\beta_o}{d\lambda}\right)}$$

$$= \frac{\lambda^2}{2\pi cL}\frac{\frac{d\Delta\phi}{d\lambda}}{\left(\frac{d\beta_e}{d\lambda}\right)\bullet\left(\frac{d\beta_o}{d\lambda}\right)}$$

where $\Delta\phi = \Delta\beta L$, $\Delta\beta = \beta_e - \beta_o$ with β_e and β_o the propagation constants of the even and odd modes, respectively, L is the length of the taper, λ is the wavelength and c is the velocity of light.

The group velocities $V_{g,e}$ and $V_{g,o}$ of the even and odd modes are matched because $V_{g,e} - V_{g,o} = 0$ when the value of $d\Delta\phi / d\lambda = 0$. As illustrated in Fig. 5-4, $\Delta\phi(\lambda)$ has slow variation near the resonance wavelength λ_r indicating $d\Delta\phi / d\lambda \to 0$. Group-velocity matching can be used for enhanced nonlinear processing of sub-picosecond pulses due to a short pulse walk-off, and for increased efficiency of phase-matched four-wave mixing.

5.1.4. Applications based on the group-velocity matching in the dual-core fibers

Fast variation of $\Delta\phi$ at λ_r in Fig. 5-4 implies that ϕ_e and ϕ_o have fast variations with wavelength indicating the potential for inducing a slow light propagation velocity. This is the first time to our knowledge that long-period gratings are shown to have the potential for achieving slow light. This slow light feature can be utilized for the implementation of highly sensitive devices for the measurement of temperature and refractive-index change of a liquid solution. Furthermore, As_2Se_3-PMMA fiber tapers are highly nonlinear [35, 93], and the introduction of slow light will further enhance the waveguide nonlinearity parameter [99]. Moreover, antisymmetric long-period gratings can be inscribed in long dual-core fibers allowing for long propagation delays. Finally, the group-velocity matching induced by the antisymmetric-long period grating can enhance the efficiency of nonlinear effects such as broadening the gain bandwidth of the four-wave mixing (FWM). To illustrate this, we give the following description.

The maximum gain of FWM occurs when effective phase mismatch

$$\kappa = \Delta\beta + \gamma P_0 L = 0$$

where $\Delta\beta = (\beta_3 + \beta_4) - (\beta_1 + \beta_2)$ with β being the propagation constant, γ is the waveguide nonlinearity, P_0 is the peak power of the signal, and L is the length of the waveguide.

We denote $\beta_e(\omega)$ and $\beta_o(\omega)$ as the propagation constants of the even and odd modes, which leads to

$$\Delta\beta = (\beta_e(\omega_3) + \beta_o(\omega_4)) - (\beta_e(\omega_1) + \beta_o(\omega_2))$$

$$= (\beta_e(\omega_0 + \Delta\omega) + \beta_o(\omega_0 - \Delta\omega)) - (\beta_e(\omega_0) + \beta_o(\omega_0))$$

where $\omega_1 = \omega_2 = \omega_0$, $\omega_3 = \omega_0 + \Delta\omega$ and $\omega_4 = \omega_0 - \Delta\omega$.

Expanding $\beta_e(\omega)$ and $\beta_o(\omega)$ as a Taylor series around ω_0, we obtain

$$\beta_e(\omega) = \beta_e^{(0)} + \beta_e^{(1)}(\Delta\omega) + 0.5\beta_e^{(2)}(\Delta\omega)^2$$

$$\beta_o(\omega) = \beta_o^{(0)} + \beta_o^{(1)}(\Delta\omega) + 0.5\beta_o^{(2)}(\Delta\omega)^2$$

where $\Delta\omega = \omega - \omega_0$, $\beta^{(0)} = \beta(\omega)|_{\omega=\omega_0}$, $\beta^{(1)} = \dfrac{d\beta(\omega)}{d\omega}|_{\omega=\omega_0}$, $\beta^{(2)} = \dfrac{d^2\beta(\omega)}{d\omega^2}|_{\omega=\omega_0}$.

This leads to

$$\Delta\beta = \left(\beta_e^{(0)} + \beta_e^{(1)}(\Delta\omega) + 0.5\beta_e^{(2)}(\Delta\omega)^2\right) + \left(\beta_o^{(0)} + \beta_o^{(1)}(-\Delta\omega) + 0.5\beta_o^{(2)}(-\Delta\omega)^2\right) - \left(\beta_e^{(0)} + \beta_o^{(0)}\right)$$

$$= \left(\beta_e^{(1)} - \beta_o^{(1)}\right)\Delta\omega + 0.5\left(\beta_e^{(2)} + \beta_o^{(2)}\right)\Delta\omega^2$$

To achieve the phase matching condition, $\kappa = \Delta\beta + \gamma P_0 L = 0$ and we ignore the second term in the expression of $\Delta\beta$ and get

$$\kappa = \left(\beta_e^{(1)} - \beta_o^{(1)}\right)\Delta\omega + \gamma P_0 L = 0$$

The bandwidth with the maximum gain is given by

$$\Delta\omega = \frac{-\gamma P_0 L}{\beta_e^{(1)} - \beta_o^{(1)}}$$

$$\Delta\omega = \frac{-\gamma P_0 L^2}{\frac{d\Delta\phi}{d\lambda}}$$

According to the expression of $\Delta\omega$, the group velocity matching can induce the enlargement of the bandwidth with the maximum gain.

5.1.5. Conclusion

We report the first observation of self-inscribed antisymmetric long-period grating in a tapered dual-core As_2Se_3-PMMA fiber. Propagation of optical pulses centered at wavelength of 1550 nm in a dual-core As_2Se_3-PMMA fiber leads to the inscription of an antisymmetric long-period grating on the tapered fiber due to photosensitivity of As_2Se_3 at 1550 nm. Experimental results show that antisymmetric long-period gratings in dual-core fibers can be used to achieve group-velocity matching for nonlinear processing of sub-picosecond optical pulses. Experimental results also show the potential for achieving slow light velocity in dual-core fibers with antisymmetric long-period gratings.

5.2 Temperature-sensitivity enhancement in a tapered dual-core As_2Se_3-PMMA fiber with an antisymmetric long-period grating

We propose and demonstrate an approach for temperature-sensitivity enhancement by a factor of 4.0 based on effective group-velocity matching between the even and odd modes of a dual-core As_2Se_3-PMMA taper on which an antisymmetric long-period grating is inscribed. The transmission of optical pulses in the dual-core As_2Se_3-PMMA taper inscribes the antisymmetric long-period grating that causes the electric fields to couple back and forth between the even and odd modes leading to effective group-velocity matching between the two modes. The variation of the difference between phases of the two modes with respect to wavelength tends to 0 ($\partial\phi_d(\lambda)/\partial\lambda\rightarrow0$) near the resonance wavelength of the grating due to the effective group-velocity matching between the two modes, and consequently, thermally-induced change of the difference between phases of the two modes $\phi_d(\lambda)$ leads to a large wavelength shift indicating enhancement of the temperature measurement sensitivity. The sensitivity of temperature measurement in the wavelength range with effective group velocity matching is enhanced by a factor of 4.0 in comparison with that in the wavelength range that does not have effective group velocity matching. The effective group-velocity matching between modes in fibers opens the path towards the realization of novel high-sensitivity sensors for temperature and strain measurement.

5.2.1 Background

Temperature measurement based on fiber optics has been extensively investigated using Fiber Bragg gratings (FBG) [61, 100], long-period fiber gratings (LPFGs) [101, 102], polarization maintaining fibers [103], core-diameter mismatching method [104] and other techniques [52, 53, 105]. Most of the demonstrated silica-fiber-based temperature sensors are implemented by the measurement of the wavelength shift of the spectrum caused by the thermally-induced refractive-index change and thermally-induced fiber length variation. However, the temperature measurement sensitivity in silica fibers is low due to the low values of the thermo-optic coefficient (5.81×10^{-6}/°C [106]) that is defined as the change in refractive index with respect to temperature and the thermal-expansion coefficient (0.5×10^{-6}/°C [21]) that describes how the length of a fiber changes with temperature. One common method to enhance the temperature measurement sensitivity is to design fibers using materials with high values of the thermal-expansion coefficient and high thermo-optic coefficient. For example, a high-sensitivity temperature measurement sensor is designed based on a fiber loop mirror combined with an alcohol-filled high-birefringence photonic crystal fiber [107]. The high sensitivity for temperature measurement is realized by measuring the thermally-induced wavelength shift of the resonance of dips due to the high thermo-optic coefficient of alcohol. Another example, high-sensitivity temperature measurement is achieved in polymer optical fibers based on the large value of the thermal-expansion coefficient of the polymer materials [85, 108, 109].

The inscription of fiber Bragg gratings in tapered single-core As_2Se_3-PMMA fibers has been reported due to photosensitivity of As_2Se_3 glass to optical signals at 1550 nm [39]. It has also been reported recently that the propagation of optical pulses with high peak-power in a tapered dual-core As_2Se_3-PMMA fiber leads to the inscription of an antisymmetric long-period grating at 1550 nm [86], which is discussed in Section 5.1. The antisymmetric long-period grating causes the input electric fields to couple back and forth between the even and odd modes. The electric fields travel half the propagation distance in the even mode and the other half in the odd mode leading to effective group-velocity matching between the two modes.

In this section, we demonstrate for the first time that temperature measurement sensitivity is enhanced by the antisymmetric-long-period-grating-induced effective group-velocity matching between the even and odd modes in a tapered dual-core As_2Se_3-PMMA fiber. Theoretical analysis and numerical simulation results show that temperature measurement sensitivity is enhanced when $\partial\phi_d(\lambda)/\partial\lambda \rightarrow 0$ where $\phi_d(\lambda)$ is the difference between phases of the even and odd modes, which indicates effective group velocity matching can be utilized for temperature sensitivity enhancement in tapered dual-core As_2Se_3-PMMA fibers. In comparison with the measured results in the wavelength range without the effective group velocity matching, temperature measurement sensitivity enhancement by a factor of 4.0 is experimentally observed within the wavelength range of effective group velocity matching.

5.2.2 Analytical model

The tapered dual-core As_2Se_3-PMMA fiber is multimode as it carries two modes: an even mode and an odd mode [49]. When $\phi_d(\lambda, T)$ satisfies the condition $\phi_d(\lambda, T) = (2m+1)\pi$, where m is an integer, troughs are observed in the transmission spectrum of the dual-core fiber. Variation in the temperature of the fiber changes the difference of the refractive index between the two modes Δn_{eff} and the fiber length L_w leading to a wavelength shift of the troughs. The wavelength-shift is given by Eq. (2.1) in Chapter 2.

The illustration in Fig. 5-5 shows that, at temperature T_0 and $T_0+\Delta T$, the difference between the phases of the even and odd modes of dual-core fibers (a) without group velocity matching and (b) with group velocity matching as a function of wavelength. As presented in Fig. 5-5(a), for dual-core fibers without group velocity matching, the thermally-induced wavelength shifts of both troughs are the same, $\Delta\lambda_1=\Delta\lambda_2$, since the values of $\partial\phi_d(\lambda)/\partial\lambda$ are constant. However, temperature sensitivity is enhanced for fibers with group velocity matching where the wavelength shift of trough II is larger than that of trough I such that $\Delta\lambda_4>\Delta\lambda_3$ due to the smaller value of $\partial\phi_d(\lambda)/\partial\lambda$ at wavelength of trough II, as illustrated in Fig. 5-5(b).

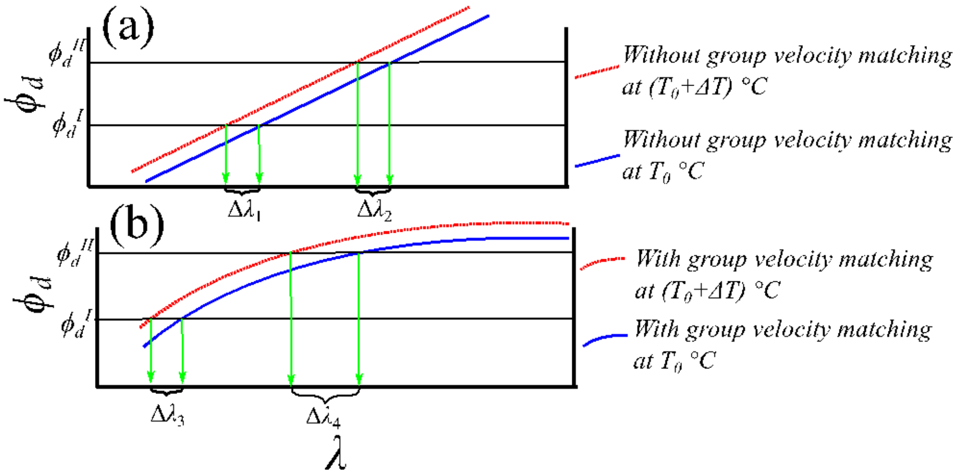

Figure 5- 5. Illustration of the difference between phases of even and odd modes in dual-core fibers (a) without group velocity matching and (b) with group velocity matching as a function of wavelength at temperature T_0 and $T_0+\Delta T$. Wavelength shift of troughs I and II for which $\phi_d(\lambda,T)$ satisfies $\phi_d^{I}=(2m+1)\pi$ and $\phi_d^{II}=(2(m+k)+1)\pi$, respectively, where m and k are integers, as

temperature changes, is larger when the trough wavelength lies within the wavelength range where $\partial\phi_d(\lambda)/\partial\lambda\rightarrow0$.

5.2.3 Numerical simulations

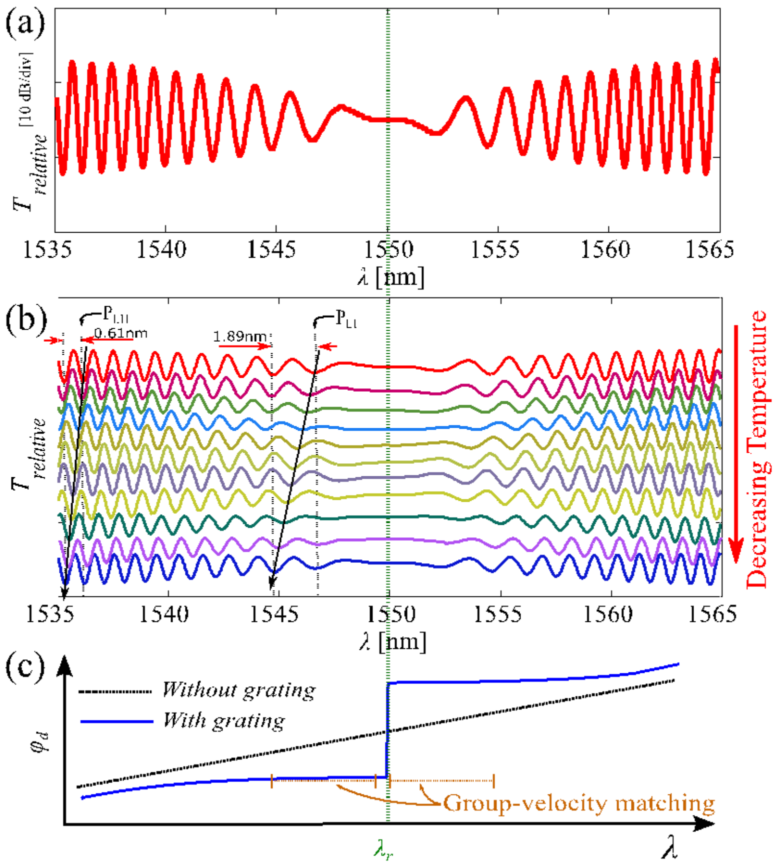

Figure 5- 6. (a) Typical calculated transmission spectrum of a dual-core As_2Se_3-PMMA fiber with an antisymmetric long period grating for which the amplitude of the refractive-index change is 1.0×10^{-4}. (b) The calculated evolution of transmission spectrum as a function of temperature. (c) Illustration of the difference between phases of the even and odd modes dependence on wavelength before and after exposure to optical pulses [86]. λ_r is the resonance wavelength of the grating.

Numerical simulations are also performed to show temperature sensitivity enhancement over the wavelength range around effective group velocity matching. The transmission spectrum of the tapered dual-core As_2Se_3-PMMA fiber on which an antisymmetric long-period grating is inscribed is calculated based on the ordinary differential equations [86] given by Eqs. (5-3) and (5-4):

$$\frac{\partial \tilde{A}_e}{\partial z} = i\left(\beta_e - \beta_{e,r}\right)\tilde{A}_e + i\kappa_{e,o}\tilde{A}_o \tag{5.3}$$

$$\frac{\partial \tilde{A}_o}{\partial z} = i\left(\beta_o - \beta_{o,r}\right)\tilde{A}_o + i\kappa_{o,e}\tilde{A}_e \tag{5.4}$$

The solution is given by Eq. (5-5):

$$\begin{pmatrix} \tilde{A}_e \\ \tilde{A}_o \end{pmatrix} = \exp\begin{pmatrix} i\left(\beta_e - \beta_{e,r}\right)z & i\kappa_{e,o}z \\ i\kappa_{o,e}z & i\left(\beta_o - \beta_{o,r}\right)z \end{pmatrix}\begin{pmatrix} \tilde{A}_{e,0} \\ \tilde{A}_{o,0} \end{pmatrix} \tag{5.5}$$

where $\tilde{A}_m$, β_m are the electric field amplitude and the propagation constant of mode m , respectively, $\beta_{m,0} = \beta_m |_{\lambda = \lambda 0}$ with λ_0 being the carrier wavelength of an optical signal, $\kappa_{o,e}$ and $\kappa_{e,o}$ are the coupling coefficients. Temperature variation changes the values of the fiber length L_W and the propagation constants of the even and odd modes $\beta_e(\lambda)$, $\beta_o(\lambda)$ whose numerical values are calculated utilizing Comsol Multiphysics software leading to the wavelength shift of troughs in the transmission spectrum.

Figure 5-6(a) presents the calculated transmission spectrum of the dual-core fiber with an antisymmetric long-period grating for which the amplitude of the refractive-index change is 1.0×10^{-4}. The transmission spectrum has slower oscillations around λ_r where λ_r is the resonance wavelength of the grating indicating the formation of an antisymmetric long-period grating in a tapered dual-core As_2Se_3-PMMA fiber. Figure 5-6(b) presents the evolution of the calculated transmission spectrum as a function of temperature showing that the troughs shift towards shorter wavelength as the temperature decreases. The absolute value of wavelength shift $|\Delta\lambda|$ increases for $\lambda < \lambda_r$; trough P_{L1} has the largest wavelength shift while trough P_{L11} shifts the smallest. Figure 5-6(c) presents an illustration of the difference between phases of the even and odd modes dependence on wavelength before and after the inscription of the antisymmetric long-period grating given in Fig. (5-4) and shows that ϕ_d decreases for $\lambda < \lambda_r$, increases for $\lambda > \lambda_r$, and has slow variation near λ_r indicating $\partial\phi_d(\lambda)/\partial\lambda$ tends to zero near the antisymmetric long-period grating resonance wavelength around λ_r =1550 nm. The trough P_{L11} has a wavelength shift of 0.61 nm, but the trough P_{L1} has a larger wavelength shift of 1.89 nm because the value of the $\partial\phi_d(\lambda)/\partial\lambda$ is larger at P_{L1}. These results demonstrate that the effective group velocity matching can be utilized for temperature sensitivity enhancement in tapered dual-core As_2Se_3-PMMA fibers. Furthermore, the numerical simulation results agree with Eq. (2.1) in which the wavelength shift $\Delta\lambda$ induced by variation in the temperature of the dual-core taper is enhanced when $\partial\phi_d/\partial\lambda\rightarrow 0$ leading to sensitivity enhancement.

5.2.4 Experiment and Results

Two As_2Se_3 fibers are coated with a PMMA layer to make a dual-core As_2Se_3-PMMA preform that is drawn to obtain As_2Se_3-PMMA fibers with As_2Se_3 core diameter of 21.25 µm. A 7 cm-long fiber section is cut and both ends of the fiber are finely polished. Figure 5-7 presents an image of the polished dual-core fiber end showing two fused As_2Se_3 fibers and a surrounding PMMA cladding. The two polished ends are butt-coupled to standard single mode fibers and the conjunctions are bonded permanently using UV epoxy. Then the fiber is tapered down to get a 10 cm-long dual-core As_2Se_3-PMMA fiber with As_2Se_3 core diameter of 1.5 µm. An antisymmetric long-period grating is inscribed by launching optical pulses into one of the principal axes of the tapered dual-core fiber with a pulse width of 10 ns, a peak power of 23 dBm, a repetition rate of 1 MHz and a central wavelength at 1550 nm [86].

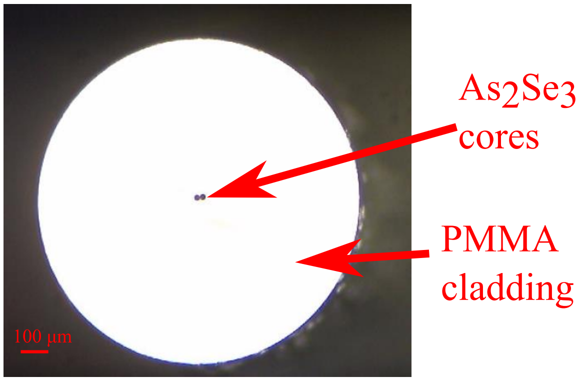

Figure 5- 7. An image of the polished end of the dual-core fiber showing the fused As_2Se_3 fibers and the surrounding PMMA cladding.

Figure 5-8(a) presents a schematic of the temperature measurement setup using a tapered dual-core As_2Se_3-PMMA fiber on which an antisymmetric long-period grating is inscribed. Light from a C-band erbium-doped fiber amplifier (EDFA) is passed through a linear polarizer (LP) followed by a polarization controller (PC) that is used to align the polarization of the input broadband light with one of the principal polarization axes of the dual-core fiber. The tapered dual-core fiber is placed in a water-bath whose temperature is raised to 45 ˚C. A thermocouple heat sensor (OMEGA Engineering) is used for the temperature measurement of the water bath at a resolution of 0.1 ˚C. Both the temperature of the water-bath and the transmission spectrum of the dual-core fiber are measured every 20 s as the temperature drops from 40 ˚C to 30 ˚C to obtain the evolution of the transmission spectrum as a function of temperature.

Figure 5-8(b) presents the evolution of the measured transmission spectra as a function of temperature showing that the troughs shift towards shorter wavelength as the temperature decreases. Trough P_{L1} has a larger wavelength shift because the antisymmetric long-period grating reduces the value of $\partial\phi_d(\lambda)/\partial\lambda$ near the resonance wavelength of the grating according to Fig. 5-6(c). Figure 5-8(c) presents the wavelength shift as a function of temperature for trough P_{L1} near the resonance wavelength of the grating and trough P_{L11} far away from the resonance wavelength of the grating. The sensitivity defined as the rate of wavelength shift as a function of temperature is 0.121 nm/ ˚C for trough P_{L1} and 0.030 nm/ ˚C for trough P_{L11} indicating temperature-sensitivity enhancement by a factor of 4.0. Sensitivity enhancement arises from effective group velocity matching by the antisymmetric long-period grating in the tapered dual-core As_2Se_3-PMMA fiber.

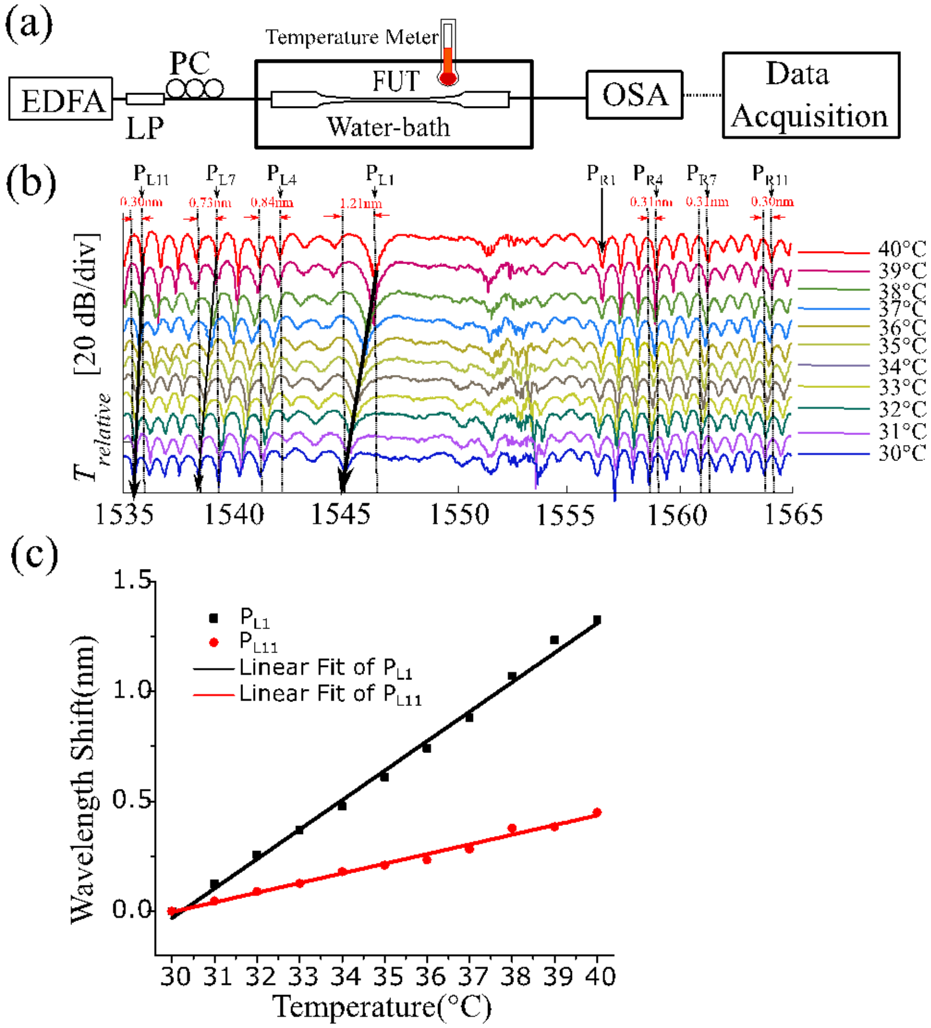

Figure 5- 8. (a) Schematic of the temperature measurement setup. (b) Measured transmission spectra as a function of temperature. (c) Temperature measurement result of P_{L1} and P_{L11}. P_{L1}: the first

trough on the left of the resonance wavelength, P_{L11}: the eleventh trough on the left of the resonance wavelength.

Strain measurement sensitivity can also be enhanced based on the antisymmetric long-period grating in a tapered dual-core As_2Se_3-PMMA fiber according to the expression of the strain sensitivity in Eq. (2.2). This will allow for high-sensitivity simultaneous temperature and strain measurement. Furthermore, other fibers such as single mode fibers and polarization maintaining fibers can also be utilized to achieve sensitivity enhancement of temperature and strain measurement based on the effective group velocity matching between the LP_{01} mode and LP_{11} mode near the cutoff wavelength of LP_{11} mode.

5.2.4 Conclusion

Temperature-sensitivity enhancement by a factor of 4.0 based on effective group-velocity matching between the even and odd modes in a tapered dual-core As_2Se_3-PMMA fiber on which an antisymmetric long-period grating is inscribed is demonstrated. Theoretical model and experimental results show that the sensitivity of temperature measurement is enhanced when $\partial\phi_d(\lambda)/\partial\lambda \rightarrow 0$ due to the effective group-velocity matching between the even and odd modes indicating that the effective group velocity matching can be used for temperature sensitivity enhancement in tapered dual-core As_2Se_3-PMMA fibers. The effective group-velocity matching between modes in fibers opens the path towards the realization of novel sensors and devices with high-sensitivity temperature and strain measurement.

Chapter 6 Modulation instability in a tapered dual-core As_2Se_3-PMMA fiber

In this chapter, we demonstrate modulation instability within the normal-dispersion regime in dual-core As_2Se_3-PMMA fiber. Many nonlinear systems exhibit an instability that leads to modulation of the steady state as a result of an interplay between the nonlinear and dispersive effects. This phenomenon is referred to as the modulation instability (MI), which amplifies weak perturbations and broadens the optical spectrum by the nonlinear Kerr effect. The phase matching condition shows that Modulation Instability depends critically on that light experiences anomalous dispersion in single-core fibers. However, a dual-core As_2Se_3-PMMA fiber in this chapter guides an even mode and an odd mode enables additional phase-matching conditions for modulation instability, which makes it possible in the normal dispersion regime.

6.1 Introduction

Nonlinear devices have a variety of practical applications including parametric amplification [110], all-optical switching [111], super-continuum generation [112, 113], and sensing applications [114]. Tapered chalcogenide-polymer fiber structures composed of an As_2Se_3 core and a polymethyl methacrylate (PMMA) cladding are a promising platform for nonlinear applications because the As_2Se_3 core provides high nonlinearity over the near- and mid-infrared spectral ranges for compact nonlinear devices with low power consumption and the PMMA cladding provides high mechanical strength for easy handling. Tapered As_2Se_3-PMMA fibers have been successfully used for super-continuum generation [35], broadband parametric amplification [38], polarization switching [93], and laser pulse generation [40].

Advanced As_2Se_3-PMMA fiber structures such as dual-core fibers that support guided propagation of an even mode and an odd mode will open the way for a variety of novel devices in the near- and mid-IR wavelength range.

MI (Modulation instability) is a process where weak modulations on a high-power optical signal are amplified and appears as a buildup of new optical frequencies on both sides of the optical signal spectrum. Interpretation of modulation instability as a four-wave mixing process shows that modulation instability arises by phase-matching the pump signal with light at surrounding wavelengths. Modulation instability in single-core As_2Se_3-PMMA fibers requires operation in the anomalous dispersion regime where phase-matching is possible [38]. The observation of MI of optical waves in the normal dispersion region has been accomplished in a strongly birefringent optical fiber [94]. Two orthogonal polarized waves co-propagate in a strong birefringent fiber, and the cross-phase modulation refers to the nonlinear phase change of an optical field in one polarization axis by the light in the other polarization axis. The added nonlinear phase changes the phase matching condition, which enables MI happen in normal dispersion regime. Theoretically MI in two core fibers with cases of both normal and anomalous dispersion has also been discussed [115, 116].

In this chapter, we report observation of modulation instability in tapered dual-core As_2Se_3-PMMA fibers. Dual-core As_2Se_3-PMMA fiber composed of two As_2Se_3 cores and a PMMA cladding are fabricated. The dual-core fiber is then tapered to a micro-wire with a length of 10 cm and an As_2Se_3 core diameter of 1.5 μm such that the cores have normal dispersion at $\lambda = 1550$ nm. Modulation instability induced in the normal dispersion regime is demonstrated in the fabricated dual-core As_2Se_3-PMMA micro-wire. The even and odd modes guided in the dual-core As_2Se_3-PMMA fibers enable additional phase change in the phase matching condition of the interplay between the nonlinear and dispersion effects so that the MI can be achieved in the normal dispersion region in the dual-core As_2Se_3-PMMA fibers.

6.2 MI Theory in dual-core fiber

Based on the coupled-mode theory, the evolution of the electric-field along the dual-core fiber is described by the coupled nonlinear Schrödinger equations [115]:

$$i\frac{\partial a_1}{\partial z}-\frac{1}{2}\beta_2\frac{\partial^2 a_1}{\partial t^2}+\gamma\left|a_1\right|^2 a_1+Ca_2+iC_1\frac{\partial a_2}{\partial t}=0 \tag{6.1}$$

$$i\frac{\partial a_2}{\partial z}-\frac{1}{2}\beta_2\frac{\partial^2 a_2}{\partial t^2}+\gamma\left|a_2\right|^2 a_2+Ca_1+iC_1\frac{\partial a_1}{\partial t}=0 \tag{6.1}$$

where a_i is the slowly varying electric-field envelope in core i, i=1 or 2; z and t are the propagation distance and the time coordinate, respectively; β_2 measures the group velocity dispersion (GVD) at the carrier frequency; γ is the waveguide nonlinearity parameter with $\gamma = 2\pi n_2/(\lambda A_{eff})$, where λ, n_2, and A_{eff} are the free-space optical wavelength, nonlinear Kerr coefficient of the fiber material, and the effective area of the fiber core, respectively; C is the coupling coefficient; $C_1 = dC/d\omega$ is the coupling–coefficient dispersion, which shows that the coupling coefficient between the two cores depends on the optical wavelength [117, 118].

Equations (6.1) and (6.2) lead to three families of stationary solutions: symmetric, antisymmetric, and asymmetric ones [119, 120]. The symmetric and antisymmetric solutions are for the situation where the optical power is equal in the two cores. The symmetric solution corresponds to the even mode for which the electric fields have the same direction in the two cores, while the antisymmetric one corresponds to the odd mode for which the electric fields in the two cores have the opposite directions. The asymmetric solution applies to the unequal power in the two cores. The two cores in the dual-core PMMA taper are not guaranteed exactly in the center of the fiber for the homemade preform, which may lead slightly diameter difference between the two cores during the drawing process. The power in the two cores are not exactly the same, which apply to the asymmetric solution of Eqs. (6.1) and (6.2). Based on the weak perturbation theoretical analysis in ref. [115], we take β_2 =2.07 ps^2/m [35], $\gamma = 1.6\times10^5/(kW\bullet m)$, $C = 200/m$, $C_1 = -12/m$ and the total input power $P = 3W$ at the wavelength of $\lambda = 1550nm$ and figure 6-1 presents the calculated MI spectrum showing that two sidebands appear on both sides of the input optical spectrum.

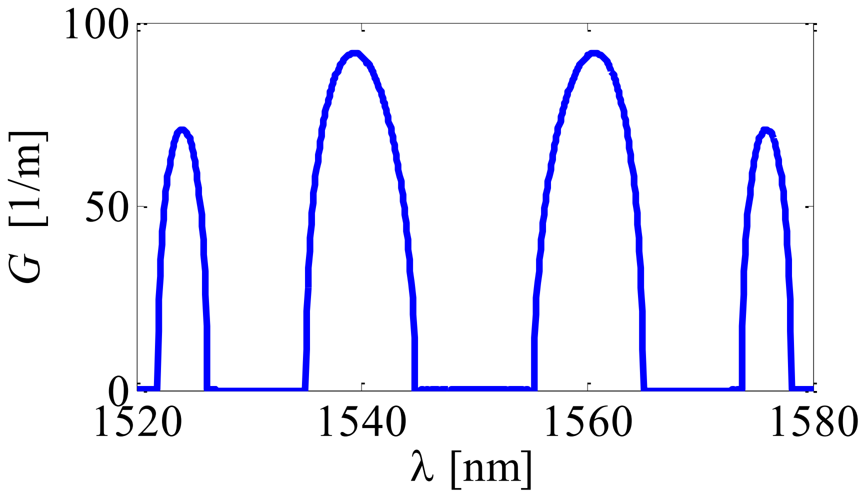

Figure 6- 1. Modulation instability gain spectrum calculated for the normal dispersion regime with β_2 =2.07 ps^2/m, $\gamma = 1.6\times10^5/(kW\bullet m)$, $C = 200/m$, $C_1 = -12/m$ and the total input power $P = 3W$ at the wavelength of $\lambda = 1550nm$.

6.3 Modulation instability characterization

The dual-core fiber is tapered using the heat-brush method [34, 69-71] to obtain a micro-wire with D_{AsSe}^{core} =0.85 µm, D_{AsSe}^{cl} =1.5 µm, D_{PMMA}^{cl} =84.7 µm, a length *L*=10 cm. Figure 6-2(a) presents the setup utilized for the observation of modulation instability in the tapered dual-core As_2Se_3/PMMA fiber. Laser pulses centered at λ =1550 nm with a pulse width of 20 ps and a repetition rate of 20 MHz are generated from a mode-locked laser source (Pritel FFL-1550-20). The output of the pulsed laser is passed to an electro-optic modulator (Photline MXER-LN-10) that is driven by an electrical square pulse with duration of 100 ns and a period of 1 μs to reduce the average power of the pulsed laser source by 10 dB to avoid over-heating the tapered dual-core fiber. The optical pulses are then launched into the tapered dual-core fiber, and the output of the dual-core fiber is observed using an optical spectrum analyzer (Yokogawa, AQ6375) at a resolution-bandwidth of 0.1 nm. A variable attenuator is utilized to change the pulse peak power and a polarization controller is utilized to align the polarization of the optical pulses with one of the principal polarization axes of the dual-core fiber taper.

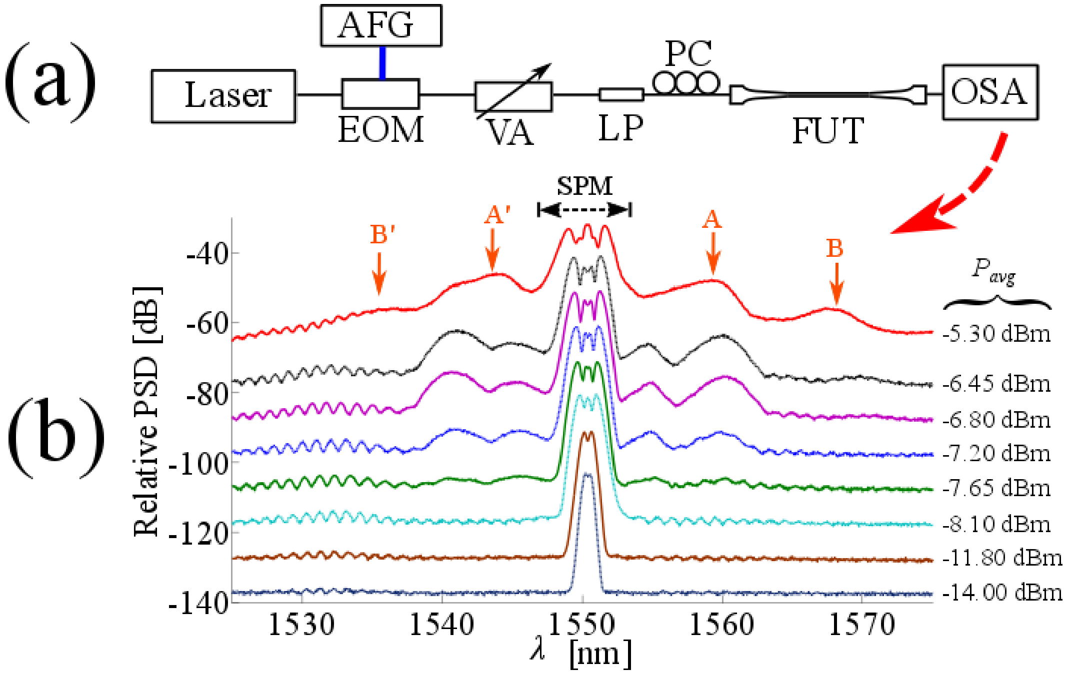

Figure 6- 2. (a) Schematic of the modulation instability characterization setup, and (b) relative values of the measured spectra at the output of the dual-core fiber as the input pulse power is increased. PSD: Power spectral density. AFG: arbitrary function generator; EOM: electro-optic modulator; VA: variable attenuator; LP: linear polarizer; PC: polarization controller; FUT: fiber-under-test; OSA:

optical spectrum analyzer; SPM: self-phase modulation.

Figures 6-2(b) presents relative values of the measured spectra at the output of the dual-core fiber as the input pulse power P_{avg} is increased. A periodic power variation is observed in the noise floor of the laser signal showing the dual-core fiber transmission response that arises from the wavelength dependence of the coupling coefficient. As the laser power is increased, the pulses spectrum broadens due to self-phase modulation in the dual-core fiber. Also, two peaks, peak A and peak B, appear in the modulation instability gain spectra when P_{avg}= -7.65 dBm. Multiple peaks arise due to the strong wavelength dependence of the coupling coefficient in the dual-core fiber. The corresponding four-wave mixing process involves the conversion of two photons from the even mode of the dual-core fiber, and the generation of two new photons in the odd mode.

6.4 Conclusion

We report the first observation of modulation-instability in the normal-dispersion regime of a dual-core As_2Se_3-PMMA fiber. The modulation instability spectrum shows multiple peaks arising from the strong wavelength dependence of the coupling coefficient. Modulation instability in dual-core fibers can be used for enhanced parametric amplification, broadly tunable lasers, and efficient entangled photon generations.

Chapter 7 Investigation of forward stimulated Brillouin scattering in single-core As_2Se_3-PMMA tapers

In this chapter, we review the recent work about the forward stimulated Brillouin scattering and its sensing applications. The forward stimulated Brillouin scattering by the radial and torsional-radial guided acoustic modes of silica fibers and tapered single-core As_2Se_3-PMMA fibers is investigated experimentally and the preliminary results are presented. Sensing applications such as acoustic impedance measurement of the surrounding medium and taper dimension characterization can be achieved based on cavity lifetime measurements of multiple modes due to the acoustic reflectivity at the outer cladding boundary.

7.1 Background

Tight confinement of both acoustic vibrations and light in a small space can lead to strong interactions between them. Acousto-optic interactions [121-127] has been studied extensively such as forward stimulated Brillouin scattering [126], backward stimulated Brillouin scattering [121], and Raman-like scattering by acoustic phonons [125].

Guided acoustic-wave Brillouin scattering (GAWBS) occurs by the interaction between incident light and acoustic waves propagating in the cross-sectional area of the fiber [121]. The scattered light propagates with the pump light in the same direction, which is known to be forward stimulated Brillouin scattering (FSBS) that accompanies multiple spectral peaks caused by acoustic resonance. Several fiber structural parameters can influence the spectrum of the FSBS, such as a fiber outer diameter, a core diameter, and a refractive index profile [128]. GAWBS can be categorized into two types based on the acoustic modes in fibers: one is polarized GAWBS caused by the radial-mode ($R_{0,m}$) that perturbs the refractive index of the fiber cross-section, and the other is depolarized GAWBS caused by the torsional-radial-mode ($TR_{p,m}$) that perturbs not only the refractive index but also the birefringence, where $p \geq 0$ is an integer and m denotes the order number of the acoustic resonance [121, 129-132]. To illustrate the difference between the $R_{0,m}$ mode and $TR_{p,m}$ mode, the transverse profiles of the photo-elastic index variation induced by $R_{0,8}$ and $TR_{18,14}$ in a seven-core PCF fiber are given in Fig. 7-1 [133].

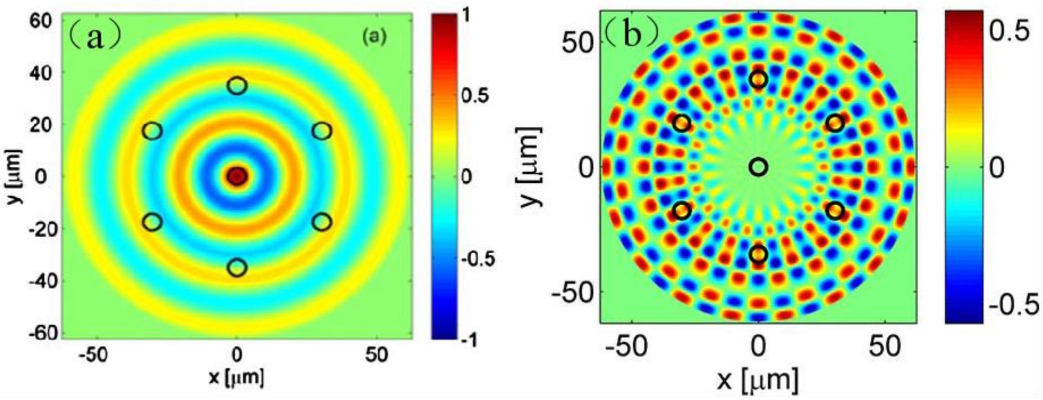

Figure 7- 1. Simulated transverse profiles of the photo-elastic index variation for $R_{0,8}$ and $TR_{18,14}$ in a seven-core PCF fiber. The cores of the fiber are labeled in black circles. This figure was taken from ref. [126].

The sensing application based on guided acoustic-wave Brillouin scattering has been investigated extensively. Existing fiber sensors for analysis of chemical species requires a spatial overlap between the analyzed liquids and the light in fibers, which needs to modify the fiber structures such as tapering the fibers to excite the cladding modes. Fiber sensors based on forward stimulated Brillouin scattering are proposed for the impedance sensing without any structural intervention. Firstly, Yair Antman, et al. proposes the idea of impedance measurement based on polarized guided acoustic-wave Brillouin scattering ($R_{0,m}$ modes) [134]. The acoustic reflectivity at the outer cladding boundary and the acoustic impedance of the surrounding medium are extracted from cavity lifetime measurements of multiple modes. Then Neisei Hayashi, et al. proposed the measurement of the acoustic impedance of external materials based on spectrum dependence of depolarized guided acoustic Brillouin scattering (TR$_{2,m}$ modes) [129]. The impedance is characterized by the variation of the linewidth and the shift of the central wavelength of TR$_{2,m}$ modes. A method of absolute diameter characterization of micrometer-scale fiber tapers has also been proposed based on the torsional-radial acoustic mode (TR$_{2,m}$ modes) whose spectrum structure reveals the sample diameter and its non-uniformity [135].

7.2 Theory model for guided acoustic-wave Brillouin scattering

7.2.1 Radial Acoustic Modes (*$R_{0,m}$*) in Fibers

The radial modes, denoted as $R_{0,m}$, with the radially symmetric acoustic field distribution are one of the groups of guided acoustic modes. The cut-off frequency of modes $R_{0,m}$ is given by [121]

$$f_{0,m} = \left[V_d / \left(2\pi a\right)\right]\xi_m ,$$

where V_d is the acoustic velocities of the longitudinal wave, a is the radius of the fiber cladding, and ξ_m is the *m*th order solution to the equation

$$\left(1-\alpha^2\right)J_0\left(\xi\right)=\alpha^2 J_2\left(\xi\right),$$

where $\alpha= V_s/V_d$ with V_s being the acoustic velocity of the shear wave in fibers and J_0 and J_2 are the zero- and second-order Bessel functions

For example, in standard silica fibers, V_s =3740 *m/s*, V_d =5996 *m/s* [136] and a =62.5 µm, the calculated first 8 frequencies are 30.51 MHz, 82.04 MHz, 130.72 MHz, 179.00 MHz, 227.15 MHz, 275.23 MHz, 323.27 MHz, and 371.30 MHz, respectively.

7.2.2 Torsional-radial acoustic mode (T$R_{2,m}$) in Fibers

The torsional-radial acoustic mode (T$R_{2,m}$) perturbs not only the refractive index but also the birefringence in the fibers. The central frequency of the m^{th} order acoustic mode is given by [121]

$$f_m = V_s \xi_m / (2\pi a)$$

where V_s is the acoustic velocities of the shear wave, a is the radius of the fiber cladding, and ξ_m is the mth order solution to the following equation [121]:

$$\begin{vmatrix} \left(3-\frac{\xi_m^2}{2}\right) J_2(\alpha\xi_m) & \left(6-\frac{\xi_m^2}{2}\right) J_2(\xi_m) - 3\xi_m J_3(\xi_m) \\ J_2(\alpha\xi_m) - \alpha\xi_m J_3(\alpha\xi_m) & \left(2-\frac{\xi_m^2}{2}\right) J_2(\xi_m) + \xi_m J_3(\xi_m) \end{vmatrix} = 0$$

where $\alpha = V_s/V_d$ with V_d being the acoustic velocity of the longitudinal wave in fibers and J_2 and J_3 are the second- and third-order Bessel functions, respectively. For example, the central frequency of the $TR_{2,5}$ mode is 107.7 MHz.

7.3 Experimental setup and results

7.3.1 Experimental setup and results for observing ringing traces induced by Radial Acoustic Modes ($R_{0,m}$) in Fibers

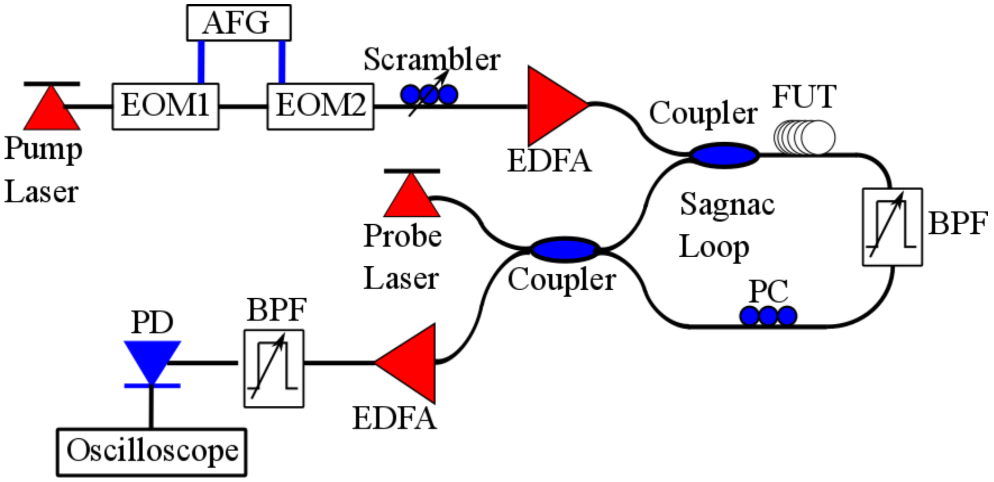

Figure 7- 2. Schematic of the experimental setup for observing the ringing traces induced by radial guided acoustic mode. AFG, arbitrary function generator; EOM, electro-optic modulator; EDFA, erbium-doped fiber amplifier; FUT, fiber under test; BPF, bandpass filter; PC, polarization controller; PD, photodetector.

A schematic of the experimental setup for observing the ringing traces induced by radial guided acoustic mode is presented in Figure 7-2. Light from the pump laser at a wavelength of 1550 nm was modulated by two electro-optic modulators (EOM) driven by an arbitrary function generator to get pulses with 4 ns duration. The pump pulses are amplified by the erbium-doped fiber amplifier (EDFA) and launched into the fiber under test. The peak power of the pulses is up to 40 dBm. The polarization scrambler was utilized to suppress the torsional-radial acoustic modes ($TR_{2,m}$).

The fiber under test was placed in a Sagnac loop. The probe light at a wavelength of 1556 nm was launched into the Sagnac loop in both directions. Following the propagation of the pump pulses, the refractive index change induced by acoustic vibration will introduce the changes in the phase delay of the clockwise-propagating probe light, and much smaller changes in the phase delay of the anticlockwise-propagating probe light. The bandpass filter in the Sagnac loop blocks the pump light but allows the probe light to propagate in both directions. The output signal was detected by a photodetector and recorded in the oscilloscope.

Firstly, a 15-m-long single-mode fiber with its polymer coating removed was tested in the Sagnac loop. Figure 7-3(a) shows the signal trace $V(t)$ as a function of time t, when the fiber under test was exposed in the air. An acoustic impulse was stimulated by a pump pulse and radiates outward from the core to the out boundary of the cladding. Part of the acoustic wave is reflected back towards the core due to the impedance mismatch between the cladding and the air and the other part is transmitted to the air. The acoustic impulses bound from the core to the boundary of cladding every ~21 ns that is determined by the cladding diameter and the acoustic velocity in the cladding. As presented in Fig. 7-3(b), the power density of the measured trace is calculated. The multiple resonances agree with the calculated frequencies in the theory part shown in 7.2.1.

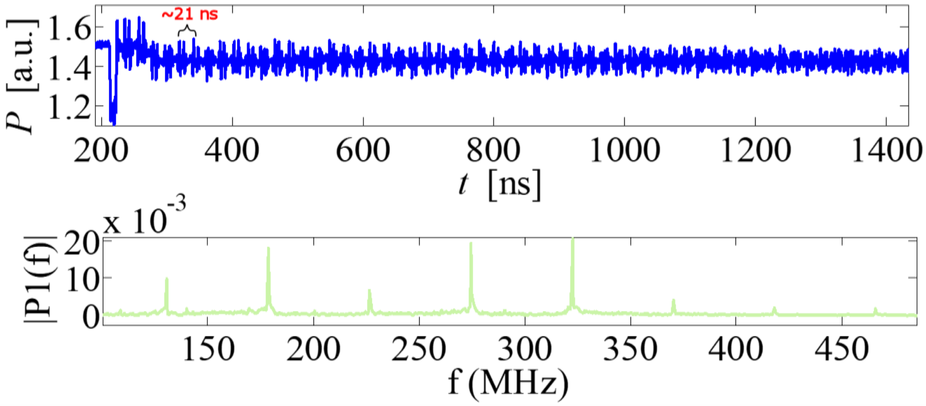

Figure 7- 3. (a) Measured power of the signal as a function of time t in the oscilloscope. The fiber under test was 15-m-long single mode fiber with the polymer coating removed. (b) Power spectrum density of the measured signal trace.

Then a 10-cm-long single-core As_2Se_3-PMMA taper with As_2Se_3 core diameter of 3 µm and PMMA diameter of 169.5 µm was placed in the Sagnac loop as FUT. Figure 7-4 shows the measured power of the signal as a function of time *t* in the oscilloscope. Wavelength conversion effect will be induced while a pump pulse and a CW probe light propagate in a Sagnac loop due to the Kerr effect. In our case, two pulses are observed because the duration of the pump pulse is larger than the length of single-core As_2Se_3-PMMA taper as the nonlinear medium. The echo period is about ~65 ns. Considering that the acoustic velocity in PMMA of 3800 m/s [137] and the diameter of PMMA, the experimental and calculated results are matched. There are two reasons for that only a few echoes appear in the trace: (1)

the As_2Se_3 core is not guaranteed in the center of the fiber; (2) acoustic loss is large due to the impedance mismatch between the As_2Se_3 core and PMMA cladding.

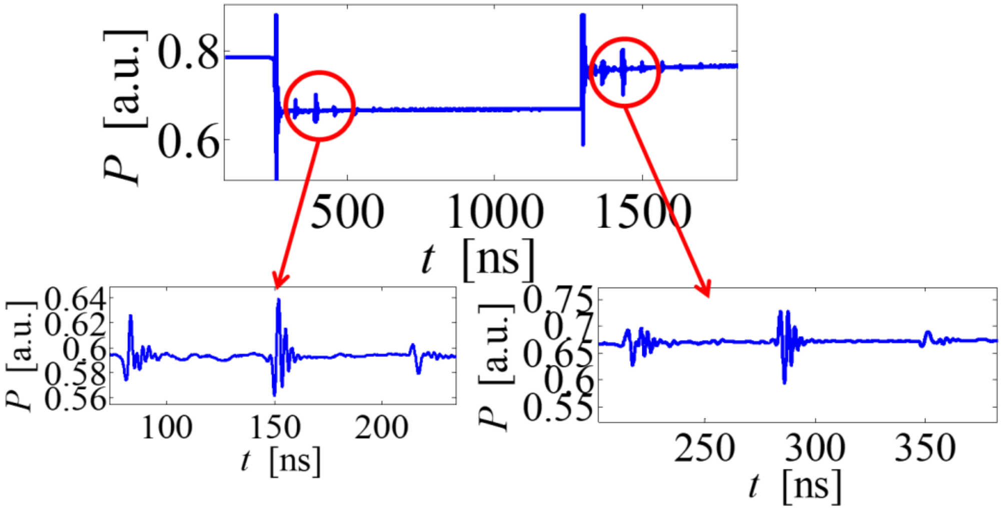

Figure 7- 4. Measured power of the signal as a function of time t in the oscilloscope. The fiber under test was 10-cm long As_2Se_3-PMMA taper.

7.3.2 Experimental setup and results for studying the Torsional-radial Acoustic Modes ($TR_{2,m}$) in Fibers

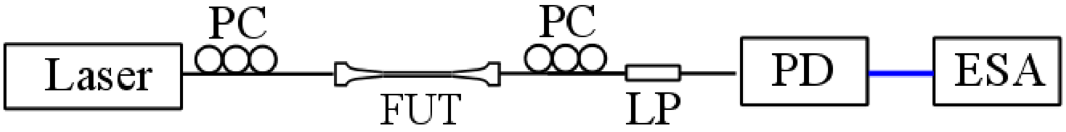

Figure 7- 5. Schematic of setup for observing depolarized guided acoustic wave Brillouin scattering. PC, polarization controller; LP, linear polarizer; PD, photodetector; ESA, electrical spectrum analyzer.

Figure 7-5 shows the experimental setup for observing depolarized guided acoustic wave Brillouin scattering. The light source is a fiber laser operating at 1550 nm, which is launched into the FUT. The beat signal of the GAWBS light and the pump light emitted out of the fiber is detected by a photodetector placed after an analyzer. The polarization of the input and output light is adjusted by the two polarization controllers (PC) and a polarizer so as to maximize the resonance peak monitored on a spectrum analyzer.

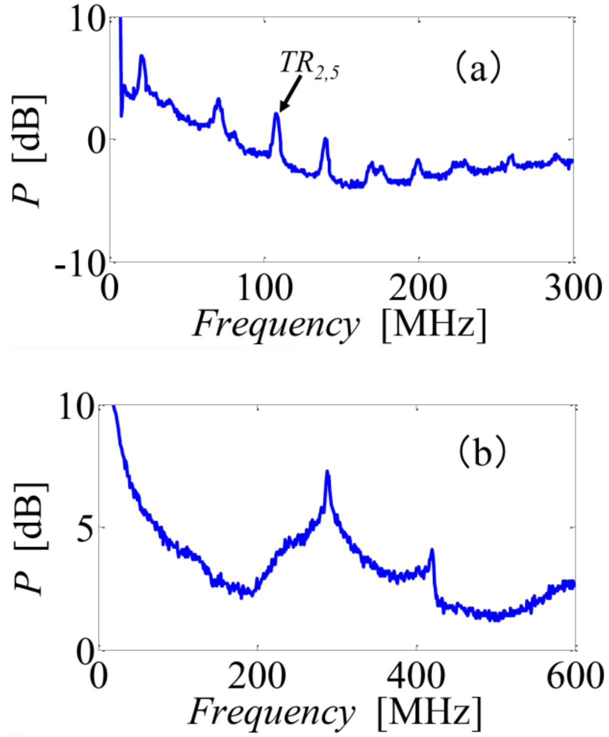

Figure 7- 6. Measured depolarized GAWBS spectra of (a) 1.5-km-long single-mode fiber and (b) 60-cm-long As_2Se_3-PMMA fiber with As_2Se_3diameter of 1.06 micron.

A 1.5-km-long single mode fiber and a 60-cm-long As_2Se_3-PMMA taper with As_2Se_3 diameter of 1.06 µm and PMMA cladding diameter of 60 µm are tested, respectively, and the results are shown in Fig. 7-6. A clear peak was observed at 108.2 MHz in Fig. 7-6(a) corresponding to the $TR_{2,5}$ mode, which agrees with the theoretical value of 107.7 MHz. Figure 7-6(b) shows the GAWBS spectrum of the As_2Se_3-PMMA taper with a peak wavelength of ~292 MHz.

7.4 Conclusion

In this chapter, we review the recent work about the guided acoustic-wave Brillouin scattering (GAWBS) and its sensing applications. The GAWBS by the radial and torsional-radial guided acoustic modes ($R_{0,m}$ and $TR_{2,m}$) of silica fibers and tapered single-core As_2Se_3-PMMA fibers is investigated experimentally and the preliminary results are presented. Based on the measured ringing traces for radial and torsional-radial guided acoustic modes $R_{0,m}$ and torsional-radial guided acoustic modes $TR_{2,m}$, a new approach for humidity sensing can be achieved due to the impedance changed in the PMMA cladding induced by the water absorption property of the PMMA material.

Chapter 8 Summary and future work

8.1 Summary

This thesis introduced the fabrication procedure of tapered dual-core As_2Se_3-PMMA fibers and extended the applications of the As_2Se_3-PMMA taper to the high sensitivity temperature and strain sensing and the nonlinear effects such as modulation instability and guided acoustic wave Brillouin scattering. The background of the chalcogenide fiber, PMMA material, dual-core structure and tapering technique and procedure is reviewed and discussed. A theoretical model for temperature and strain measurement is given based on a dual-core As_2Se_3-PMMA taper. Below is the summary of my thesis:

(1) We propose and demonstrate an approach for high-sensitivity simultaneous temperature and strain measurement in a dual-core As_2Se_3-PMMA taper utilizing the intrinsic material properties of the As_2Se_3 and PMMA with an As_2Se_3 core diameter of 0.55 μm. High measurement sensitivity is achieved by combining the large thermal-expansion coefficient of the PMMA cladding, the low stiffness of the micron diameter As_2Se_3 core, and the large difference between the refractive-indices of As_2Se_3 and PMMA. High measurement sensitivities of -115 pm/ºC, -4.21 pm/με are measured from the transmission spectrum of one principal polarization axis of the dual-core fiber, -35.5 pm/ºC and -3.16 pm/με are obtained from the transmission spectrum of the second polarization axis of the dual-core fiber.

(2) A temperature-insensitive strain sensor is proposed and demonstrated based on a dual-core As_2Se_3-PMMA taper utilizing the thermal forces on the As_2Se_3 cores by the PMMA cladding with an As_2Se_3 core diameter of 0.61 μm and a PMMA cladding diameter of 34.4 μm. Longitudinal and transverse forces on the As_2Se_3 cores are induced by thermal

expansion/contraction of the PMMA cladding due to an order of magnitude difference between the thermal expansion coefficients of As_2Se_3 and PMMA. At an optimal PMMA layer thickness, the wavelength shift caused by the thermally-induced forces on the refractive-index of the dual-core fiber cores counterbalances that caused by the thermally-induced fiber length variation leading to temperature insensitive transmission. Temperature-insensitive strain measurement over a temperature range from 30 °C to 40 °C is demonstrated in a dual-core As_2Se_3-PMMA fiber. Thermally-induced forces in hybrid fibers open the path towards the realization of novel sensors and devices that are immune to temperature fluctuations.

(3) We report for the first time that transmission of optical pulses centered at a wavelength of 1550 nm through a tapered dual-core As_2Se_3-PMMA fiber inscribes an antisymmetric long-period grating. The pulse power is equally divided between even and odd modes that superpose along the dual-core fiber to form an antisymmetric intensity distribution. A permanent refractive-index change that matches the antisymmetric intensity distribution is inscribed due to photosensitivity at the pulse central wavelength. The evolution of the transmission spectrum of the dual-core fiber is experimentally measured as the accumulated time that the fiber is exposed to the pulse is increased. A theoretical model of an antisymmetric long-period grating in a dual-core fiber computationally reproduces the experimentally observed evolution of the transmission spectrum. Experimental results indicate that antisymmetric long-period gratings induce effective group-velocity matching between the even and odd modes of the dual-core fiber, and reveal for the first time that long-period gratings can lead to slow light propagation velocities.

(4) We investigated two approaches for sensitivity enhancement of temperature and strain measurement. Firstly, we demonstrate an approach for sensitivity enhancement of temperature and strain measurement in a dual-core As_2Se_3-PMMA taper with a large As_2Se_3 core diameter of 2.5 μm by reducing the value of $\partial\phi_d(\lambda)/\partial\lambda$ and increasing thermal forces. The variation of the difference between phases of the two modes with respect to wavelength ($\partial\phi_d(\lambda)/\partial\lambda$) becomes small as the As_2Se_3 core diameter increases, and consequently, thermally-induced and strain-induced change of the difference between phases of the two modes $\phi_d(\lambda)$ leads to a large wavelength shift indicating enhancement of the temperature and strain measurement sensitivity. Furthermore, thermally-induced longitudinal and transverse forces on the As_2Se_3 cores further enhance the temperature measurement sensitivity. High sensitivities of 436 pm/°C, -6.23 pm/μ**ε** and 572 pm/°C and -3.63 pm/μ**ε** from the transmission spectra of axis-1 and axis-2 in the dual-core As_2Se_3-PMMA taper are obtained. Then, the second approach is that based on effective group-velocity matching between the even and odd modes of a dual-core As_2Se_3-PMMA taper on which an antisymmetric long-period grating is inscribed, we propose and demonstrate an approach for temperature-sensitivity enhancement by a factor of 4.0. The transmission of optical pulses in the dual-core As_2Se_3-PMMA taper inscribes the antisymmetric long-period grating that causes the electric fields to couple back and forth between the even and odd modes leading to effective group-velocity matching between the two modes. The variation of the difference between phases of the two modes with respect to wavelength tends to 0 ($\partial\phi_d(\lambda)/\partial\lambda\rightarrow0$) near the resonance wavelength of the grating due to the effective group-velocity matching between the two modes, and consequently, thermally-induced change of the difference between phases of the two modes $\phi_d(\lambda)$ leads to a large wavelength shift indicating enhancement of the temperature measurement sensitivity. The sensitivity of temperature measurement in the

wavelength range with effective group velocity matching is enhanced by a factor of 4.0 in comparison with that in the wavelength range that does not have effective group velocity matching. The effective group-velocity matching between modes in fibers opens the path towards the realization of novel high-sensitivity sensors for temperature and strain measurement.

(5) For the nonlinear effects, firstly, we report the first observation of modulation-instability in the normal-dispersion regime of a dual-core As_2Se_3-PMMA fiber. The modulation instability spectrum shows multiple peaks arising from the strong wavelength dependence of the coupling coefficient. Modulation instability in dual-core fibers can be used for enhanced parametric amplification, broadly tunable lasers, and efficient entangled photon generations. Then we review the recent work about the forward stimulated Brillouin scattering and its sensing applications. The forward stimulated Brillouin scattering by the radial guided acoustic modes of silica fibers and tapered dual-core As_2Se_3-PMMA fibers is investigated experimentally and the preliminary results are presented. Sensing applications such as the acoustic impedance of the surrounding medium and taper dimension characterization can be achieved based on cavity lifetime measurements of multiple modes due to the acoustic reflectivity at the outer cladding boundary.

8.2 Future work

Tapered dual-core chalcogenide-polymer tapers composed of two As_2Se_3 cores and a polymethyl methacrylate (PMMA) cladding are promising platforms for sensing and nonlinear applications. And chalcogenide glass has a wide transparency in the MIR wavelength range. The summarized work in this thesis only introduces part of the applications of the tapered As_2Se_3-PMMA fibers. Future work on the tapered chalcogenide-

PMMA fibers may focus on three parameter sensing (temperature, strain and humidity sensing), nonlinear effects (stimulated Brillouin scattering, forward stimulated Brillouin scattering, Modulation instability) and slow light.

8.2.1 Simultaneous temperature, strain, and humidity sensing

We introduced many techniques for temperature and strain measurement based on dual-core As_2Se_3-PMMA tapers in this thesis. The PMMA coating provides high robustness, high flexibility and ease of handing, which has great advantages over the silica fibers [138, 139]. However, the water-absorption property of the PMMA is an essential factor people should take care of when using PMMA materials in fiber sensing, which will lead to a swelling of the optical fibers and also an increase of the refractive index [140]. Simultaneous temperature, strain and humidity sensors have not been achieved, although simultaneous measurement of these three parameters is critical in many applications, such as air-conditioning of office buildings and greenhouse industries. To simultaneous measure temperature, strain and humidity, we propose two potential methods.

The first approach is that simultaneous temperature, strain and humidity sensing based on a dual-core As_2Se_3-PMMA taper. As illustrated in Chapter 2, a dual-core fiber sustains two main modes, an even mode and an odd mode. The geometrical structure of a dual-core fiber has two distinct axes of symmetry resulting in strong birefringence with two distinct principal polarization axes. When light is launched at the input of core-1 of the dual-core fiber, the even mode and the odd mode are excited equally. For each principal axis, the output radiation pattern is a superposition of the fields of the even and odd modes. The intensity at the output of core-1 is given by $I=0.5|a_e|^2+0.5|a_o|^2+|a_e||a_o|\cos[\phi_d\,(\lambda,T)]$, where $\phi_d\,(\lambda,T)= 2\pi\Delta n_{eff}L_w/\lambda+\theta_e-\theta_o$, $\Delta n_{eff} = n^e_{eff}-n^o_{eff}$, a_i is the complex amplitude with i being

e for the even-mode or o for the odd-mode, θ_i is the phase of a_i, and L_w is the length of the dual-core taper waist. Due to the wavelength dependence of the phase difference ϕ_d, troughs are observed in the transmission spectrum of a tapered dual-core fiber when the difference between the phases of the even and odd modes satisfies the condition $\phi_d\,(\lambda,T) = (2m+1)\,\pi$, where m is an integer. Changes in the temperature, strain and humidity of the fiber taper, respectively, lead to change in the wavelength shifts of both axes and also the oscillation periods of the transmission spectrum of both axes. The principal polarization axes of the dual-core fiber have different values of $\Delta\lambda$ and oscillation periods, which lead to decorrelated temperature, strain and humidity measurement sensitivities for these two axes.

The second approach is simultaneous temperature, strain and humidity sensing based on a dual-core As_2Se_3-PMMA taper with an antisymmetric long-period grating. The transmission of optical pulses in the dual-core As_2Se_3-PMMA taper inscribes the antisymmetric long-period grating that causes the electric fields to couple back and forth between the even and odd modes leading to effective group-velocity matching between the two modes. The values of variation of the difference between phases of the two modes $\phi_d(\lambda)$ with respect to wavelength ($\partial\phi_d(\lambda)/\partial\lambda$) are different for different troughs near the resonance wavelength of the grating due to effective group-velocity matching between the two modes, and consequently, the temperature, strain and humidity induce different wavelength shifts enabling simultaneous multiple-parameter sensing.

8.2.2 Nonlinear effect

Chalcogenide glass is an excellent nonlinear medium with the intrinsic material nonlinearity 1000 times larger than that of the widespread silica glass. However, due to the high photosensitivity of the As_2Se_3 glass, a refractive index change is induced and proportional to the intensity; consequently, gratings are inscribed in the As_2Se_3-PMMA fiber when pulses with high-peak power propagate along the fiber. For example, the inscription of fiber Bragg gratings in tapered single-core As_2Se_3-PMMA fibers has been reported utilizing photosensitivity of As_2Se_3 glass to optical signals at 1550 nm [39]. We have also reported that the propagation of optical pulses with high peak-power in a tapered dual-core As_2Se_3-PMMA fiber leads to the inscription of an antisymmetric long-period grating at 1550 nm [86]. This limits the applications of tapered As_2Se_3-PMMA fibers in the nonlinear effects because high power or high peak power is required to achieve most of the nonlinear effects. To solve this problem, As_2S_3 instead of As_2Se_3 is a potential core material due to its low photosensitivity and comparable nonlinearity.

8.2.3 Slow light

As illustrated in chapter 5, fast variation of $\Delta\varphi$ at the resonance wavelength of λ_r implies that phase of even mode φ_e and phase of odd mode φ_o have fast variations with wavelength indicating the potential for inducing a slow light propagation velocity. This is the first time to our knowledge that long-period gratings are shown to have the potential for achieving slow light. This slow light feature can be utilized for the implementation of highly sensitive devices for the measurement of temperature and refractive-index change of a liquid solution. It will be exciting to demonstrate it experimentally.

Curriculum Vitae

Full name	Song Gao
Education	Ph.D. in Physics (Sep.2014-Aug.2018) Department of Physics University of Ottawa, Ottawa, Canada Supervisors: Prof. Xiaoyi Bao
	M.Sc. (Sep.2011-Aug.2014) Department of Physics Beijing Jiaotong University, Beijing, China Supervisors: Prof. Xinzhi Sheng
	B.S. (Sep.2007-Jun.2011) College of Physics University of Jinan, Jinan, P. R. China

Publications

Journal Papers

- 1. **Song Gao**, C. Baker, L. Chen, X. Bao, "Temperature-sensitivity enhancement in a tapered dual-core As2Se3 -PMMA fiber with an antisymmetric long-period grating", Journal of Lightwave Technology, (Accepted 2018).
- 2. **Song Gao**, C. Baker, L. Chen, X. Bao, "High-sensitivity temperature and strain measurement in dual-core hybrid tapers", IEEE Photonics Technology Letters 30, no. 12, 1155 – 1158 (2018).
- 3. **Song Gao**, C. Baker, L. Chen, X. Bao, "Approach for temperature insensitive strain measurement using a dual-core As2Se3-PMMA taper", Opt. Lett. 43, 1523-1526 (2018).
- 4. **Song Gao**, C. Baker, L. Chen, X. Bao, "Simultaneous measurement of temperature and strain in a dual-core As2Se3 -PMMA taper", IEEE Photonics Technology Letters 30, no. 1, 79 – 82 (2018).
- 5. **Song Gao**, L. Zhang, Y. Xu, L. Chen, X. Bao, "High-speed truly physical random bit generation via Brillouin random fiber laser with non-uniform fibers", IEEE Photonics Technology Letters 29, no. 16, 1352-1355 (2017).
- 6. **Song Gao**, L. Zhang, Y. Xu, P. Lu, L. Chen, X. Bao, "Tapered fiber based Brillouin random fiber laser and its application for linewidth measurement", Opt Express, 24(25), 28353-28360 (2016).
- 7. Gao Song, Sheng Xin-Zhi, Feng Zhen, Wu Chong-Qing, Dong Hong-Hui. "Capability of single optical buffer loop implementing all-optical time slot

interchange based on nonlinear polarization rotation in semiconductor optical amplifier," Acta Phys. Sin, 63(8), 084205 (2014).

- 8. C. Baker, **Song Gao**, L. Chen, X. Bao, "Self-inscribed antisymmetric long-period grating in a dual-core As2Se3-PMMA fiber", Opt. Express 25, 12409-12414 (2017).
- 9. Y. Xu, **Song Gao**, P. Lu, S. Mihailov, L. Chen, X. Bao, "Low noise Brillouin random fiber laser with random grating based resonator," Opt Lett., 41(14), 3197-3200 (2016).
- 10. Y. Xu, L. Zhang, **Song Gao**, P. Lu, S. Mihailov, X. Bao, Highly sensitive fiber random-grating-based random laser sensor for ultrasound detection. Optics Letters, 42(7), 1353-1356 (2017).
- 11. L. Zhang, Y. Xu, **Song Gao**, B. Saxena, L. Chen, X. Bao, "Linearly polarized low-noise Brillouin random fiber laser", Optics Letters, 42(4), 739-742 (2017).
- 12. L. Zhang, Y. Xu, **Song Gao**, B. Saxena, L. Chen, X. Bao. Multi-wavelength coherent Brillouin random fiber laser with ultra-high optical signal-to-noise ratio. IEEE Journal of Selected Topics in Quantum Electronics (2017).
- 13. Y. Xu, P. Lu, **Song Gao**, D. Xiang, P. Lu, and X. Bao, "Optical fiber random grating based multi-parameter sensor", Optics Lett, 40 (23), 5514-5517 (2015).
- 14. D. Xiang, P. Lu, Y. Xu, **Song Gao**, L. Chen and X. Bao, "Truly random bit generation based on a novel random Brillouin fiber laser", Optics Letters, 40 (22), 5415-5418 (2015).
- 15. L. Zhang, C. Wang, Z. Li, Y. Xu, B. Saxena, **Song Gao**, L. Chen, X. Bao. High-efficiency Brillouin random fiber laser using all-polarization maintaining ring cavity. Optics Express, 25(10), 11306-11314 (2017).

Conference Papers

1. **Song Gao**, C. Baker, L. Chen, X. Bao, “Temperature-sensitivity enhancement in a tapered dual-core As2Se3-PMMA fiber with an antisymmetric long-period grating,” In CLEO, 2018.
2. Liang Zhang, Yuan Wang, Yanping Xu, **Song Gao**, Dapeng Zhou, Liang chen, xiaoyi bao, “Coherent Brillouin Random Fiber Laser for Application in Phase-sensitive Optical Time Domain Reflectometry ,” In CLEO, 2018.
3. Yanping Xu, Dao Xiang, Zhonghua Ou, **Song Gao**, and Xiaoyi Bao, “Novel bi-pumped Brillouin random fiber laser and its applications,” 2015, Schawlow-Townes Symposium: Poster Session, Ottawa, Canada.
4. Liang Zhang, Yanping Xu, **Song Gao**, Bhavaye Saxena, Liang Chen, and Xiaoyi Bao, "Multi-wavelength Coherent Brillouin Random Fiber Laser with High Optical Signal-to-Noise Ratio," 2017, Conference on Lasers and Electro-Optics, San Jose, California, USA.
5. Baker, Chams, **Song Gao**, Liang Chen, and Xiaoyi Bao. "Pulse-induced permanent group-velocity matching in a dual-core As 2 Se 3/PMMA fiber." In CLEO: Science and Innovations, pp. SW4O-3. Optical Society of America, 2017.
6. Yanping Xu, Dao Xiang, Zhonghua Ou, **Song Gao**, and Xiaoyi Bao, “Novel bi-pumped Brillouin random fiber laser and its applications,” 2015, Schawlow-Townes Symposium: Poster Session, Ottawa, Canada.

Bibliography

1. Humbach, O., H. Fabian, U. Grzesik, U. Haken, and W. Heitmann, *Analysis of OH absorption bands in synthetic silica.* Journal of non-crystalline solids, 1996. **203**: p. 19-26.

2. Kitamura, R., L. Pilon, and M. Jonasz, *Optical constants of silica glass from extreme ultraviolet to far infrared at near room temperature.* Applied optics, 2007. **46**(33): p. 8118-8133.

3. Yu, F., W.J. Wadsworth, and J.C. Knight, *Low loss silica hollow core fibers for 3–4 μm spectral region.* Optics express, 2012. **20**(10): p. 11153-11158.

4. *CorActive_Inc, Amorphous_material_Inc*. Available from: http://coractive.com/fileadmin/documents_publics/boutique/mid-ir-fibers/ir-fibers/Infrared_Products_Brochure_-_BR0001r1.3.pdf.

5. Sanghera, J.S., L.B. Shaw, and I.D. Aggarwal, *Applications of chalcogenide glass optical fibers.* Comptes Rendus Chimie, 2002. **5**(12): p. 873-883.

6. Sanghera, J., I. Aggarwal, L. Shaw, L. Busse, P. Thielen, V. Nguyen, P. Pureza, S. Bayya, and F. Kung, *Applications of chalcogenide glass optical fibers at NRL.* Journal of Optoelectronics and Advanced Materials, 2001. **3**(3): p. 627-640.

7. Letokhov, V., *Generation of light by a scattering medium with negative resonance absorption.* Soviet Journal of Experimental and Theoretical Physics, 1968. **26**: p. 835-840.

8. Li, L., A. Al-Kadry, N. Abdukerim, and M. Rochette, *Design, fabrication and characterization of PC, COP and PMMA-cladded As 2 Se 3 microwires.* Optical Materials Express, 2016. **6**(3): p. 912-921.

9. Slusher, R.E., G. Lenz, J. Hodelin, J. Sanghera, L.B. Shaw, and I.D. Aggarwal, *Large Raman gain and nonlinear phase shifts in high-purity As 2 Se 3 chalcogenide fibers.* JOSA B, 2004. **21**(6): p. 1146-1155.

10. Agrawal, G.P., *Nonlinear fiber optics*, in *Nonlinear Science at the Dawn of the 21st Century*. 2000, Springer. p. 195-211.

11. Asobe, M., T. Kanamori, K. Naganuma, H. Itoh, and T. Kaino, *Third‐order nonlinear spectroscopy in As2S3 chalcogenide glass fibers.* Journal of applied physics, 1995. **77**(11): p. 5518-5523.

12. Fu, L., M. Rochette, V. Ta'eed, D. Moss, and B. Eggleton, *Investigation of self-phase modulation based optical regeneration in single mode As 2 Se 3 chalcogenide glass*

fiber. Optics Express, 2005. **13**(19): p. 7637-7644.

13. Smektala, F., C. Quemard, V. Couderc, and A. Barthélémy, *Non-linear optical properties of chalcogenide glasses measured by Z-scan.* Journal of non-crystalline solids, 2000. **274**(1-3): p. 232-237.

14. Smektala, F., C. Quemard, L. Leneindre, J. Lucas, A. Barthélémy, and C. De Angelis, *Chalcogenide glasses with large non-linear refractive indices.* Journal of non-crystalline solids, 1998. **239**(1-3): p. 139-142.

15. Dai, S., Y. Wang, X. Peng, P. Zhang, X. Wang, and Y. Xu, *A Review of Mid-Infrared Supercontinuum Generation in Chalcogenide Glass Fibers.* Applied Sciences (2076-3417), 2018. **8**(5).

16. Asobe, M., T. Kanamori, and K.i. Kubodera, *Applications of highly nonlinear chalcogenide glass fibers in ultrafast all-optical switches.* IEEE Journal of Quantum Electronics, 1993. **29**(8): p. 2325-2333.

17. Sanghera, J.S., L.B. Shaw, and I.D. Aggarwal, *Chalcogenide glass-fiber-based mid-IR sources and applications.* IEEE Journal of selected topics in quantum electronics, 2009. **15**(1): p. 114-119.

18. Abedin, K.S., *Observation of strong stimulated Brillouin scattering in single-mode As 2 Se 3 chalcogenide fiber.* Optics Express, 2005. **13**(25): p. 10266-10271.

19. Song, K.Y., K.S. Abedin, K. Hotate, M.G. Herráez, and L. Thévenaz, *Highly efficient Brillouin slow and fast light using As2Se3 chalcogenide fiber.* Optics Express, 2006. **14**(13): p. 5860-5865.

20. Yaman, M., H.E. Kondakci, and M. Bayindir, *Large and dynamical tuning of a chalcogenide Fabry-Perot cavity mode by temperature modulation.* Optics express, 2010. **18**(3): p. 3168-3173.

21. Li, X., S. Lin, J. Liang, Y. Zhang, H. Oigawa, and T. Ueda, *Fiber-optic temperature sensor based on difference of thermal expansion coefficient between fused silica and metallic materials.* IEEE Photonics Journal, 2012. **4**(1): p. 155-162.

22. Myer, E., *Plastics failure guide: cause and prevention.* New York, 1996.

23. Beadie, G., M. Brindza, R.A. Flynn, A. Rosenberg, and J.S. Shirk, *Refractive index measurements of poly (methyl methacrylate)(PMMA) from 0.4–1.6 μm.* Applied optics, 2015. **54**(31): p. F139-F143.

24. N'Diaye, M., F. Pascaretti-Grizon, P. Massin, M.F. Baslé, and D. Chappard, *Water absorption of poly (methyl methacrylate) measured by vertical interference microscopy.* Langmuir, 2012. **28**(31): p. 11609-11614.

25. Li, X., Z. Cao, Q. Shen, and Y. Yang, *Influence of dopant concentration on thermo-optic*

properties of PMMA composite. Materials Letters, 2006. **60**(9-10): p. 1238-1241.

26. Lee, B.H., J.B. Eom, J. Kim, D.S. Moon, U.-C. Paek, and G.-H. Yang, *Photonic crystal fiber coupler.* Optics Letters, 2002. **27**(10): p. 812-814.

27. Szostkiewicz, L., M. Napierala, A. Ziolowicz, A. Pytel, T. Tenderenda, and T. Nasilowski, *Cross talk analysis in multicore optical fibers by supermode theory.* Optics letters, 2016. **41**(16): p. 3759-3762.

28. Richardson, D., J. Fini, and L. Nelson, *Space-division multiplexing in optical fibres.* Nature Photonics, 2013. **7**(5): p. 354.

29. Antonio-Lopez, J.E., Z.S. Eznaveh, P. LiKamWa, A. Schülzgen, and R. Amezcua-Correa, *Multicore fiber sensor for high-temperature applications up to 1000 C.* Optics letters, 2014. **39**(15): p. 4309-4312.

30. Moore, J.P. and M.D. Rogge, *Shape sensing using multi-core fiber optic cable and parametric curve solutions.* Optics express, 2012. **20**(3): p. 2967-2973.

31. Van Newkirk, A., J.E. Antonio-Lopez, G. Salceda-Delgado, M.U. Piracha, R. Amezcua-Correa, and A. Schülzgen, *Multicore fiber sensors for simultaneous measurement of force and temperature.* IEEE Photonics Technology Letters, 2015. **27**(14): p. 1523-1526.

32. Mothe, N. and P. Di Bin, *Numerical analysis of directional coupling in dual-core microstructured optical fibers.* Optics express, 2009. **17**(18): p. 15778-15789.

33. Dumais, P., A. Villeneuve, P. Wigley, F. Gonthier, S. Lacroix, G. Stegeman, and J. Bures, *Enhanced self-phase modulation in tapered fibers.* Optics letters, 1993. **18**(23): p. 1996-1998.

34. Kenny, R., T. Birks, and K. Oakley, *Control of optical fibre taper shape.* Electronics letters, 1991. **27**(18): p. 1654-1656.

35. Baker, C. and M. Rochette, *Highly nonlinear hybrid AsSe-PMMA microtapers.* Optics Express, 2010. **18**(12): p. 12391-12398.

36. Ahmad, R. and M. Rochette, *Chalcogenide optical parametric oscillator.* Optics express, 2012. **20**(9): p. 10095-10099.

37. Ahmad, R. and M. Rochette, *Raman lasing in a chalcogenide microwire-based Fabry–Perot cavity.* Optics letters, 2012. **37**(21): p. 4549-4551.

38. Ahmad, R. and M. Rochette, *High efficiency and ultra broadband optical parametric four-wave mixing in chalcogenide-PMMA hybrid microwires.* Optics express, 2012. **20**(9): p. 9572-9580.

39. Ahmad, R. and M. Rochette, *Photosensitivity at 1550 nm and Bragg grating inscription*

in As2Se3 chalcogenide microwires. Applied Physics Letters, 2011. **99**(6): p. 061109.

40. Al-Kadry, A., M. El Amraoui, Y. Messaddeq, and M. Rochette, *Mode-locked fiber laser based on chalcogenide microwires.* Optics letters, 2015. **40**(18): p. 4309-4312.

41. Beugnot, J.-C., R. Ahmad, M. Rochette, V. Laude, H. Maillotte, and T. Sylvestre, *Reduction and control of stimulated Brillouin scattering in polymer-coated chalcogenide optical microwires.* Optics letters, 2014. **39**(3): p. 482-485.

42. Godin, T., Y. Combes, R. Ahmad, M. Rochette, T. Sylvestre, and J.M. Dudley, *Far-detuned mid-infrared frequency conversion via normal dispersion modulation instability in chalcogenide microwires.* Optics letters, 2014. **39**(7): p. 1885-1888.

43. Yang, R., Y.-S. Yu, Y. Xue, C. Chen, Q.-D. Chen, and H.-B. Sun, *Single S-tapered fiber Mach–Zehnder interferometers.* Optics letters, 2011. **36**(23): p. 4482-4484.

44. Lu, P., L. Men, K. Sooley, and Q. Chen, *Tapered fiber Mach–Zehnder interferometer for simultaneous measurement of refractive index and temperature.* Applied Physics Letters, 2009. **94**(13): p. 131110.

45. Tripathi, S.M., A. Kumar, R.K. Varshney, Y.B.P. Kumar, E. Marin, and J.-P. Meunier, *Strain and temperature sensing characteristics of single-mode–multimode–single-mode structures.* Journal of Lightwave Technology, 2009. **27**(13): p. 2348-2356.

46. Wu, D., T. Zhu, M. Deng, D.-W. Duan, L.-L. Shi, J. Yao, and Y.-J. Rao, *Refractive index sensing based on Mach–Zehnder interferometer formed by three cascaded single-mode fiber tapers.* Applied optics, 2011. **50**(11): p. 1548-1553.

47. Murphy, R.P., S.W. James, and R.P. Tatam, *Multiplexing of fiber-optic long-period grating-based interferometric sensors.* Journal of Lightwave Technology, 2007. **25**(3): p. 825-829.

48. Yu, X., P. Shum, and X. Dong, *Photonic‐crystal‐fiber‐based Mach‐Zehnder interferometer using long‐period gratings.* Microwave and optical technology letters, 2006. **48**(7): p. 1379-1383.

49. Lacroix, S., F. Gonthier, and J. Bures, *Modeling of symmetric 2× 2 fused-fiber couplers.* Applied Optics, 1994. **33**(36): p. 8361-8369.

50. Bricheno, T. and V. Baker, *All-fibre polarisation splitter/combiner.* Electronics Letters, 1985. **21**(6): p. 251-252.

51. Sanghera, J. and I. Aggarwal, *Active and passive chalcogenide glass optical fibers for IR applications: a review.* Journal of Non-Crystalline Solids, 1999. **256**: p. 6-16.

52. Wade, S.A., S.F. Collins, and G.W. Baxter, *Fluorescence intensity ratio technique for optical fiber point temperature sensing.* Journal of Applied physics, 2003. **94**(8): p. 4743-4756.

53. Bao, X., D.J. Webb, and D.A. Jackson, *32-km distributed temperature sensor based on Brillouin loss in an optical fiber.* Optics letters, 1993. **18**(18): p. 1561-1563.

54. Kersey, A.D., T. Berkoff, and W. Morey, *Multiplexed fiber Bragg grating strain-sensor system with a fiber Fabry–Perot wavelength filter.* Optics letters, 1993. **18**(16): p. 1370-1372.

55. Takeo, T. and H. Hattori, *Optical fiber sensor for measuring refractive index.* Japanese Journal of Applied Physics, 1982. **21**(10R): p. 1509.

56. Yuan, W., G.E. Town, and O. Bang, *Refractive index sensing in an all-solid twin-core photonic bandgap fiber.* IEEE Sensors Journal, 2010. **10**(7): p. 1192-1199.

57. Li, H.-N., D.-S. Li, and G.-B. Song, *Recent applications of fiber optic sensors to health monitoring in civil engineering.* Engineering structures, 2004. **26**(11): p. 1647-1657.

58. Cheng, S.-F. and L.-K. Chau, *Colloidal gold-modified optical fiber for chemical and biochemical sensing.* Analytical chemistry, 2003. **75**(1): p. 16-21.

59. Markos, C., W. Yuan, K. Vlachos, G.E. Town, and O. Bang, *Label-free biosensing with high sensitivity in dual-core microstructured polymer optical fibers.* Optics express, 2011. **19**(8): p. 7790-7798.

60. Frazao, O., L. Marques, S. Santos, J.M. Baptista, and J. Santos, *Simultaneous measurement for strain and temperature based on a long-period grating combined with a high-birefringence fiber loop mirror.* IEEE Photonics Technology Letters, 2006. **18**(22): p. 2407-2409.

61. Guan, B.-O., H.-Y. Tam, X.-M. Tao, and X.-Y. Dong, *Simultaneous strain and temperature measurement using a superstructure fiber Bragg grating.* IEEE Photonics Technology Letters, 2000. **12**(6): p. 675-677.

62. Shao, L.-Y., A. Laronche, M. Smietana, P. Mikulic, W.J. Bock, and J. Albert, *Highly sensitive bend sensor with hybrid long-period and tilted fiber Bragg grating.* Optics Communications, 2010. **283**(13): p. 2690-2694.

63. Chen, X., K. Zhou, L. Zhang, and I. Bennion, *Simultaneous measurement of temperature and external refractive index by use of a hybrid grating in D fiber with enhanced sensitivity by HF etching.* Applied optics, 2005. **44**(2): p. 178-182.

64. Liu, Y. and L. Wei, *Low-cost high-sensitivity strain and temperature sensing using graded-index multimode fibers.* Applied optics, 2007. **46**(13): p. 2516-2519.

65. Zhou, D.-P., L. Wei, W.-K. Liu, Y. Liu, and J.W. Lit, *Simultaneous measurement for strain and temperature using fiber Bragg gratings and multimode fibers.* Applied optics, 2008. **47**(10): p. 1668-1672.

66. Kang, Z., X. Wen, C. Li, J. Sun, J. Wang, and S. Jian, *Up-taper-based Mach–Zehnder*

interferometer for temperature and strain simultaneous measurement. Applied optics, 2014. **53**(12): p. 2691-2695.

67. Xu, Y., *Multi-parameter sensing based on in-line Mach-Zehnder interferometer*. 2013: University of Ottawa (Canada).

68. Baker, C., R. Ahmad, and M. Rochette, *Simultaneous measurement of the core diameter and the numerical aperture in dual-mode step-index optical fibers.* Journal of Lightwave Technology, 2011. **29**(24): p. 3834-3837.

69. Bilodeau, F., K.O. Hill, D.C. Johnson, and S. Faucher, *Compact, low-loss, fused biconical taper couplers: overcoupled operation and antisymmetric supermode cutoff.* Optics letters, 1987. **12**(8): p. 634-636.

70. Birks, T.A. and Y.W. Li, *The shape of fiber tapers.* Journal of Lightwave Technology, 1992. **10**(4): p. 432-438.

71. Baker, C. and M. Rochette, *A generalized heat-brush approach for precise control of the waist profile in fiber tapers.* Optical Materials Express, 2011. **1**(6): p. 1065-1076.

72. Wang, Y.-P., L. Xiao, D. Wang, and W. Jin, *Highly sensitive long-period fiber-grating strain sensor with low temperature sensitivity.* Optics letters, 2006. **31**(23): p. 3414-3416.

73. Kersey, A., W. Morey, and T. Berkoff, *Fiber-optic Bragg grating strain sensor with drift-compensated high-resolution interferometric wavelength-shift detection.* Optics letters, 1993. **18**(1): p. 72-74.

74. Belleville, C. and G. Duplain, *White-light interferometric multimode fiber-optic strain sensor.* Optics letters, 1993. **18**(1): p. 78-80.

75. Tian, Z. and S.S.-H. Yam, *In-line abrupt taper optical fiber Mach–Zehnder interferometric strain sensor.* IEEE Photonics Technology Letters, 2009. **21**(3): p. 161-163.

76. Zhong, X., Y. Wang, C. Liao, S. Liu, J. Tang, and Q. Wang, *Temperature-insensitivity gas pressure sensor based on inflated long period fiber grating inscribed in photonic crystal fiber.* Optics letters, 2015. **40**(8): p. 1791-1794.

77. Zhao, C.-L., X. Yang, C. Lu, W. Jin, and M. Demokan, *Temperature-insensitive interferometer using a highly birefringent photonic crystal fiber loop mirror.* IEEE Photonics Technology Letters, 2004. **16**(11): p. 2535-2537.

78. Dobb, H., K. Kalli, and D.J. Webb, *Temperature-insensitive long period grating sensors in photonic crystal fibre.* Electronics Letters, 2004. **40**(11): p. 657-658.

79. Dong, X., H. Tam, and P. Shum, *Temperature-insensitive strain sensor with polarization-maintaining photonic crystal fiber based Sagnac interferometer.* Applied

physics letters, 2007. **90**(15): p. 151113.

80. Zhao, C.-L., L. Xiao, J. Ju, M. Demokan, and W. Jin, *Strain and temperature characteristics of a long-period grating written in a photonic crystal fiber and its application as a temperature-insensitive strain sensor.* Journal of Lightwave Technology, 2008. **26**(2): p. 220-227.

81. Villatoro, J., V. Finazzi, V.P. Minkovich, V. Pruneri, and G. Badenes, *Temperature-insensitive photonic crystal fiber interferometer for absolute strain sensing.* Applied Physics Letters, 2007. **91**(9): p. 091109.

82. Gao, S., C. Baker, L. Chen, and X. Bao, *Simultaneous Measurement of Temperature and Strain in a Dual-Core As 2 Se 3-PMMA Taper.* IEEE Photonics Technology Letters. **30**(1): p. 79-82.

83. Brownrigg, P., V. Vali, and B. Youmans, *Method for eliminating the temperature sensitivity of an optical fiber and a temperature insensitive optical fiber*. 1991, Google Patents.

84. Markos, C., I. Kubat, and O. Bang, *Hybrid polymer photonic crystal fiber with integrated chalcogenide glass nanofilms.* Scientific reports, 2014. **4**: p. 6057.

85. Woyessa, G., J.K. Pedersen, A. Fasano, K. Nielsen, C. Markos, H.K. Rasmussen, and O. Bang, *Zeonex-PMMA microstructured polymer optical FBGs for simultaneous humidity and temperature sensing.* Optics letters, 2017. **42**(6): p. 1161-1164.

86. Baker, C., S. Gao, L. Chen, and X. Bao, *Self-inscribed antisymmetric long-period grating in a dual-core As 2 Se 3-PMMA fiber.* Optics Express, 2017. **25**(11): p. 12409-12414.

87. Lee, B., *Review of the present status of optical fiber sensors.* Optical fiber technology, 2003. **9**(2): p. 57-79.

88. Kang, E.-S., T.-H. Lee, and B.-S. Bae, *Measurement of the thermo-optic coefficients in sol-gel derived inorganic–organic hybrid material films.* Applied physics letters, 2002. **81**(8): p. 1438-1440.

89. Gao, S., C. Baker, L. Chen, and X. Bao, *Approach for temperature-insensitive strain measurement using a dual-core As 2 Se 3-PMMA taper.* Optics letters, 2018. **43**(7): p. 1523-1526.

90. Hu, J., *Ultra-sensitive chemical vapor detection using micro-cavity photothermal spectroscopy.* Optics express, 2010. **18**(21): p. 22174-22186.

91. Bernini, U., P. Russo, M. Malinconico, E. Martucelli, M. Volpeau, and P. Mormile, *Temperature dependent optical properties of a synthesis blend of poly (methyl methacrylate) and vinyl rubber.* Journal of materials science, 1993. **28**(23): p. 6399-6402.

92. Anderson, P. and A. Varshneya, *Stress-optic coefficient of Ge · As · Se chalcogenide glasses.* Journal of non-crystalline solids, 1994. **168**(1-2): p. 125-131.

93. Baker, C. and M. Rochette, *High Nonlinearity and Single-Mode Transmission in Tapered Multimode $\hbox {As} _ {2}\hbox {Se} _ {3} $-PMMA Fibers.* IEEE Photonics Journal, 2012. **4**(3): p. 960-969.

94. Rothenberg, J.E., *Modulational instability for normal dispersion.* Physical Review A, 1990. **42**(1): p. 682.

95. Jensen, S.M., *The nonlinear coherent coupler.* IEEE Transactions on Microwave Theory and Techniques, 1982. **30**(10): p. 1568-1571.

96. Setzpfandt, F., A.S. Solntsev, J. Titchener, C.W. Wu, C. Xiong, R. Schiek, T. Pertsch, D.N. Neshev, and A.A. Sukhorukov, *Tunable generation of entangled photons in a nonlinear directional coupler.* Laser & Photonics Reviews, 2016. **10**(1): p. 131-136.

97. Snyder, A.W., *Coupled-mode theory for optical fibers.* JOSA, 1972. **62**(11): p. 1267-1277.

98. Gonthier, F., S. Lacroix, and J. Bures, *Numerical calculations of modes of optical waveguides with two-dimensional refractive index profiles by a field correction method.* Optical and quantum electronics, 1994. **26**(3): p. S135-S149.

99. Boyd, R.W., *Material slow light and structural slow light: similarities and differences for nonlinear optics.* JOSA B, 2011. **28**(12): p. A38-A44.

100. James, S., M. Dockney, and R. Tatam, *Simultaneous independent temperature and strain measurement using in-fibre Bragg grating sensors.* Electronics Letters, 1996. **32**(12): p. 1133-1134.

101. Bhatia, V. and A.M. Vengsarkar, *Optical fiber long-period grating sensors.* Optics letters, 1996. **21**(9): p. 692-694.

102. Han, Y.-G., S.B. Lee, C.-S. Kim, J.U. Kang, U.-C. Paek, and Y. Chung, *Simultaneous measurement of temperature and strain using dual long-period fiber gratings with controlled temperature and strain sensitivities.* Optics Express, 2003. **11**(5): p. 476-481.

103. Starodumov, A., L. Zenteno, D. Monzon, and E. De La Rosa, *Fiber Sagnac interferometer temperature sensor.* Applied Physics Letters, 1997. **70**(1): p. 19-21.

104. Nguyen, L.V., D. Hwang, S. Moon, D.S. Moon, and Y. Chung, *High temperature fiber sensor with high sensitivity based on core diameter mismatch.* Optics express, 2008. **16**(15): p. 11369-11375.

105. Grattan, K.T. and B.T. Meggitt, *Optical fiber sensor technology*. Vol. 1. 1995: Springer.

106. Kronenberg, P., P.K. Rastogi, P. Giaccari, and H.G. Limberger, *Relative humidity sensor*

with optical fiber Bragg gratings. Optics letters, 2002. **27**(16): p. 1385-1387.

107. Qian, W., C.-L. Zhao, S. He, X. Dong, S. Zhang, Z. Zhang, S. Jin, J. Guo, and H. Wei, *High-sensitivity temperature sensor based on an alcohol-filled photonic crystal fiber loop mirror.* Optics letters, 2011. **36**(9): p. 1548-1550.

108. Silva-López, M., A. Fender, W.N. MacPherson, J.S. Barton, J.D. Jones, D. Zhao, H. Dobb, D.J. Webb, L. Zhang, and I. Bennion, *Strain and temperature sensitivity of a single-mode polymer optical fiber.* Optics letters, 2005. **30**(23): p. 3129-3131.

109. Woyessa, G., A. Fasano, A. Stefani, C. Markos, K. Nielsen, H.K. Rasmussen, and O. Bang, *Single mode step-index polymer optical fiber for humidity insensitive high temperature fiber Bragg grating sensors.* Optics Express, 2016. **24**(2): p. 1253-1260.

110. Stolen, R. and J. Bjorkholm, *Parametric amplification and frequency conversion in optical fibers.* IEEE Journal of Quantum Electronics, 1982. **18**(7): p. 1062-1072.

111. Soto‐Crespo, J.M. and E. Wright, *All‐optical switching of solitons in two‐and three‐core nonlinear fiber couplers.* Journal of applied physics, 1991. **70**(12): p. 7240-7243.

112. Birks, T., W. Wadsworth, and P.S.J. Russell, *Supercontinuum generation in tapered fibers.* Optics letters, 2000. **25**(19): p. 1415-1417.

113. Nagasaka, K., H.T. Tong, L. Liu, M. Matsumoto, H. Tezuka, T. Suzuki, and Y. Ohishi. *Mid-infrared supercontinuum generation in chalcogenide multi-step index fibers with normal chromatic dispersion*. in *Optical Components and Materials XIV*. 2017. International Society for Optics and Photonics.

114. Bao, X. and L. Chen, *Recent progress in distributed fiber optic sensors.* Sensors, 2012. **12**(7): p. 8601-8639.

115. Li, J.H., K.S. Chiang, and K.W. Chow, *Modulation instabilities in two-core optical fibers.* JOSA B, 2011. **28**(7): p. 1693-1701.

116. Agrawal, G.P., *Modulation instability induced by cross-phase modulation.* Physical review letters, 1987. **59**(8): p. 880.

117. Chiang, K.S., *Propagation of short optical pulses in directional couplers with Kerr nonlinearity.* JOSA B, 1997. **14**(6): p. 1437-1443.

118. Chiang, K.S., *Coupled-mode equations for pulse switching in parallel waveguides.* IEEE journal of quantum electronics, 1997. **33**(6): p. 950-954.

119. Tasgal, R.S. and B.A. Malomed, *Modulational instabilities in the dual-core nonlinear optical fiber.* Physica Scripta, 1999. **60**(5): p. 418.

120. Snyder, A.W., D. Mitchell, L. Poladian, D.R. Rowland, and Y. Chen, *Physics of*

nonlinear fiber couplers. JOSA B, 1991. **8**(10): p. 2102-2118.

121. Shelby, R., M. Levenson, and P. Bayer, *Guided acoustic-wave Brillouin scattering.* Physical Review B, 1985. **31**(8): p. 5244.

122. Biryukov, A., M.E.e. Sukharev, and E.M. Dianov, *Excitation of sound waves upon propagation of laser pulses in optical fibres.* Quantum Electronics, 2002. **32**(9): p. 765.

123. Russell, P.S.J., D. Culverhouse, and F. Farahi, *Experimental observation of forward stimulated Brillouin scattering in dual-mode single-core fibre.* Electronics Letters, 1990. **26**(15): p. 1195-1196.

124. Russell, P.S.J., D. Culverhouse, and F. Farahi, *Theory of forward stimulated Brillouin scattering in dual-mode single-core fibers.* IEEE Journal of Quantum Electronics, 1991. **27**(3): p. 836-842.

125. Kang, M., A. Nazarkin, A. Brenn, and P.S.J. Russell, *Tightly trapped acoustic phonons in photonic crystal fibres as highly nonlinear artificial Raman oscillators.* Nature Physics, 2009. **5**(4): p. 276.

126. Wang, J., Y. Zhu, R. Zhang, and D.J. Gauthier, *FSBS resonances observed in a standard highly nonlinear fiber.* Optics express, 2011. **19**(6): p. 5339-5349.

127. Peral, E. and A. Yariv, *Degradation of modulation and noise characteristics of semiconductor lasers after propagation in optical fiber due to a phase shift induced by stimulated Brillouin scattering.* IEEE journal of quantum electronics, 1999. **35**(8): p. 1185-1195.

128. Poustie, A.J., *Bandwidth and mode intensities of guided acoustic-wave Brillouin scattering in optical fibers.* JOSA B, 1993. **10**(4): p. 691-696.

129. Hayashi, N., Y. Mizuno, K. Nakamura, S.Y. Set, and S. Yamashita, *Experimental study on depolarized GAWBS spectrum for optomechanical sensing of liquids outside standard fibers.* Optics Express, 2017. **25**(3): p. 2239-2244.

130. Thurston, R., *Elastic waves in rods and optical fibers.* Journal of sound and vibration, 1992. **159**(3): p. 441-467.

131. Engan, H.E., B.Y. Kim, J.N. Blake, and H.J. Shaw, *Propagation and optical interaction of guided acoustic waves in two-mode optical fibers.* Journal of Lightwave Technology, 1988. **6**(3): p. 428-436.

132. Auld, B.A., *Acoustic fields and waves in solids*. 1973: Рипол Классик.

133. Diamandi, H.H., Y. London, and A. Zadok, *Opto-mechanical inter-core cross-talk in multi-core fibers.* Optica, 2017. **4**(3): p. 289-297.

134. Antman, Y., A. Clain, Y. London, and A. Zadok, *Optomechanical sensing of liquids*

outside standard fibers using forward stimulated Brillouin scattering. Optica, 2016. **3**(5): p. 510-516.

135. Jarschel, P., L. Magalhaes, I. Aldaya, O. Florez, and P. Dainese, *Fiber taper diameter characterization using forward Brillouin scattering.* Optics letters, 2018. **43**(5): p. 995-998.

136. Thomas, P., N. Rowell, H. Van Driel, and G. Stegeman, *Normal acoustic modes and Brillouin scattering in single-mode optical fibers.* Physical review B, 1979. **19**(10): p. 4986.

137. Hayashi, N., Y. Mizuno, D. Koyama, and K. Nakamura, *Measurement of acoustic velocity in poly (methyl methacrylate)-based polymer optical fiber for Brillouin frequency shift estimation.* Applied Physics Express, 2011. **4**(10): p. 102501.

138. Peters, K., *Polymer optical fiber sensors—a review.* Smart materials and structures, 2010. **20**(1): p. 013002.

139. Webb, D.J., *Fibre Bragg grating sensors in polymer optical fibres.* Measurement Science and Technology, 2015. **26**(9): p. 092004.

140. Zhang, C., W. Zhang, D.J. Webb, and G.-D. Peng, *Optical fibre temperature and humidity sensor.* Electronics Letters, 2010. **46**(9): p. 643-644.